PHASE SLIP PHENOMENA AND VORTEX DYNAMICS IN MESOSCOPIC SUPERCONDUCTORS

Mathieu Lu-Dac

Doctoral dissertation
Jožef Stefan International Postgraduate School
Ljubljana, Slovenija, March 2011

Supervisor:
Prof. Dr. Viktor V. Kabanov

Evaluation Board

Prof. Dr. Feodor V. Kusmartsev, Loughborough University, United Kingdom
Asst. Prof. Dr. Tomaž Mertelj, Jožef Stefan Institute, Ljubljana, Slovenia
Prof. Dr. Bosiljka Tadić, Jožef Stefan Institute, Ljubljana, Slovenia

MEDNARODNA PODIPLOMSKA ŠOLA JOŽEFA STEFANA
JOŽEF STEFAN INTERNATIONAL POSTGRADUATE SCHOOL

Mathieu Lu-Dac

Phase slip phenomena and vortex dynamics in mesoscopic superconductors

Doctoral Dissertation

Pojav faznega zdrsa in dinamika vrtincev v mezoskopskih superprevodnikih

Doktorska disertacija

Supervisor: Prof. Dr. Viktor V. Kabanov

Ljubljana, Slovenia

March 2011

Abstract

Phase slip phenomena and vortex dynamics in mesoscopic superconductors

We investigate the dynamics in one-dimensional (1D) and two dimensional (2D) mesoscopic superconductors in an external magnetic field using the time-dependent Ginzburg-Landau equations. We analyze the different transitions between metastable states and describe the creation of topological defects that occur as the phase of the Ginzburg-Landau order parameter makes finite jumps: phase slip phenomena.

We first analyze the stability and the dynamics for the phase slip phenomena starting from a metastable state in a 1D ring. We find a stability condition relating the winding number of the initial metastable state and the number of flux quanta penetrating the ring. We as well study the competition between simultaneous and consecutive multiple phase slips analytically and numerically.

In 2D, we consider flux penetration to a superconducting thin-walled cylinder. We show that in the low field limit, the kinetics are deterministic. In the strong field limit the dynamics become stochastic. Analytical calculation and simulations show that, in the case of a superconducting cylinder in the presence of a constant magnetic field, simple perturbations could not result in the creation of well defined vortex-antivortex pairs. We identify different regimes depending on the value of the magnetic field: at low magnetic field, quasi-1D dynamics such as vortex rivers prevail, but at high magnetic field, the sample is quenched and kinetics are similar to the Kibble-Zurek mechanism of vortex production. Surprisingly the inhomogeneity in the cylinder reduces the level of stochasticity because of the predominance of Kelvin-Helmholtz vortices.

Last, we investigate the possibility of a novel kind of optical pump probe spectroscopy where the two laser pulses are focused on different areas of the sample. The response to the destruction of the superconducting state in a large part of a mesoscopic ring is studied numerically. We evaluate the relaxation rates of the superconducting order parameter as well as the voltage induced by the charge imbalance and discuss the feasibility of such measurements.

KEY WORDS: Superconductivity, Ginzburg-Landau theory, Vortex dynamics.

PACS: 74.40.Gh, 74.40.De, 74.78.Na, 74.81.-g.

Povzetek

Pojav faznega zdrsa in dinamika vrtincev v mezoskopskih superprevodnikih

Z uporabo časovno odvisnih enačb Ginzburga in Landaua smo raziskovali dinamiko v enodimenzionalnih (1D) in dvodimenzionalnih (2D) mezoskopskih superprevodnikih v zunanjem magnetnem polju. Analizirali smo različne prehode med metastabilnimi stanji in opisali oblikovanje topolokih defektov, ki se pojavijo, ko faza parametra reda naredi končni preskok (fazni zdrs).

Najprej smo analizirali stabilnost in dinamike faznega zdrsa, pri čemer smo začeli z metastabilnim stanjem v 1D obroču. Določili smo pogoj stabilnosti v povezavi z ovojnim tevilom prvotnega metastabilnega stanja in s tevilom kvantov magnetnega pretoka, ki prodirajo skozi obroč. Proučevali smo tudi tekmovanje med sočasnimi in zaporednimi večkratnimi faznimi zdrsi, tako analitično kot numerično.

V 2D smo proučevali prodiranje magnetnega pretoka v plašč valja. Pokazali smo, da je v približku majhnega magnetnega polja kinetika deterministična, pri velikem magnetnem polju pa postane dinamika stohastična. Analitični izračun in simulacije kažejo, da v primeru plašča valja v prisotnosti konstantnega magnetnega polja enostavne motnje ne morejo povzročiti nastanka dobro definiranih parov vrtinec-antivrtinec. V odvisnosti od velikosti magnetnega polja smo identificirali različne režime: v majhnem magnetnem polju prevlada kvazi-1D dinamika kot npr. reke vrtincev, v velikem magnetnem polju pa je kinetika podobna Kibble-Zurek-ovemu mehanizmu nastanka vrtincev. Presenetljivo pa nehomogenost v plašču valja zniža raven stohastičnosti, ker prevladujejo Kelvin-Helmholtz-ovi vrtinci.

Nazadnje smo teoretično proučevali možnost uporabe nove vrste optične časovno ločljive ekscitacijske spektroskopije, kjer sta dva ločena laserska sunka usmerjena na različne dele vzorca. V tem okviru smo numerično proučevali odziv na uničenje superprevodnega stanja v večjem delu mezoskopskega obroča. Ocenili smo hitrost relaksacije superprevodnega parametra reda, kot tudi električno napetost, ki nastane zaradi neravnovesnega naboja in razpravljali o izvedljivosti teh meritev.

KEY WORDS: Superprevodnost, Ginzburg-Landau teorija, Dinamika vrtincev.

PACS: 74.40.Gh, 74.40.De, 74.78.Na, 74.81.-g.

Contents

Abbreviations

BCS	**B**ardeen **C**ooper **S**chrieffer
CGS	**C**entimeter **G**ram **S**econd (see appendix A)
cm	**c**enti**m**eter
Eq.	**E**quation
Fig.	**F**igure
Fr	**Fr**anklin (CGS)
G	**G**auss (CGS)
GL	**G**inzburg-**L**andau
He	**H**elium
K	**K**elvin
KH	**K**elvin-**H**elmholtz
KZ	**K**ibble-**Z**urek
LAMH	**L**anger **A**mbegaokar **M**cCumber **H**alperin
NBN	**N**iobium **N**itrate
PSC	**P**hase **S**lip **C**enter
PSL	**P**hase **S**lip **L**ine
ps	**p**ico**s**econd ($= 10^{-12}$ s)
Ref.	**R**eference
s	**s**econd
SI	**I**nternational **S**ystem
SQUID	**S**uperconducting **QU**antum **I**nterference **D**evice
statV	**s**tat**V**olt
TDGL	**T**ime-**D**ependent **G**inzburg-**L**andau
V	**V**olt
VaV	**V**ortex-**a**nti**V**ortex

Physical Constants

Constant Name	Symbol		Constant Value in CGS units (see appendix A)
Speed of Light	c	=	2.9979248×10^{10} cm $\cdot$ s^{-1}
Elementary charge	e	=	4.80310^{-10} Fr
Planck constant	$\hbar$	=	$1.054571628 \times 10^{-27}$ erg $\cdot$ s
Boltzmann constant	k_B	=	$1.3806504 \times 10^{-16}$ erg$\cdot$K^{-1}
Electron mass	m	=	$9.10938215 \times 10^{-28}$ g
Magnetic flux quantum	ϕ_0	=	$\frac{\pi\hbar c}{e} \approx 2.07 \times 10^{-}7$ G $\cdot$ cm^2
	π	$\approx$	3.14159265

Symbols

Symbol	Name	CGS unit (see appendix A)
$\mathbf{A}$	Magnetic vector potential	$\mathrm{G} \cdot \mathrm{cm}$
d	Thickness	cm
$\mathbf{E}$	Electric Field	G
F	Free energy density	$\mathrm{erg \cdot cm^{-3}}$
$\mathcal{F}$	Free energy	erg
G	Gibbs free energy density	$\mathrm{erg \cdot cm^{-3}}$
$\mathbf{H}$	Magnetic field	G
$\mathbf{H_c}$	Critical magnetic field	G
$\mathbf{H_{c1}}$	Lower critical magnetic field	G
$\mathbf{H_{c2}}$	Upper critical magnetic field	G
$\mathbf{J}$	Total current density	$\mathrm{Fr} \cdot \mathrm{s^{-1}}$
$\mathbf{J_s}$	Superconducting current density	$\mathrm{Fr} \cdot \mathrm{s^{-1}}$
$\mathbf{J_n}$	Normal current density	$\mathrm{Fr} \cdot \mathrm{s^{-1}}$
n_s	Superfluid density	$\mathrm{cm^{-3}}$
$\mathcal{P}$	Phase slip rate	$\mathrm{s^{-1}}$
R	Radius	cm
T	Temperature	K
T_c	Critical Temperature	K
$\mathbf{S} = (X, Y, Z) = (r, \zeta, z)$	Spatial coordinate	cm
λ_L	London penetration depth	cm
σ_n	normal conductivity	$\mathrm{s^{-1}}$
τ	time	s
τ_ρ	Characteristic time of ρ	s
τ_θ	Characteristic time of θ	s
τ_T	Characteristic time of diffusion	s

ϕ	Magnetic flux	G·cm^2
$\Psi = \lvert\Psi\rvert e^{i\vartheta}$	Order parameter	
χ	Electrostatic potential	Fr
ξ	Coherence length	cm

Dimensionless Symbol	Name
$\mathbf{a}$	Magnetic vector potential
D	Heat diffusion coefficient
$\mathcal{H}$	Heaviside step function
$\mathbf{j}$	Total current
$\mathbf{j_s}$	Superconducting current
$\mathbf{j_n}$	Normal current
$\mathbf{s} = (x, y, z)$	Spatial coordinate
η	Langevin thermal noise
κ	Ginzburg-Landau parameter
Φ	Electrostatic potential
$\psi = \rho e^{i\theta}$	Order parameter

Chapter 1

General Introduction

1.1 Content of the thesis

In this thesis, we study the dynamics of the electronic properties of superconductors driven out of equilibrium by external perturbations. Using a time-dependent derivation of the Ginzburg-Landau theory, which describes the superconducting state using a complex order parameter, we analyze the different possible transitions which involve topological jumps of the phase of the order parameter: phase slip phenomena. The nucleation of vortices, which corresponds to this topological configuration, has been our main concern from the very beginning, but this starting ideas lead us to discover a broader range of possibilities.

Most of the classic fundamental results can be found in [1–6]. Chapter 1, is a general introduction to the field of superconductivity, which is meant to help the non-specialist to understand the subject of the thesis. In chapter 2 we explain in more details the theoretical background of the thesis: the Ginzburg-Landau theory and some of the fundamental results that can be obtained including the extension to the time-dependent Ginzburg-Landau equations. In chapter 3 we introduce the time-dependent Ginzburg-Landau equations in a dimensionless form and derive the stationary solutions as well as the condition of their stability. Chapter 4 focuses on the aspects of the phase slip phenomena that occur in one dimensional (1D) cases. In particular, we studied a mesoscopic ring in presence of an external magnetic field and obtained results concerning the competition between consecutive and simultaneous phase slip centers. In chapter 5 we address the problem of phase slip phenomena for the two dimensional (2D) case. We describe the possible dynamical processes that can happen during a transition between two stationary solutions of the Ginzburg-Landau equations. In a 2D cylinder penetrated by an external magnetic field, we discuss the evolution of the dynamics from the ordered phase slip line to the chaotic Kibble-Zurek mechanism. In chapter 6 we describe some new scenarios for ultrafast optical spectroscopy. Indeed, using the time-dependent

Ginzburg-Landau equations, we make predictions to check whether some new configurations for experiments would be justified or not. Last, chapter 7 summarizes the overall conclusions of this thesis.

1.2 Superconductivity for non-scientists

Superconductivity is a physical phenomenon related to the conduction of electricity. When electricity runs through a material, part of the electric energy is converted into heat. In some electric devices, this heating is the wanted effect, like in electric stoves, but often electric heating is a loss of energy and can cause a device to overheat. The amount of heating depends on the material and the characteristic measure is called electric resistance. The larger the electric resistance is, the larger will be the heat produced in the material for the same value of electric current.

When the temperature is decreased close to the absolute zero (-273.15 degrees Celsius), some materials see their resistance drop to zero Ohm: electric energy is no longer lost when a current flows through the material. This is what is called superconductivity and such materials are called superconductors. It was discovered in 1911 by H. Kamerlingh-Onnes. Of course, for many applications, the materials would need to become superconductors at room temperature. Looking for such materials has been one of the leading subjects in physical research for the past century. Unfortunately, until now, superconductivity remains in the domain of very low temperatures. Yet superconductors have some "real world" applications when very high electric currents are needed. Indeed, using very high currents, one can produce very strong magnetic fields which are used in magnetic resonance imaging, fusion reactors and other research projects like the Large Hadron Collider (LHC). Last, but not least, superconductivity is a complex physical phenomenon involving many microscopic effects some of which can be used for applications. Today, a hundred years after the discovery of superconductivity, we still do not understand all the details and the theory remains a large puzzle to complete. This thesis will focus on one humble piece of the puzzle that we define at the end of this chapter.

1.3 The physics of superconductors in a nutshell

1.3.1 Perfect conductivity, perfect diamagnetism

Superconductivity was discovered in 1911 when H. Kamerlingh-Onnes asked his student Gilles Holst to study the temperature-dependence of mercury which could be extensively purified. Having discovered how to liquify helium three years before, Onnes and Holst were able to reach very low temperatures. They found out that the resistance of mercury completely vanished at 4.19 K.

Below this temperature, mercury behaved as a perfect conductor. This new phenomenon was called superconductivity. Zero electrical resistivity or equivalently perfect conductivity became the first hallmark of superconductors. Many metals, alloys and intermetallic compounds, were found to be superconductors at different temperatures.

The second hallmark of superconductivity is the perfect diamagnetism, discovered in 1933 by W. Meissner and R. Ochsenfeld. They found out that not only a magnetic field is excluded from entering a superconductor, as could be explained by perfect conductivity, but also that a field penetrating a sample is expelled as the sample is cooled below T_c. This phenomenon, on the opposite to perfect conductivity which would trap the field inside, was called *Meissner effect*. The discovery of this reversible effect was very important as it implies that the transition to the superconducting state should be treated as a phase transition, using the analytical tools of thermodynamics. Superconductors were characterized by a phase diagram (see figure 1.1), implying that the superconducting state would disappear once the external magnetic field becomes larger than the critical field H_c.

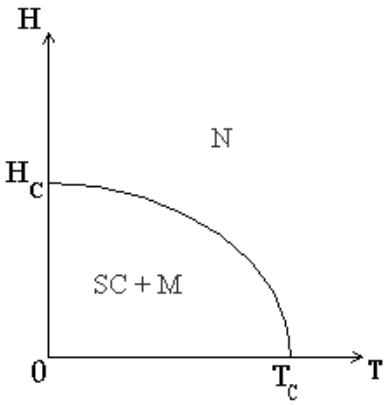

FIGURE 1.1: Phase diagram of a type-I superconductor. The SC+M part is the superconducting state with Meissner effect and the N part is the normal state where temperature and/or external field are too high and destroy superconductivity.

1.3.2 The London equations

1.3.2.1 The first London equation

The idea of the London equations is to derive the equations of a perfect conductor. Indeed, if we consider that we have a density n_s of superconducting electrons, the equation of their motion is:

$$n_s m \frac{d\mathbf{v_s}}{dt} = n_s e \mathbf{E}, \tag{1.1}$$

where m is the electron mass, e its absolute charge and $\mathbf{v_s}$ the average velocity of the superconducting electrons. $\mathbf{E}$ is the electric field which can be rewritten using the supercurrent density

$\mathbf{j_s} = n_s e \mathbf{v_s}$

$$\mathbf{E} = \frac{d}{dt}(\Lambda \mathbf{j_s}) \tag{1.2}$$

with

$$\Lambda = \frac{m}{n_s e^2}. \tag{1.3}$$

Equation (1.2) is called the first London equation and shows the direct relation between the superconducting current variations and the electric field. Namely, a stationary supercurrent flows without voltage and thus without resistance. The first London equation thus describes the first hallmark of superconductivity.

1.3.2.2 The second London equation

To describe the second Hallmark of superconductivity, one needs to characterize the state of the superconductor in presence of an external magnetic field $\mathbf{H}$. The first step is to calculate the free energy of a superconductor in a magnetic field. The free energy density F is:

$$F = F_0 + W_{\text{kin}} + W_{\text{mag}}, \tag{1.4}$$

where F_0 is the free energy of the normal state. The magnetic energy density W_{mag} is $H^2/8\pi$, whereas the kinetic energy density of the supercurrent W_{kin} is:

$$W_{\text{kin}} = \frac{n_s m v_s^2}{2} = \frac{m j_s^2}{2 n_s e^2} \tag{1.5}$$

which becomes, using Maxwell's equation $\text{curl}\mathbf{H} = \frac{4\pi}{c}\mathbf{j_s}$:

$$W_{\text{kin}} = \frac{\lambda_L^2}{8\pi}(\text{curl}\mathbf{H})^2 \tag{1.6}$$

where

$$\lambda_L^2 = \frac{mc^2}{4\pi n_s e^2}. \tag{1.7}$$

Last, the total free energy $\mathcal{F}$ of the superconductor is

$$\mathcal{F} = \mathcal{F}_0 + \frac{1}{8\pi}\int [\mathbf{H}^2 + \lambda_L^2 (\text{curl}\mathbf{H})^2] dV, \tag{1.8}$$

where $\mathcal{F}_0$ is the free energy of the superconductor in absence of magnetic field.

To describe the state of the superconductor, we need to find the minimum of the free energy and write the infinitesimal variation $\delta\mathcal{F}$ of the free energy caused by the infinitesimal variation $\delta\mathbf{H}$ of the magnetic field:

$$\delta\mathcal{F} = \frac{1}{8\pi}\int \left(2\mathbf{H}\cdot\delta\mathbf{H} + 2\lambda_L^2 \text{curl}\mathbf{H}\cdot\text{curl}\delta\mathbf{H}\right) dV. \tag{1.9}$$

Writing the minimization condition $\delta\mathcal{F} = 0$ and developing using vector analysis, we have:

$$\int [\mathbf{H} + \lambda_L^2(\text{curlcurl}\mathbf{H})] \cdot \delta\mathbf{H} dV - \int \text{div}[\text{curl}\mathbf{H} \times \delta\mathbf{H}] dV = 0 \tag{1.10}$$

The second integral in (1.10) can be transformed by the Gauss theorem into $\oint (\text{curl}\mathbf{H} \times \delta\mathbf{H}) \cdot \mathbf{dS}$ which, integrated over the external surface of the superconductor is zero because there the field is fixed by the external field.

We obtain the second London equation:

$$\mathbf{H} + \lambda_L^2 \text{curlcurl}\mathbf{H} = 0 \tag{1.11}$$

Using Maxwell-Ampere equation and the vector potential $\mathbf{A}$ defined by the London gauge $\text{div}\mathbf{A} = 0$ and $\mathbf{A} \cdot \mathbf{n} = 0$ where $\mathbf{n}$ is the unit vector perpendicular to the surface of the superconductor, we can write the second London equation in another form:

$$\mathbf{j_s} = -\frac{c}{4\pi\lambda_L^2}\mathbf{A}. \tag{1.12}$$

1.3.2.3 The London Penetration depth

Let us now have a look at the meaning of the length λ_L that appeared in the equations. For simplicity, we take here a simple geometry with an infinite superconductor defined by $x > 0$: the surface of the superconductor is defined by the plane $x = 0$. The magnetic field is taken along the z axis. With such a geometry the second London equation (1.11) becomes:

$$\frac{d^2H}{dx^2} - \lambda_L^{-2} H = 0 \tag{1.13}$$

with the boundary conditions:

$$H(x) = H_0, \text{ for } x \leq 0 \tag{1.14}$$

$$H(\infty) = 0. \tag{1.15}$$

The solution of the problem is:

$$H(x) = H_0, \text{ for } x \leq 0 \tag{1.16}$$

$$H(x) = H_0 e^{-\frac{x}{\lambda_L}}, \text{ for } x \geq 0. \tag{1.17}$$

This result describes the second Hallmark of superconductivity: the Meissner effect. The magnetic field is reduced exponentially as we go deeper in the superconductor, with a small characteristic

length λ_L, which is comprehensively called the "penetration depth". When we look at the superconductor at a larger scale, we therefore see that the magnetic field does not penetrate the sample. We get a similar equation for the current:

$$j_s = \frac{cH_0}{4\pi\lambda_L} e^{-\frac{-x}{\lambda_L}}. \tag{1.18}$$

In presence of a magnetic field, the screening current thus runs at the surface of the superconductor.

1.3.3 The development of new theories

The London equations are local equations and hence define the superconducting properties as such. However, early discrepancies between experimental estimations of λ_L at zero temperature led A. B. Pippard [7] in 1953 to introduce non-local effects into the London equations. Spatial changes of quantities such as the superfluid density n_s in a superconductor may only occur on a finite length scale, the coherence length ξ and not over arbitrarily small distances. This was a first step towards a microscopic theory, but the precise mechanism for superconductivity at the atomic level still remained an enigma.

The microscopic theory emerged only in 1957, introduced by J. Bardeen, L. N. Cooper and J.R. Schrieffer [8–10] (the BCS theory). The key to the BCS theory was to understand that since different isotopes of the same element had different critical temperature T_c (the so-called isotope effect), the crystal lattice had to play a role in the behavior of the electrons. More precisely, they discovered that the vibrations of the crystal lattice (phonons) could interact with the electrons. The electron-phonon interaction leads to the formation of pairs of electrons below T_c: the Cooper pairs [8]. The energy required to break those pairs corresponds to the energy gap between the ground state and the quasi-particle excitations of the system. The BCS theory therefore brought a way to describe quantitatively the superconducting state at the atomic scale.

The Ginzburg-Landau (GL) theory that will have most of our interest in this work, was published in 1950, before the BCS theory, by V. L. Ginzburg and L. D. Landau [11], but was recognized universally only later on. It is a phenomenological theory in the sense that it does not give quantitative predictions on its own, but should first be fitted by experimental values. However, in 1959, Gor'kov [12, 13] derived the quantities involved in the GL equations from the BCS theory, thus transforming it into a self-consistent theory.

The latest important breakthrough in superconductivity was made in 1986, with the discovery of high temperature superconductors, which lead to a renewed interest in superconductors, with T_c reaching $164K$ (underpressure), far above the freezing temperature of nitrogen. However, the mechanism responsible for such high T_c remains a controversial subject for theoreticians.

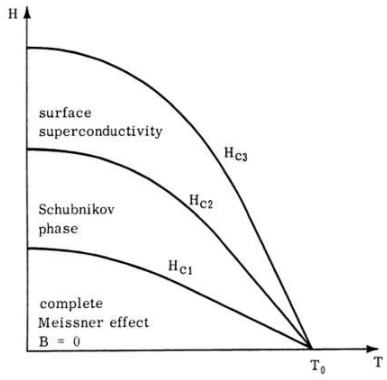

FIGURE 1.2: The complete phase diagram of a type-II superconductor: below H_c1 we have a complete Meissner effect and no magnetic field can penetrate the sample. For $H_{c1} < H < H_{c2}$, the magnetic field penetrates the superconductors in the form of quantized vortices. Last, for $H_{c2} < H < H_{c3}$, the superconductivity survives only close to the surface of the sample.

1.3.4 The limits of the two hallmarks of superconductivity

We described above the two hallmarks of the superconducting state and their representation in a phase diagram. Yet, this picture was restricted to the so-called type-I superconductors by the theory of A. A. Abrikosov [14–16], who opposed them to type-II superconductors. His theory was based on the GL theory when the London penetration depth λ_L is larger than the coherence length ξ (see section 2.1.4 and 2.1.4 for more details). He predicted that for type-II superconductors submitted to an external field, the superconducting state would first be modified when the field is greater than a first critical field H_{c1}, letting an increasing part of the field penetrate the sample in the form of quantized vortex filaments, as the external field increases. Once the field reaches the upper critical field H_{c2}, it penetrates completely through the superconductor [1]. In type II superconductors, the second Hallmark is thus more complex because of the possibility of vortices penetrating the system: when $H_{c1} < H < H_{c2}$, the superconductor is in the Schubnikov [17] or mixed state. When the vortices start to move, for example if a transport current is applied, there will be resistivity and the second Hallmark of superconductivity will be modified as well. Moreover, in macroscopic samples, the superconducting state (zero electric resistance) can survive above H_{c2}, in a region close to the surface of the superconductor, for $H_{c2} < H < H_{c3}$. Those effects modify the phase diagram which is drawn in figure 1.2.

Last, in type I superconductors, because of the Meissner effect, for certain geometries, the effective critical field will depend on the region in the sample. Therefore, close to the critical field, the sample will be divided into regions where the superconducting state is destroyed and regions where it still survives. This state is called the intermediate state [1–3].

1.4 Problematic of the thesis

In this work, we are interested in the dynamics of the superconducting phase in the framework of time-dependent Ginzburg-Landau equations. For the experimentalist, this corresponds to the observation of a certain set of properties after the external parameters have been changed. As theoreticians, we use the equations to describe the superconducting state and solve them for different values of the parameters. More precisely, our idea is that changing the value of the external magnetic field, a superconductor will undergo a transition towards a state with different properties. We are mostly interested about transitions that involve the appearance of resistivity. The resistivity is in that case associated with the creation of topological defects regarding the phase of the order parameter: such dynamics are described by phase slip-phenomena which include our starting motivation, vortex dynamics.

Chapter 2

The Ginzburg-Landau framework

In this chapter we explain the basics of the Ginzburg-Landau (GL) theory and derive the most important results for the rest of our work. Indeed, the GL theory along with its extension to the nonequilibrium case (time-dependent GL) will be the main background for our investigation.

2.1 The Ginzburg-Landau Theory

The GL theory was introduced in 1950 by V. L. Ginzburg and L. D. Landau [11]. It is the first theory of superconductivity that takes into account quantum effects. It is commonly called a phenomenological theory as opposed to the microscopic theories (like the BCS theory) that investigate the details of the interactions at the atomic level. Instead, it focuses on the behavior of the system as a whole. Nevertheless, the GL theory was shown to be in complete agreement with the BCS derivation close to T_c [12, 13]. The Ginzburg-Landau theory is the application to the superconducting state of the Landau theory of phase transitions.

2.1.1 Landau theory of phase transitions

A phase transition is the transformation of a thermodynamic system from one phase or state of matter to another. In particular, in many phase transitions, the system switches from a state of higher symmetry to a state of lower symmetry (or vice versa): the symmetry group of the state after the phase transition is a subgroup of the symmetry group of the state before the phase transition. The Landau [4] theory of phase transitions is based on the existence of an order parameter Ψ: a global variable that evolves with the symmetry of the system: $|\Psi| = 0$ in the high symmetry phase and $|\Psi| > 0$ in the low symmetry phase. To describe the properties of the system

in the low symmetry phase, one must construct an expression of the free energy depending on the order parameter and minimize it.

In second order phase transitions, the order parameter is a continuous function and the free energy density F can be written as a Taylor expansion of Ψ. Let us here consider that Ψ is a real function. The Taylor expansion of the free energy is:

$$F = F_0 + c_1\Psi + c_2\Psi^2 + c_3\Psi^3 + c_4\Psi^4... \tag{2.1}$$

where F_0 is the free energy of the high symmetry phase. The coefficients c_n are characteristics of the material and independent of Ψ. They might however depend on other external conditions like pressure and temperature. As the symmetries of each state have to be respected, some of the terms of the expansion will not be allowed. In particular, c_1 is always zero (it is impossible to have a non-zero order parameter invariant to all symmetries that would vanish during the phase transition). The quadratic term $c_2\Psi^2$ thus determines the landscape of the free energy close to $\Psi = 0$. The stable state will correspond to the minimum of the free energy. In the high symmetry phase, F must have a minimum for $\Psi = 0$ which implies that $c_2 > 0$. In the low symmetry phase, F must have a minimum for $|\Psi| > 0$ which implies that there, $c_2 < 0$. In the common case of a transition driven by the temperature T happening at a critical temperature T_c, we simply write $c_2 \propto (T - T_c)$. In presence of an external field, there might be as well a linear coupling term with the conjugated field in the expansion. For example, in ferroelectrics, the order parameter is the electric dipole moment per unit volume and the conjugated field is the electric field.

There are two families of curves that we can distinguish when we draw the variation of the free energy as a function of Ψ for different temperatures. The first family of curves, plotted in Fig. 2.1(a) is typical of second order phase transitions. As written above, we have for $T > T_c$, $\left(\frac{\partial^2 F}{\partial \Psi^2}\right)_{\Psi=0} > 0$. For $T < T_c$, a non-zero (either positive or negative) order parameter becomes the minimum of the free energy: $\left(\frac{\partial^2 F}{\partial \Psi^2}\right)_{\Psi=0} > 0$. In many cases, one can thus determine the critical temperature by solving the condition $\left(\frac{\partial^2 F}{\partial \Psi^2}\right)_{\Psi=0} = 0$ at $T = T_c$. The second family of curves, plotted in Fig. 2.1(b) is typical of the first order phase transitions: For $T > T_c$ the global minimum is found for $\Psi = 0$ but there is another local minimum corresponding to a finite value of Ψ. For $T = T_c$ the two minima are at the same height: there is a coexistence of the two phases. This is a characteristic of first order phase transitions. For $T < T_c$, the second minima, the one corresponding to a finite value of Ψ, now becomes the lowest and is therefore the global minimum of the free energy. The second minima is obtained for $\Psi > 0$ if $c_3 < 0$ and for $\Psi < 0$ if $c_3 > 0$. One immediately remarks that the evolution of the order parameter around T_c is ambiguously defined by the Landau theory: this is because the order parameter is not a continuous function

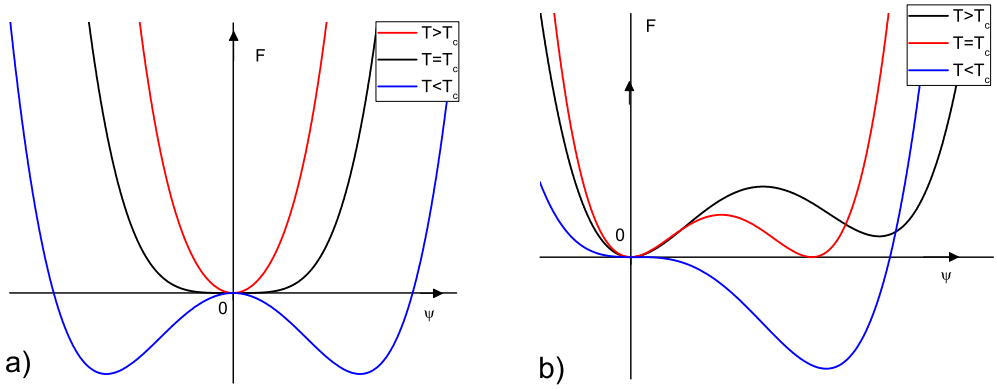

FIGURE 2.1: Shape of the free energy as a function of the order parameter Ψ for different temperatures. There are two possible families of curves corresponding to second order phase transitions (a) and first order phase transitions (b).

of the temperature around T_c. The order parameter indeed switches between 0 and a finite value corresponding to the other minimum of the free energy.

Having a non-zero cubic term $c_3\Psi^3$ in the expansion (after symmetry considerations) will thus imply that the transition is of the first order. The absence of cubic term is a necessary but not sufficient condition to have a second order phase transition: there can be first order phase transitions where the cubic term is not alowed by symmetry. The truncation of the Taylor expansion (2.1) depends on the needs of each theory but the last term should be an even power of Ψ with a positive coefficient to keep the minimum of F bounded. First order phase transitions are commonly described with expansions of higher orders than second order phase transitions. In second order phase transitions, the physics is often well described by the quadratic and quartic terms alone.

2.1.2 The superconducting transition as a second order phase transition

The principle of the GL theory is to use a kind of wavefunction of the superconducting electrons as the order parameter of a second order phase transition [5]. At the time, the BCS wavefunction describing the coherent behavior of Cooper pairs was of course unknown and the GL description was based on physical intuition. Moreover, in the initial theory, the value of the constants were phenomenological: they could be determined only by experiments. With the BCS theory the link between the order parameter and the BCS wavefunction could be established and fixed the value of the constants to the physical quantities. Close to T_c, L. P. Gor'kov [12, 12] even proved the equivalency between both theories.

In the GL theory, the order parameter is a complex variable $\Psi = |\Psi|e^{i\vartheta}$, the amplitude of which is related to the density of the superconducting electrons. The phase of Ψ is defined modulo 2π and the gradient of the phase is linked to the superfluid velocity (see Eq. (2.21)).

Having n_s the density of superconducting electrons, we choose a normalization of the wavefunction such as $|\Psi|^2$ is the density of Cooper pairs:

$$|\Psi|^2 = \frac{n_s}{2}. \tag{2.2}$$

In the case of a homogeneous superconductor near T_c and in absence of external magnetic fields, the free energy density is expanded in powers of the invariant $|\Psi|^2$:

$$F = F_n + \alpha|\Psi|^2 + \frac{\beta}{2}|\Psi|^4. \tag{2.3}$$

The expansion coefficients α and β are characteristics of the material and F_n is here the free energy density of the normal state. The expansion is truncated at the fourth order (which is common for second order phase transitions). As described above, we have $\alpha \propto (T - T_c)$ and $\beta > 0$. The coefficient β is also assumed to be completely independent of the temperature. In the superconducting state, we can minimize the free energy and find the equilibrium value of the amplitude of the order parameter

$$|\Psi_0|^2 = -\frac{\alpha}{\beta}. \tag{2.4}$$

2.1.3 The Ginzburg-Landau equations

In the general case, when the order parameter depends on the spatial coordinate and in presence of an external magnetic field $\mathbf{H_0}$, the Gibbs free energy $\mathcal{G}$ is constructed as follows:

$$\mathcal{G} = \mathcal{G}_n + \int \left(\alpha|\Psi|^2 + \frac{\beta}{2}|\Psi|^4 + \frac{1}{4m}\left|-i\hbar\nabla\Psi - \frac{2e}{c}\mathbf{A}\Psi\right|^2 + \frac{H^2}{8\pi} - \frac{\mathbf{H}\cdot\mathbf{H_0}}{4\pi} \right) dV. \tag{2.5}$$

In this expression, we recognize the energy of the normal state $\mathcal{G}_n$, the Landau expansion that corresponds to the condensation energy, the term accounting for the spatial variation of the order parameter, $\frac{1}{4m}\left|-i\hbar\nabla\Psi - \frac{2e}{c}\mathbf{A}\Psi\right|^2$ that corresponds to the Gauge invariant kinetic energy, the magnetic energy and the magnetic coupling appearing in the Gibbs free energy. We remind that $\mathbf{H_0}$ is the external magnetic field whereas $\mathbf{H}$ is the exact macroscopic field at a given point. The magnetic vector potential $\mathbf{A}$ will be used more often than $\mathbf{H}$ in the rest of this work. In this construction, several fundamental constants appear as well: m is the electron mass, e its elementary charge and $\hbar$ is the reduced Planck constant.

The value of Ψ describing the superconducting state corresponds to a minimum of the free energy. In presence of magnetic field, we have to find the minimum of $\mathcal{G}$ with respect to both Ψ and $\mathbf{A}$.

Minimization of the Gibbs free energy leads the resolution of two variational problems:

$$\begin{aligned}\delta_{\Psi^*}\mathcal{G} &= \int\left[\alpha\Psi+\frac{\beta}{2}|\Psi|^4+\frac{1}{4m}\left(-i\hbar\nabla-\frac{2e}{c}\mathbf{A}\right)^2\Psi\right]\delta\Psi^* dV \\ &\quad+\oint\left[i\hbar\nabla\Psi+\frac{2e}{c}\mathbf{A}\Psi\right]\delta\Psi^* dS=0 \qquad (2.6)\\ \delta_{\mathbf{A}}\mathcal{G} &= \frac{1}{c}\int\left[\frac{i\hbar e}{2m}(\Psi^*\nabla\Psi-\Psi\nabla\Psi^*)+\frac{2e^2}{mc}|\Psi|^2\mathbf{A}+\frac{c}{4\pi}\mathrm{curlcurl}\mathbf{A}\right]\cdot\delta\mathbf{A}dV \\ &= 0 \qquad (2.7)\end{aligned}$$

that lead to the two GL equations and the De Gennes boundary condition:

$$\begin{aligned}\alpha\Psi+\beta\Psi|\Psi|^2+\frac{1}{4m}\left(i\hbar\nabla+\frac{2e}{c}\mathbf{A}\right)^2\Psi &= 0 \qquad (2.8)\\ -\frac{i\hbar e}{2m}(\Psi^*\nabla\Psi-\Psi\nabla\Psi^*)-\frac{2e^2}{mc}|\Psi|^2\mathbf{A} &= \frac{c}{4\pi}\mathrm{curlcurl}\mathbf{A}=\mathbf{J_s} \qquad (2.9)\\ \left(i\hbar\nabla\Psi+\frac{2e}{c}\mathbf{A}\Psi\right)\cdot\mathbf{n} &= 0, \qquad (2.10)\end{aligned}$$

where $\mathbf{n}$ is the vector normal to the surface. The De Gennes boundary condition (2.10) comes from the minimization of a surface term in the free energy, but can be modified for a contact with a normal metal [2]. It is also remarkable that the superconducting current J_s, defined by the Maxwell equation, turns out to be the quantum mechanical expression for a system of electrons described by a wavefunction Ψ.

2.1.4 Characteristic lengths

In absence of current and field, we can choose a gauge in which Ψ is real. The first GL equation has two solutions which correspond to the description made in section 2.1.1: $\Psi=0$ which corresponds to the normal state and $\Psi^2=-\frac{\alpha}{\beta}=\Psi_0^2$. Using dimensionless units is a common way to find out the characteristic values of an equation. Indeed, writing the first GL equation for the dimensionless order parameter $\psi=\frac{\Psi}{\Psi_0}$, we obtain in the 1D case:

$$-\psi+\psi^3-\frac{\hbar^2}{4m|\alpha|}\frac{d^2\psi}{dx^2} \qquad (2.11)$$

and we immediately see that $\xi=\sqrt{\frac{\hbar^2}{4m|\alpha|}}$ is the characteristic length over which fluctuations of the order parameter occur. For instance, when a normal metal is deposed on a superconductor, the order parameter will decrease at this interface on the scale of ξ. The length ξ is called the coherence length. It is temperature-dependent: $\xi\propto\sqrt{\frac{T_c}{T_c-T}}$.

The second characteristic length is the London penetration depth as seen in section 1.3.2. This length is the characteristic length over which the magnetic field vanishes from the surface of a

superconductor. Indeed, in the case of a superconductor submitted to an external magnetic field, we can find the same solution as in section 1.3.2.3 by taking the curl of the second GL equation (2.10): we obtain

$$\text{curl}\mathbf{J_s} = -\frac{2e^2}{mc}\Psi_0^2\mathbf{H}$$

where $\Psi_0^2 = \frac{|\alpha|}{\beta}$ is the equilibrium value of the order parameter. For a sample occupying the half space defined by $z > 0$ and with $\mathbf{H}$ along the x axis, we find

$$H_x = H_x(0)e^{-z/\lambda_L},$$

where $\lambda_L = \sqrt{\frac{mc^2\beta}{8\pi e^2|\alpha|}}$, is the London penetration depth.

2.1.5 The Ginzburg-Landau parameter κ

The ratio of the two characteristic lengths defines the dimensionless Ginzburg-Landau parameter:

$$\kappa = \frac{\lambda_L}{\xi}. \tag{2.12}$$

Let us consider a superconducting material with $\kappa \ll 1$, submitted to an external magnetic field. As we have $\lambda_L \ll \xi$, the magnetic field penetrates the material to a small depth of the order of λ_L. Yet, Ψ is expected to vary on a much larger length, ξ, since $\lambda_L \ll \xi$. Therefore, to a certain extent, the effect of the magnetic field on the order parameter is insignificant. On the other hand, when $\kappa \gg 1$, the order parameter reacts directly to an external magnetic field and new effects appear.

These effects distinguish the two classes of superconductors: type-I superconductors with $\kappa < \frac{1}{\sqrt{2}}$ and type-II superconductors with $\kappa > \frac{1}{\sqrt{2}}$. The threshold value $\kappa = \frac{1}{\sqrt{2}}$ and description of the type-II superconductors was done by A. A. Abrikosov [14–16].

Nevertheless, in very thin films and very thin wires, as described in [18] and [2], the current is too small to screen the external magnetic field and the London penetration depth should be replaced by the Pearl penetration depth:

$$\lambda_{\text{eff}} = \frac{\lambda_L^2}{d}, \tag{2.13}$$

where d is the thickness of the sample. This is the reason why thin films and nanowires made of type-I superconductors behave as type-II superconductors ($\lambda_L < \frac{\xi}{\sqrt{2}}$, but $\frac{\lambda_L^2}{d} = \lambda_{\text{eff}} > \frac{\xi}{\sqrt{2}}$). As this thesis deals mostly with 1D and 2D geometries, we will only deal with samples which behave as type-II superconductors.

2.1.6 Magnetic flux quantization

Let us consider a superconductor containing a hole. The second GL equation (2.10) gives:

$$\mathbf{J_s} = \frac{\hbar e}{m}|\Psi|^2\nabla\vartheta - \frac{2e^2}{mc}|\Psi|^2\mathbf{A},$$

where ϑ is the phase of the order parameter. If we consider a contour C around the hole so that the distance between the contour and the hole is larger than λ_L, the supercurrent is $J_s = 0$ on the contour and $|\Psi|^2$ is uniform. Therefore, we have

$$\frac{c\hbar}{2e}\oint_C \nabla\vartheta \cdot d\mathbf{l} = \oint_C \mathbf{A} \cdot d\mathbf{l} = \phi.$$

With ϕ being the magnetic flux through the contour C. To keep the value of the order parameter uniquely defined we need $\oint_C \nabla\vartheta \cdot d\mathbf{l} = n2\pi$ with n being an integer.

Therefore, we have

$$\phi = n\phi_0, \tag{2.14}$$

where ϕ_0 is the flux quantum defined by:

$$\phi_0 = \frac{\pi\hbar c}{e} = 2.07 \times 10^{-7}\ \mathrm{G}\cdot\mathrm{cm}^2. \tag{2.15}$$

This result implies the quantization of the magnetic flux in superconductors which is the easiest quantum effect to observe in superconductors. It also confirmed the existence of the BCS Cooper pairs: without the formation of pairs, the flux quantum would be half of the value we calculated here. The magnetic flux quantization is very important in type-II superconductors where vortices carry as well an integer number of flux quanta.

2.1.7 Dimensionless GL equations

We introduce the dimensionless order parameter ψ

$$\Psi_0^2 = n_s/2 = \frac{|\alpha|}{\beta} \tag{2.16}$$

$$\psi = \frac{\Psi}{\Psi_0} \tag{2.17}$$

in the GL equations:

$$\xi^2\left(i\nabla+\frac{2\pi}{\phi_0}\mathbf{A}\right)^2\psi-\psi+\psi|\psi|^2 = 0 \tag{2.18}$$

$$\left(i\nabla+\frac{2\pi}{\phi_0}\mathbf{A}\right)\cdot\mathbf{n}\psi = 0 \tag{2.19}$$

$$-i\frac{\phi_0}{4\pi\lambda_L^2}(\psi^*\nabla\psi-\psi\nabla\psi^*)-\frac{|\psi|^2}{\lambda_L^2}\mathbf{A} = \text{curlcurl}\mathbf{A}. \tag{2.20}$$

The GL equation for the vector potential (2.20) can be simplified by writing $\psi=|\psi|e^{i\vartheta}$:

$$\text{curlcurl}\mathbf{A}=\frac{|\psi|^2}{\lambda_L^2}\left(\frac{\phi_0}{2\pi}\nabla\vartheta-\mathbf{A}\right). \tag{2.21}$$

2.2 Type-II superconductors and vortices

Type-II superconductors were defined by A. A. Abrikosov [14–16]. They do not repel completely an external magnetic field once it reaches a certain value, while remaining in the superconducting state. In type-II superconductors, above the lower critical field H_{c1} the magnetic field H penetrates the bulk in the form of quantized vortex filaments. The number of those vortices in the material increases with H until it reaches the upper critical field H_{c2} where the material switches to normal state (for a bulk sample, superconductivity can still survive on the surface).

2.2.1 Description of a single vortex

An isolated vortex is axially symmetric and its phase changes by $n2\pi$ after a rotation around its axis which we choose as the z axis. Let us describe a superconductor containing a vortex using the GL equations. We assume a cylindrical symmetry of the vortex and choose a solution in the form:

$$\Psi=\Psi_\infty f(r)e^{in\zeta} \tag{2.22}$$

where ζ is the azimuthal angle in the cylindric coordinates (r,ζ,z). We use the gauge invariant magnetic vector potential: $\tilde{\mathbf{A}}=(0,A_\zeta-\frac{n\hbar c}{er},0)$. The equation 2.18 becomes:

$$\xi^2\left(\frac{\partial^2}{\partial r^2}+\frac{1}{r}\frac{\partial}{\partial r}-\frac{4e^2\tilde{A}^2}{\hbar^2c^2}\right)f+f-f^3=0$$

For $r\neq 0$ the second GL equation (2.21) in cylindrical coordinates becomes:

$$\frac{\partial^2\tilde{A}}{\partial r^2}+\frac{1}{r}\frac{\partial\tilde{A}}{\partial r}-\frac{\tilde{A}}{r^2}-\frac{f^2\tilde{A}}{\lambda_L^2}=0$$

We can solve this equation for type-II superconductors ($\kappa \gg 1$). We can indeed approximate $f = 1$ for $r \gg \xi$ and we obtain

$$\tilde{A} = -\frac{n\hbar c}{2e\lambda_L} K_1(r/\lambda_L), \tag{2.23}$$

where $K_1(z)$ is the Bessel function of first order of an imaginary argument. The constant in front of K_1 is chosen so that A_ζ does not diverge for $r \ll \lambda_L$. The magnetic field is

$$H_z = \mathrm{curl}\tilde{\mathbf{A}} = \frac{n\hbar c}{2e\lambda_L^2} K_0(r/\lambda_L),$$

where $K_0(z)$ is the Bessel function of zero order: the magnetic field therefore decreases logarithmically for $r \ll \lambda_L$ and exponentially for $r \gg \lambda_L$. This expression diverges for $r \to 0$: it is indeed not valid in the vicinity of the normal core ($r \approx \xi$). For this region, we approximate by setting a cut-off at $r = \xi$.

We obtain for $r \leqslant \xi$

$$H_z(r) \approx \frac{n\phi_0}{2\pi\lambda_L^2} \ln(\kappa), \tag{2.24}$$

for $\xi < r \ll \lambda_L$,

$$H_z(r) \approx \frac{n\phi_0}{2\pi\lambda_L^2} \ln(\lambda_L/r). \tag{2.25}$$

and for $r \gg \lambda_L$:

$$H_z(r) \approx \frac{n\phi_0}{2\pi\lambda_L^2} \sqrt{\frac{\pi\lambda_L}{2r}} e^{-r/\lambda_L}. \tag{2.26}$$

For the order parameter, in the region $r \ll \lambda_L$, we approximate $\tilde{A} = -\frac{n\hbar c}{2er}$ and we have the equation:

$$\xi^2 \left(\frac{\partial^2}{\partial r^2} + \frac{1}{r}\frac{\partial}{\partial r} - \frac{n^2}{r^2} \right) f + f - f^3 = 0. \tag{2.27}$$

The solution of this equation saturates at the equilibrium value $f = 1$ for $r \gg \xi$ and decreases as $f \propto r^n$ for $r \to 0$. If we linearize by writing $f = 1 - \delta f$, we find for $n = 1$ (we will see later on why vortices with more than one flux quantum aren't favorable):

$$\delta f = \frac{\xi^2}{2r^2}.$$

Last, by linearizing equation 2.27 like previously for $n = 1$, we find for $r \gg \lambda_L$:

$$\delta f = \frac{2e^2\xi^2}{h^2c^2}\tilde{A}^2 = \frac{\xi^2}{2\lambda_L^2} K_1^2(r/\lambda_L).$$

We see here that the core of the vortex which behaves as a normal metal has a size of the order of ξ. In the core of the vortex ($r < \xi$), the order parameter drops from the equilibrium value in the bulk and its modulus vanishes at the vortex axis. A superconducting current surrounds the axis of the vortex and decay away from the core at distances of the order of $r = \lambda_L$ as shown in figure

2.2.

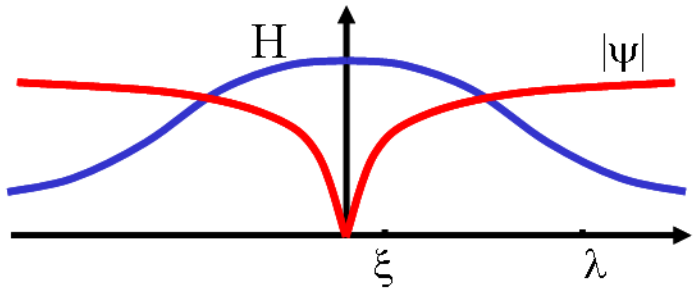

FIGURE 2.2: Structure of a simple vortex. The core region with radius ξ is surrounded by currents. Together with the magnetic field, they decay at distances of the order of λ_L.

2.2.1.1 Vorticity and polarity

The magnetic flux quantization (see 2.1.6) of course applies to vortices which carry an integer number of flux quanta $n\phi_0$. The number of flux quanta n is the vorticity or more generally the winding number. In most situations, however, vortices carry a single flux quantum. Indeed, a simple calculation (see [1]) of the free energy ϵ of a single vortex gives $\epsilon = \left(\frac{n\phi_0}{4\pi\lambda_L}\right)^2 \ln(\kappa)$. The energy is proportional to n^2: it will therefore in general be more favorable to have n vortices containing one flux quantum than a single vortex containing n flux quanta. This is the reason why in general when we talk about vortices, we assume that they are carrying one flux quantum ϕ_0.

The polarity of a vortex is connected to the direction of the magnetic field inside the vortex, or equivalently to the direction of rotation of the superconducting current. Depending on the geometry, the choice to give the positive and negative polarity to a certain direction will be arbitrary or not. We call vortices the flux lines of positive polarity and antivortices the flux lines going in the opposite direction, with negative polarity.

2.2.2 Vortex networks and dynamics

Let us consider a superconductor containing two vortices. The interaction energy may be found in the the same way as the energy for a single vortex [1].

$$\mathcal{F} = \frac{\phi_0}{8\pi}[H(r_1) + H(r_2)], \tag{2.28}$$

where $\mathcal{F}$ is the free energy of the superconductor containing two vortices measured from its energy without vortices and r_1 and r_2 are the coordinates of the centers of each vortex. The magnetic field at the center of each vortex is composed by the addition of its intrinsic field and the field

H_{12} created by the other vortex. It depends only on the distance r between the two vortices. The magnetic field H_{12} created by the other vortex is added to the self field in the case of vortices of the same polarity, but it is subtracted in the case of a vortex and an antivortex.

The free energy of a superconductor containing two vortices is thus composed by the energy of each vortex ϵ and the interaction term. This interaction term is:

$$F_{12} = \frac{\phi_0}{4\pi} H_{12} = \frac{\phi_0^2}{8\pi^2 \lambda_L^2} K_0(\frac{r}{\lambda_L}), \tag{2.29}$$

for vortices of the same polarity and

$$F_{12} = -\frac{\phi_0}{4\pi} H_{12} = -\frac{\phi_0^2}{8\pi^2 \lambda_L^2} K_0(\frac{r}{\lambda_L}). \tag{2.30}$$

for a vortex and an antivortex.

Here, we used the expression for the magnetic field found above, for a single vortex. The interaction is repulsive between vortices of the same polarity and attractive between a vortex and an antivortex. We already commented on the variation of K_0: it decreases as $r^{-1/2}e^{-r/\lambda_L}$ at large distances and varies logarithmically at small distances.

The interaction force can be obtained from the interaction energy: it is simply a particular case of the Lorentz force: the current created by the first vortex exerts a Lorentz force on the second vortex and vice versa. Indeed, any current $\mathbf{J}$ applied to a superconductor will exert a Lorentz force $\mathbf{f_L}$ on the core of the vortex which will be, per unit length,

$$\mathbf{f_L} = \frac{\phi_0}{c}(\mathbf{J} \times \mathbf{e_v}), \tag{2.31}$$

Where $\mathbf{e_v}$ is the unit vector in the direction of the vortex. Due to the repulsion between the vortices, when many vortices are present in a sample, they organize into triangular lattices or less frequently, in rectangular lattices, which correspond to the configuration with lowest energy. The number of vortices depends on the applied magnetic field and the distance between them depends on the structure of the lattice and their number. This vortex lattice was predicted by A. A. Abrikosov [15, 16] and was later confirmed by experiments with different techniques, as shown in Fig. 2.3 and 2.4 (for more details see [19] and [20]).

According to the Faraday law of induction, as soon as vortices start to move, an electric field will be created in the superconductor and therefore, dissipation will take place. Indeed, let us consider a type-II superconductor in an external magnetic field $\mathbf{H}$ with $H_{c1} < H < H_{c2}$. If a transport current is applied to the superconductor in the plane perpendicular to $\mathbf{H}$, the Lorentz force pushes the vortices in the direction perpendicular to the current but still in the same plane according to equation 2.31. At small currents, the vortices will stay pinned on their location

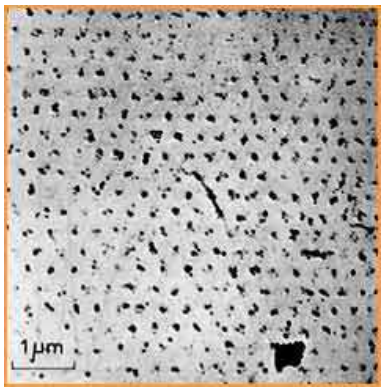

FIGURE 2.3: Evidence of the vortex lattice using a decoration technique in 1967 by U. Essmann and H. Träuble [19].

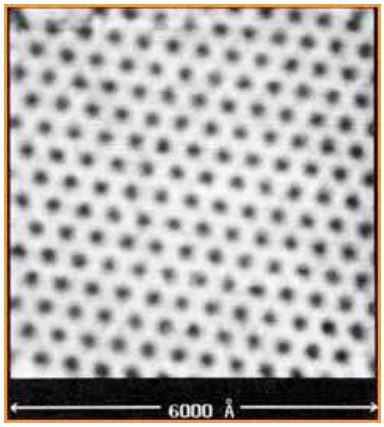

FIGURE 2.4: Image of vortices in $BbSe_2$ made by scanning tunneling microscopy in 1989 by H. F. Hess et al. [20].

if there are impurities or other objects that can act as pinning centers. When the current is increased, the Lorentz force will become stronger than the pinning forces and the vortices move irregularly from one pinning center to the other following the direction imposed by the Lorentz force. This first resistive regime is called "flux creep". At higher currents, the whole lattice moves regularly as a whole and the resistivity stays at a fixed value with increasing current. This regime is called "flux flow". To simplify, during the movement of the vortex lattice, the current has to flow through the vortex core which is resistive. The resistivity can thus be evaluated from the total area corresponding to the normal cores of vortices. The dissipation process during vortex motion is explained by different theories such as the Bardeen-Stephen model [21] (see also [22, 23]). We also need to mention the gyroscopic force that affects a moving vortex and that is comparable to the magnus force. As a result, the motion of the vortex is slightly deflected from the direction imposed by the Lorentz force. The motion of a vortex lattice in the flux flow regime will create an electric field with a component parallel to the current responsible for the resistivity and a (small) component perpendicular to the current that induces a Hall effect. Last, at higher currents, the flux flow regime can be modified by the destruction of the Abrikosov lattice and the formation

of lines of vortices: vortex rivers (see section (5.1.3 for more details). In practical applications, one often tries to minimize the resistivity and therefore, tries to optimize the presence of pinning centers to trap the vortex lattice as efficiently as possible. Pinning centers can also be used to freeze the dynamics of vortices in a certain state as we will see in chapter 5.

2.2.3 The critical magnetic fields

In type-II superconductors, the critical magnetic fields are directly related to the physics of vortices. The first critical field is the field at which the presence of a vortex starts to decrease the global free energy: the presence of a normal region inside the superconductor starts to be favorable. This happens for: $H_{c1} = \frac{4\pi\varepsilon}{\phi_0}$. where ε is the free energy of a superconductor containing one vortex. Calculations [1] give: $H_{c1} = \frac{\phi_0}{4\pi\lambda_L^2}(\ln(\kappa) + 0.08)$.

The second critical field corresponds to the field for which the vortex lattice becomes so dense, that superconductivity can no longer exist between the normal cores of the vortices: the period of the vortex lattice becomes of the order of ξ which is the size of the normal core. This field can be estimated analytically to

$$H_{c2} = \frac{\phi_0}{2\pi\xi^2}. \tag{2.32}$$

2.3 Josephson effects

In 1962, B. Josephson [24] described the effects that appear when two superconductors are connected through a barrier. His idea was to investigate the case when the barrier is small enough to allow the coherence of the superconducting state, which, in the framework of the Ginzburg-Landau theory, means that the phase of the order parameter continues to be coherent across the barrier. Such barriers are called Josephson junctions or "weak links". These weak links can be of different type: tunnel junction, normal metal, constriction of the superconductor or other geometries. For a review on Josephson junctions, see [25].

2.3.1 DC Josephson effect

Let us consider a weak link formed by a narrow constriction of length $L \ll \xi$. In the absence of magnetic field, the first Ginzburg-Landau equation (2.18) is:

$$-\xi^2\nabla^2\psi - \psi + \psi|\psi|^2 = 0. \tag{2.33}$$

Following the derivation of L. G. Aslamazov and A. I. Larkin [26, 27], we consider that the order parameter varies over the length L and we write: $\nabla^2\psi \sim \frac{\psi}{L^2}$. Since the amplitude of the dimensionless order parameter is of the order of one, we consider only the first term in the equation and we have the Laplace equation:

$$\nabla^2\psi = 0. \tag{2.34}$$

Writing $\psi = \psi_1 e^{i\theta_1}$ in the part before the constriction far away from it and $\psi = \psi_2 e^{i\theta_2}$ in the other part, the solution should be in the form:

$$\psi = \psi_1 e^{i\theta_1} f(r) + \psi_2 e^{i\theta_2}(1 - f(r)), \tag{2.35}$$

where r is the coordinate corresponding to the axis of the superconductor.

The solution must satisfy as well

$$\nabla^2 f(r) = 0. \tag{2.36}$$

A solution exists and using the expression from (2.35) and the expression of the supercurrent from the Ginzburg-Landau equations we find:

$$J_s = \frac{|\alpha|\hbar e}{\beta m}\Im(\psi^*\nabla\psi) = J_{jc}\sin\Delta\theta. \tag{2.37}$$

Here, $\Im(z)$ denotes the imaginary part of the complex number z. We therefore have a relation between the superconducting current and the phase difference $\Delta\theta$ across the junction. We also note that we defined a certain critical current J_{jc} which determines the maximum current that can flow through the particular junction. This is the first Josephson effect or DC Josephson effect: a current can flow (or even tunnel in the case of such a junction) through a barrier without voltage or dissipation. Between two superconductors connected by a weak link, a supercurrent may continue to flow. This effect is characteristic of the Josephson coupling: the coherence streches beyond the weak link.

2.3.2 AC Josephson effect

When the current through the superconductor is too strong for the "capacity " of the weak link, the charges start to accumulate on the border of the junction and a voltage appears. If we write the Schrödinger equation from both sides of the junction, we have:

$$i\hbar\frac{\partial\psi_1}{\partial t} = E_1\psi_1 \tag{2.38}$$

and

$$-\hbar\frac{\partial\theta_1}{\partial t} + \hbar\frac{\partial\theta_2}{\partial t} = E_1 - E_2. \tag{2.39}$$

Last, we write that the difference between the energies is only the result of the potential V and we obtain the second Josephson relation:

$$\hbar \frac{\partial \Delta\theta}{\partial t} = 2eV. \tag{2.40}$$

This equation is commonly referred to as the Josephson equation. If a constant current $I > I_c$ is applied, a voltage will appear and since the supercurrent is limited to I_c, a normal current will flow through the junction. Let us write R the resistance of the weak link. The total current through the junction is:

$$I = I_c \sin \Delta\theta + \frac{\hbar}{2eR} \frac{\partial \Delta\theta}{\partial t} \tag{2.41}$$

By integrating this equation and using the result in the second Josephson equation (2.40), we have:

$$V(t) = R \frac{I^2 - I_c^2}{I + I_c \cos \omega t}, \tag{2.42}$$

where $\omega = \frac{2e}{\hbar} R \sqrt{I^2 - I_c^2}$. Therefore, applying a current strong enough to a Josephson junction will have for effect to induce an oscillating voltage. This is the AC Josephson effect.

2.3.3 Superconducting Quantum Interference Devices (SQUID)

The first SQUID was invented in 1964 by Robert Jaklevic, John Lambe, Arnold Silver and James Mercereau, that is just two years after the Josephson effects were predicted. The design of the device is rather simple: it is based on a superconducting ring containing a single Josephson junction for the RF SQUID and two junctions for the DC SQUID. SQUIDs are mostly used as magnetometers with sensitivities reaching $\sim 10^{-10}$ G. They can also be used as precision voltmeters.

The idea is that when a magnetic field is applied and creates a flux through the ring, a current will flow in the ring in order to satisfy the flux quantization condition. Yet, the junctions in the ring have very low critical current and will therefore not sustain a superconducting current large enough for that. The effects happening in the field can be considered as interferences between the current which would screen the magnetic flux to satisfy the flux quantization condition and the limitations induced by the presence of the weak link (the critical current of the junction). For instance, in a DC SQUID, the current flowing through the ring will depend greatly on the magnetic flux penetrating the ring: it will increase from 0 to its maximum value for a rise of only half of a flux quantum. See [1] and references therein for a more detailed descriptions of SQUIDs.

2.4 Time-dependent Ginzburg-Landau theory

The solutions of the Ginzburg-Landau equations describe the superconducting state in equilibrium. Our goal is to investigate the dynamics during the transition between different stationary states and we therefore need time-dependent equations.

2.4.1 The principles of the time-dependent Ginzburg-Landau equations

Different versions of time-dependent equations based on the Ginzburg-Landau equations have been developed (see [28] for an overview of the different developments). The first versions are probably those of A. Schmidt [29] and of E. Abrahams and T. Tsuneto [30]. Here, we follow the derivations that can be found in [22], [31–33] and [34]. In equilibrium, the free energy of a superconductor is at its minimum regarding the order parameter Ψ and satisfies

$$\frac{\delta F}{\delta \Psi^*} = 0. \tag{2.43}$$

The leading idea of time-dependent derivations is to consider that the order parameter is driven out of equilibrium and that it will relax with a certain rate that depends on its deviation from equilibrium:

$$-\gamma\hbar\frac{\partial \Psi}{\partial \tau} = \frac{\delta F}{\delta \Psi^*}, \tag{2.44}$$

where γ is a positive constant and τ is the time.

The electrostatic potential χ and the magnetic vector potential defined by

$$\mathbf{E} = -\frac{1}{c}\frac{\partial \mathbf{A}}{\partial \tau} - \nabla\chi \tag{2.45}$$

$$\mathbf{H} = \mathrm{curl}\mathbf{A}, \tag{2.46}$$

preserve the gauge invariance of the electromagnetic fields $\mathbf{E}$ and $\mathbf{H}$ but equation 2.44 should be corrected to preserve gauge invariance as well:

$$\gamma\left(\hbar\frac{\partial \Psi}{\partial \tau} + 2ie\chi\Psi\right) = -\frac{\delta F}{\delta \Psi^*}. \tag{2.47}$$

Deriving the free energy from (2.6), we obtain the first TDGL equation:

$$-\gamma\left(\hbar\frac{\partial \Psi}{\partial \tau} + 2ie\chi\Psi\right) = \alpha\Psi + \beta\Psi|\Psi|^2 + \frac{1}{4m}\left(i\hbar\nabla + \frac{2e}{c}\mathbf{A}\right)^2\Psi$$

The non-equilibrium situation modifies the second GL equation (2.10), by introducing the possibility of a normal current $\mathbf{J_n}$ due to variations of the electric field. The expressions for the different

currents, where σ_n is the normal conductivity (e.g. measured above T_c) are:

$$\mathbf{J} = \frac{c}{4\pi}\text{curl}\mathbf{H} = \frac{c}{4\pi}\text{curlcurl}\mathbf{A} \tag{2.48}$$

$$\mathbf{J_s} = -\frac{ie\hbar}{m}(\Psi^*\nabla\Psi - \Psi\nabla\Psi^*) - \frac{4e^2}{mc}\mathbf{A}|\Psi|^2 \tag{2.49}$$

$$\mathbf{J_n} = -\sigma_n\left(\frac{1}{c}\frac{\partial\mathbf{A}}{\partial\tau} + \nabla\chi\right), \tag{2.50}$$

and the second TDGL equation is simply the decomposition of the total current $\mathbf{J}$ into the superconducting current $\mathbf{J_s}$ and the normal current $\mathbf{J_n}$:

$$\mathbf{J} = \mathbf{J_s} + \mathbf{J_n}. \tag{2.51}$$

We obtain the simplest version of the time-dependent Ginzburg-Landau (TDGL) equations:

$$-\gamma\left(\hbar\frac{\partial\Psi}{\partial\tau} + 2ie\chi\Psi\right) = \alpha\Psi + \beta\Psi|\Psi|^2 + \frac{1}{4m}\left(i\hbar\nabla + \frac{2e}{c}\mathbf{A}\right)^2\Psi \tag{2.52}$$

$$\frac{c}{4\pi}\nabla\times(\nabla\times\mathbf{A}) = -\sigma_n\left(\frac{1}{c}\frac{\partial\mathbf{A}}{\partial\tau} + \nabla\chi\right) - \frac{ie\hbar}{2m}(\Psi^*\nabla\Psi - \Psi\nabla\Psi^*) - \frac{2e^2}{mc}\mathbf{A}|\Psi|^2. \tag{2.53}$$

The total current $\mathbf{J}$ also obeys the continuity equation for the conservation of the charge:

$$\text{div}\mathbf{J} + \frac{e\partial n_e}{\partial\tau} = 0, \tag{2.54}$$

where n_e is the density of electrons. As the plasma frequency is much greater than the characteristic frequency of the superconducting electrons, we can neglect the variations in the density of electrons $\frac{\partial n_e}{\partial\tau}$ [22, 34]. We obtain the electroneutrality equation:

$$\text{div}\mathbf{J} = 0. \tag{2.55}$$

The TDGL equations were derived from the microscopic theory in the case of so-called gapless superconductors, where pair breaking interactions are so strong that the energy gap vanishes from the excitation spectrum [35, 36]. Strictly speaking the range of validity of the TDGL theory is thus much more limited than for the stationary GL theory: the relaxation rate in the superconductor needs as well to be sufficiently fast which for some mechanisms means that the temperature needs to be very close to T_c.

2.4.2 Generalized TDGL equations

A generalized version of the TDGL equations was derived from the microscopic theory by L. Kramer and R. J. Watts-Tobin [37] to extend the validity to dirty superconductors with a finite

gap. Here we give a simple description of the derivation.

The relaxation equation (2.47) written as such considers that the relaxation rates of the order parameter and of the electrostatic potential are the same. This hypothesis can seem to be an oversimplification and one can divide the real and imaginary part of equation (2.47), by decomposing the order parameter $\Psi = |\Psi|e^{i\vartheta}$ into its amplitude and phase. Moreover, we use the gauge invariant potentials:

$$\tilde{\mathbf{A}} = \mathbf{A} - \frac{c\hbar}{2e}\nabla\vartheta \tag{2.56}$$

$$\tilde{\chi} = \chi + \frac{\hbar}{2e}\frac{\partial\vartheta}{\partial t}. \tag{2.57}$$

With the two different positive factors $\gamma_{|\Psi|}$ and γ_χ, we have:

$$-\gamma_{|\Psi|}\hbar\frac{\partial|\Psi|}{\partial t} = \Re\left(\frac{\delta F}{\delta\Psi^*}e^{-i\vartheta}\right) \tag{2.58}$$

$$-\gamma_\chi|\Psi|2e\tilde{\chi} = \Im\left(\frac{\delta F}{\delta\Psi^*}e^{-i\vartheta}\right) \tag{2.59}$$

and using the expression of the free energy, we obtain:

$$\gamma_{|\Psi|}\hbar\frac{\partial|\Psi|}{\partial t} = \alpha|\Psi| + \beta|\Psi|^3 + \frac{1}{4m}\left(\hbar^2\nabla^2 - \frac{4e^2}{c^2}\tilde{\mathbf{A}}\right)^2|\Psi| \tag{2.60}$$

$$-\gamma_\chi|\Psi|^2\tilde{\chi} = \frac{1}{4m}\nabla\cdot(|\Psi|^2\tilde{\mathbf{A}}). \tag{2.61}$$

The microscopic calculations (see [31–33]) imply that factors $\gamma_{|\Psi|}$ and γ_χ depend on the value of the order parameter:

$$\gamma_{|\Psi|} = c_1\sqrt{1 + c_2|\Psi|^2}$$

$$\gamma_\chi = c_1\frac{1}{\sqrt{1 + c_2|\Psi|^2}}$$

Here c_1 and c_2 are the constants appearing in the derivation from the microscopic theory. In dimensionless units and under certain conditions, equations (2.60) and (2.61) can be written with the dimensionless complex order parameter $\psi = \Psi/\Psi_0$, time $t = \tau/\tau_{\mathrm{GL}}$, with $\tau_{\mathrm{GL}} = \frac{\pi\hbar}{8k_B(T_c - T)}$, the distance is measured in units of the coherence length ξ, vector potential $\mathbf{a} = \frac{2\pi\xi\mathbf{A}}{\phi_0}$ (where $\phi_0 = \frac{\pi\hbar c}{e}$ is the flux quantum and k_B is the Boltzmann constant) and electrostatic potential $\Phi = \chi\frac{2e\tau_{\mathrm{GL}}}{\hbar}$. The equations (2.60) and (2.61) then yield:

$$\frac{u}{\sqrt{1 + \Gamma^2|\psi|^2}}\left(\frac{\partial\psi}{\partial t} + i\Phi\psi + \frac{1}{2}\Gamma^2\psi\frac{\partial|\psi|^2}{\partial t}\right) = \psi - \psi|\psi|^2 + (i\nabla + \mathbf{a})^2\psi, \tag{2.62}$$

where u is a temperature independent parameter ($u = 5.79$ according to the microscopic derivation in [37]) and Γ is the temperature-dependent pair breaking parameter (see [31–33] for a more detailed explanation of the derivation). The generalized time-dependent Ginzburg-Landau equations are equivalent to the simple TDGL equations when $\Gamma \to 0$ which corresponds to $T \to T_c$.

Chapter 3

Mathematical analysis of the time-dependent Ginzburg-Landau equations

In this chapter, we write the time-dependent Ginzburg-Landau (TDGL) equations in a dimensionless form and derive the main general results concerning stability that we will need to study the forthcoming physical problems.

3.1 Inhomogeneous coefficients in the Ginzburg-Landau equations

The TDGL equations are often used in their dimensionless form and the characteristics of the material as well as the universal constants are included in the dimensionless variables, making it easier for analysis and computations. In this section we take into account inhomogeneous superconductors provided that the scale of the inhomogeneities is much larger than the coherence length. The sample could also be composed of an assembly of different materials like in the case of Josephson junctions (see section 2.3).

We use here the simple version of the TDGL equations [29] as described in section 2.4. It includes the presence of the magnetic field by using the vector potential $\mathbf{A}$. The electric field is described

by the electrostatic potential χ. We recall Eqs. (2.52) and (2.53):

$$\begin{aligned} -\gamma\left(\hbar\frac{\partial\Psi}{\partial\tau}+2ie\chi\Psi\right) &= \alpha\Psi+\beta\Psi|\Psi|^2+\frac{1}{4m}\left(i\hbar\nabla+\frac{2e}{c}\mathbf{A}\right)^2\Psi \\ \frac{c}{4\pi}\nabla\times(\nabla\times\mathbf{A}) &= -\sigma_n\left(\frac{1}{c}\frac{\partial\mathbf{A}}{\partial\tau}+\nabla\chi\right)-\frac{ie\hbar}{2m}(\Psi^*\nabla\Psi-\Psi\nabla\Psi^*)-\frac{2e^2}{mc}\mathbf{A}|\Psi|^2, \end{aligned}$$

where γ is a positive constant accounting for the relaxation of the order parameter. $\Psi(\mathbf{S},\tau)=|\Psi|e^{i\vartheta}$ is the Ginzburg-Landau order parameter which depends on the spatial coordinate $\mathbf{S}$ and the time τ. m and e are the electron mass and charge, σ_n is the conductivity of the normal state (measured above the critical temperature T_c), $\hbar$ the reduced Planck constant and c the speed of light. Last, α and β are the coefficients appearing in the Ginzburg-Landau theory (see section 2.4).

The values of the parameters γ, σ_n, α, β, ξ, λ_L and κ are characteristics of the material. Therefore, in the case of a non-homogeneous sample, they are functions of the spatial coordinate $\mathbf{S}$. They can as well be function of some external parameter (like temperature) which does depend on the time τ. Those parameters are not all independent between them: they obey relations derived in chapter 2. We normalize these parameters by introducing a new set of constants and dimensionless functions:

$$\begin{aligned} \gamma(\mathbf{S},\tau) &= \gamma_0\gamma_r(\mathbf{S},\tau) && \text{, with } 0 \le \gamma_r \le 1 \\ \sigma_n(\mathbf{S},\tau) &= \sigma_r(\mathbf{S},\tau)\sigma_0 && \text{, with } 0 \le \sigma_r \le 1 \\ \alpha(\mathbf{S},\tau) &= |\alpha_0|\alpha_r(\mathbf{S},\tau) && \text{, with } -1 \le \alpha_r \le \infty \\ \beta(\mathbf{S},\tau) &= \beta_0\beta_r(\mathbf{S},\tau) && \text{, with } 0 \le \beta_r \le 1 \\ \xi(\mathbf{S},\tau) &= \xi_0\xi_r(\mathbf{S},\tau) && \text{, with } 0 \le \xi_r \le 1 \\ \lambda_L(\mathbf{S},\tau) &= \lambda_0\lambda_r(\mathbf{S},\tau) && \text{, with } 0 \le \lambda_r \le 1 \\ \kappa(\mathbf{S},\tau) &= \kappa_0\kappa_r(\mathbf{S},\tau) && \text{, with } 0 \le \kappa_r \le 1. \end{aligned} \tag{3.1}$$

The values of γ_0, σ_0, $|\alpha_0|$, β_0, λ_0, ξ_0 and κ_0 are the highest values of respectively γ, σ_n, $|\alpha|$, β, λ_L, ξ and κ that can be found in the material (α_0 is the lowest value of α for $T<T_c$). γ_r, σ_r, α_r, β_r, λ_r, ξ_r and κ_r are the dimensionless functions obtained after normalization. α_r is negative for temperatures below the corresponding T_c.

We define the following dimensionless variables: vector potential $\mathbf{a}=\frac{2\pi\xi_0\mathbf{A}}{\phi_0}$ ($\phi_0=\frac{\pi\hbar c}{e}$ is the flux quantum), time $t=\frac{c^2}{4\pi\lambda_{\text{eff}}^2\sigma_0}\tau=\frac{\tau}{\tau_\theta}$, spatial coordinate $\mathbf{s}=\frac{\mathbf{S}}{\xi_0}$, electrostatic potential $\Phi=\chi\frac{2e\tau_\theta}{\hbar}$ and order parameter $\psi=\Psi\sqrt{\frac{\beta_0}{|\alpha_0|}}=\rho(\mathbf{s},t)e^{i\theta(\mathbf{s},t)}$.

The Pearl penetration depth [18] $\lambda_{\text{eff}}=\frac{\lambda_L}{d^2}$ has been used instead of the London penetration depth $\lambda_L=\sqrt{\frac{mc^2\beta}{8\pi e^2|\alpha|}}$ since the thickness $d\ll\lambda_L$ is small. The coherence length is defined as $\xi=\sqrt{\frac{\hbar^2}{4m|\alpha|}}$.

While putting the equations in the dimensionless form, two characteristic time scales emerge [34]. The first one, $\tau_\rho = \frac{\gamma_0 \hbar}{|\alpha_0|}$, corresponds to the characteristic relaxation time of the amplitude of the order parameter as can be seen by taking the real part of equation (2.52). The microscopic theory evaluates this characteristic time to the Ginzburg-Landau time τ_{GL}:

$$\tau_\rho = \tau_{GL} = \frac{\pi \hbar}{8(T_c - T)}. \tag{3.2}$$

The second characteristic time τ_θ accounts for the dynamics of the phase. It is revealed from the equation for the current (2.53): the time derivative of the magnetic vector potential is linked to the current which is itself determined by the phase of the order parameter.

The ratio between those two characteristic times is the only dimensionless parameter left in the equations with uniform coefficients: $u = \frac{\tau_\rho}{\tau_\theta}$. The estimates from microscopic theories give the value of u ranging from 5.79 [29, 37] to 12 [23, 35, 36]. However, we consider here the general case where $0 < u < \infty$.

The functions defined in Eq. (3.1) have been introduced in the most general form and can describe a large variety of situations. However, one needs to take care that the variations introduced in these functions are compatible with the TDGL equations. For instance, a reasonable condition for these coefficients is to restrict the spatial variations to scales much larger than ξ and to restrict the time variations to timescales much larger than τ_{GL}. The first equation in dimensionless units reads:

$$\gamma_r u \left(\frac{\partial \psi}{\partial t} + i\Phi\psi \right) = -\alpha_r \psi - \beta_r \psi |\psi|^2 - (i\nabla + \mathbf{a})^2 \psi \tag{3.3}$$

The second equation is the decomposition of the total current into the superconducting and the normal current:

$$\nabla \times (\nabla \times \mathbf{a}) = \frac{1}{\kappa_0^2} \left[-\frac{i}{2}(\psi^* \nabla\psi - \psi \nabla\psi^*) - \mathbf{a}|\psi|^2 - \sigma_r \left(\frac{\partial \mathbf{a}}{\partial t} + \nabla\Phi \right) \right]. \tag{3.4}$$

The total current $\mathbf{j} = \nabla \times (\nabla \times \mathbf{a})$ is the sum of the superconducting current $\mathbf{j_s} = -\frac{i}{2}(\psi^* \nabla\psi - \psi\nabla\psi^*) - \mathbf{a}|\psi|^2$ and the normal current $\mathbf{j_n} = -\sigma_r \left(\frac{\partial \mathbf{a}}{\partial t} + \nabla\Phi \right)$ in dimensionless units.

The dimensionless total current also obeys the electroneutrality equation (2.55):

$$\mathrm{div}\mathbf{j} = 0. \tag{3.5}$$

which can be used to simplify equation (3.4), as we will see later on. One can also write it depending on the variation of the coherence length. Indeed, we have $\xi_r = \sqrt{\frac{1}{|\alpha_r|}}$. Dividing both sides of equation (3.3) by $|\alpha_r|$, we have:

$$\frac{\gamma_r}{|\alpha_r|} u \left(\frac{\partial \psi}{\partial t} + i\Phi\psi \right) = -\frac{\alpha_r}{|\alpha_r|}\psi - \frac{\beta_r}{|\alpha_r|}\psi|\psi|^2 - \xi_r^2 (i\nabla + \mathbf{a})^2 \psi$$

Moreover, adding the conditions: $\gamma_r = |\alpha_r|$, $\alpha_r = -|\alpha_r|$, $\beta_r = |\alpha_r|$, we obtain an equation corresponding to the situation where the coherence length is varying throughout the sample:

$$u\left(\frac{\partial\psi}{\partial t} + i\Phi\psi\right) = \psi - \psi|\psi|^2 - \xi_r^2(i\nabla + \mathbf{a})^2\psi. \tag{3.6}$$

3.2 Stationary solutions

For the sake of clarity, we present here the stationary solutions in the homogeneous case ($\alpha_r = -1$ and $\beta_r = \gamma_r = \sigma_r = 1$). The derivation including these coefficients can be found in appendix C.

3.2.1 The Complex Ginzburg-Landau equation

The first TDGL equation (3.3) is very similar to the more general complex Ginzburg-Landau (CGL) equation which is often studied in the form:

$$\frac{\partial\psi}{\partial t} = \psi + (1 + ic_1)\nabla^2\psi - (1 + ic_2)|\psi|^2\psi. \tag{3.7}$$

Our equation is the CGL equation with real coefficients ($c_1 = c_2 = 0$) and with adding the electrostatic potential and magnetic field. For a review on the CGL equation, see [38] for example. Here we assume that the material is in the superconducting state.

3.2.2 The 1D case

The stationary solutions of the CGL equation have been studied in details [38, 39] and in 1D, one can derive the conditions of the Eckhaus type instability. Here, we derive the stationary solutions for our equations which includes magnetic field, electrostatic potential and the possibility of inhomogeneities. We used a similar method as what is used for the CGL equation with real coefficients.

Indeed, we can rewrite equation (3.3) in the same way as in [39] by separating real and imaginary parts:

$$u\frac{\partial\rho}{\partial t} = \frac{\partial^2\rho}{\partial x^2} + \rho\left[1 - \rho^2 - \left(a - \frac{\partial\theta}{\partial x}\right)^2\right] \tag{3.8}$$

and

$$u\rho\left(\frac{\partial\theta}{\partial t} + \Phi\right) = \frac{1}{\rho}\frac{\partial}{\partial x}\left[\rho^2\left(\frac{\partial\theta}{\partial x} - a\right)\right], \tag{3.9}$$

where ρ is the amplitude, θ the phase of the complex order parameter $\psi = \rho e^{i\theta}$ and x is the longitudinal dimensionless spatial coordinate.

We recognize in Eq. (3.9) the superconducting current

$$|\mathbf{j_s}| = j_s = -\frac{i}{2}\left(\psi^*\frac{\partial\psi}{\partial x} - \psi\frac{\partial\psi^*}{\partial x}\right) - a|\psi|^2 = \rho^2\left(\frac{\partial\theta}{\partial x} - a\right), \tag{3.10}$$

and we will therefore be able to use the electroneutrality condition (3.5).

We can use the common mechanical analogy to describe the stationary solutions of equations (3.8) and (3.9) by rewriting them in the form:

$$\frac{\partial^2\rho}{\partial x^2} = -\frac{\partial U(\rho)}{\partial\rho} \tag{3.11}$$

with

$$U = \frac{1}{2}\left(\frac{j_s^2}{\rho^2} + \rho^2 - \frac{1}{2}\rho^4\right). \tag{3.12}$$

These equations describe the motion of a particle with spatial coordinate ρ in the field U. In this analogy, the time is represented by x.

3.2.2.1 Case $j_s \neq 0$

We see that $\lim_{\rho^2\to\infty} U = -\infty$ and $\lim_{\rho^2\to 0} U = \infty$. Bounded solutions of Eq. (3.11) exist if and only if U has local extrema and has the shape sketched in Fig. 3.1. The condition for U to have local

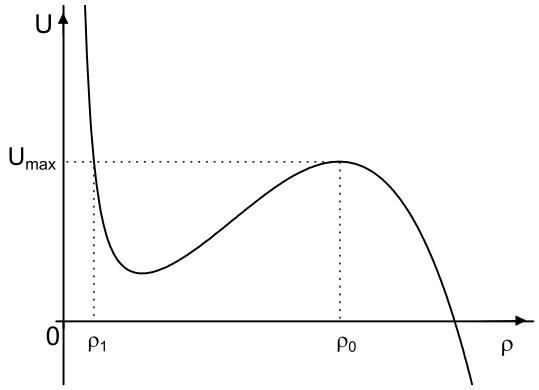

FIGURE 3.1: The potential $U = \frac{1}{2}\left(\frac{j_s^2}{\rho^2} + \rho^2 - \frac{1}{2}\rho^4\right)$. For $j_s < j_c$, there is a local maximum and minimum and stationary solutions can be seen as either stable states or oscillating states in the potential well.

extrema is

$$\frac{\partial U}{\partial\rho} = \frac{1}{\rho^3}\left(-j_s^2 + \rho^4 - \rho^6\right) = 0.$$

Therefore ρ must satisfy:

$$\rho^4(1-\rho^2) = j_s^2. \tag{3.13}$$

By studying the shape of $\rho^4(1-\rho^2)$, which has a local maximum for $\rho^2 = \frac{2}{3}$ (see Fig. 3.2), we find that the condition (3.13) is only achievable if:

$$j_s^2 < j_c^2, \tag{3.14}$$

with

$$j_c = \frac{2}{\sqrt{27}} \tag{3.15}$$

which is the definition of the Ginzburg-Landau critical (depairing) current. Indeed, the critical current is calculated from the uniform stationary state of the GL equations for which the superconducting current is $j_s = \rho^2\sqrt{1-\rho^2}$. For $j_s > j_c$, the only uniform stationary solution is $\rho = 0$: the superconductivity is destroyed. For $j_s < j_c$, there are two different solutions possible which define the two branches seen in Fig. 3.2. They correspond to

$$\rho > \sqrt{\frac{2}{3}} \tag{3.16}$$

and

$$\rho < \sqrt{\frac{2}{3}}. \tag{3.17}$$

The stability of each branch can be deduced from thermodynamical arguments (see [1] for example) or by further stability analysis as we will see in section 3.3.2.2. Surprisingly, the stable solution is the one satisfying Eq. (3.16) which corresponds to the local maximum of U.

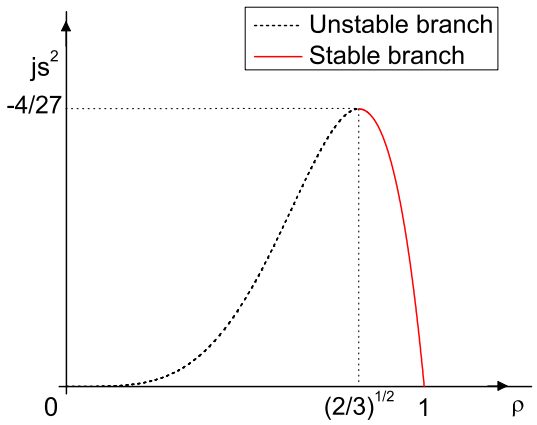

FIGURE 3.2: The superconducting current $|\mathbf{j_s}|^2 = \rho^4(1-\rho^2)$. It defines as well the Ginzburg-Landau critical (depairing) current $j_c = \frac{2}{\sqrt{27}}$. A further analysis also determines which part of the curve corresponds to the stable branch.

The local extrema of U correspond to solutions which satisfy $\frac{\partial^2\rho}{\partial x^2} = 0$ and in particular, solutions of uniform amplitude. They are described by:

$$\rho = \sqrt{1-Q^2}\ \text{, with } Q = \frac{j_s}{\rho^2} = \frac{\partial\theta}{\partial x} - a, \tag{3.18}$$

under the condition that

$$1 - Q^2 = 1 - \left(\frac{\partial\theta}{\partial x} - a\right)^2 \geq 0. \tag{3.19}$$

This condition restricts the intensity of the magnetic field and even more accurately the gauge invariant vector potential $a - \frac{\partial\theta}{\partial x}$. Moreover, when a is uniform, Eq. (3.5), $\frac{\partial}{\partial x}\left[\rho^2\left(\frac{\partial\theta}{\partial x} - a\right)\right] = 0$ leads to

$$\begin{cases} \frac{\partial^2\theta}{\partial x^2} & = & 0 \\ \text{or} & & \\ \frac{\partial\theta}{\partial x} & = & \pm\sqrt{\frac{1}{3}} - a. \end{cases} \tag{3.20}$$

Therefore, we write $\frac{\partial\theta}{\partial x} = k$, and

$$j_s = \left(\frac{\partial\theta}{\partial x} - a\right)\left[1 - \left(\frac{\partial\theta}{\partial x} - a\right)^2\right]. \tag{3.21}$$

Last, we obtain a family of solutions in the well known twisted plane wave form:

$$\psi_k = \sqrt{1 - (a-k)^2}\, e^{ikx + \theta_0} \tag{3.22}$$

where k and θ_0 are real constants.

3.2.2.2 Case $j_s = 0$

In this case, the potential becomes $U_0 = \frac{1}{2}(\rho^2 - \frac{1}{2})$ with $\lim_{\rho^2\to\infty} U_0 = -\infty$ and $\lim_{\rho^2\to 0} U_0 = 0$. The shape of U_0 is plotted in Fig. 3.3. Solutions satisfying $\frac{\partial U}{\partial \rho} = 0$ have simply:

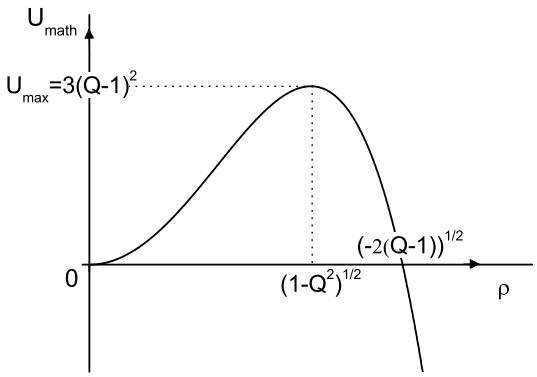

FIGURE 3.3: The potential U_{math} as a function of the amplitude ρ. The shape and values correspond as well to the case $j_s = 0$ by applying $Q = 0$.

$$\rho_0 = 1 \tag{3.23}$$

and when a is uniform, $j_s = 0$ requires the stationary solution to be in the form

$$\psi_0 = e^{iax+\theta_0}, \tag{3.24}$$

which is in agreement with Eq. (3.22).

3.2.2.3 Comments on this analysis

The choice to write the potential $U = \frac{1}{2}\left(\frac{j_s^2}{\rho^2} + \rho^2 - \frac{1}{2}\rho^4\right)$ brings a very beautiful way to describe many particular solutions of the CGL and TDGL equations as we will discuss in section 4.1.2. Indeed, common "interesting" solutions will be seen as reflecting the periodic or oscillating movement of the particle in the potential well. However, this choice can be misleading, because of the "diverging limiting case" and because j_s does depend on ρ. Moreover if its expression is substituted, a sign problem emerges. A more purely mathematical way of treating the problem would be to write the potential $U_{\text{math}} = \frac{1}{2}\left[-\rho^2\left(\left[\frac{\partial\theta}{\partial x} - a\right]^2 - 1\right) - \frac{1}{2}\rho^4\right]$. The shape of the potential, plotted in Fig. 3.3 does this time converge with the shape of U_0. Solutions corresponding to $\frac{\partial U_{\text{math}}}{\partial \rho} = 0$ are consistent with the ones found before, but in this case, the requirement to have $j_s < j_c$ does not emerge, although it can be brought up artificially.

3.2.3 The 2D case

The 2D case is treated similarly, bringing only minor modifications to the derivation. It could easily be extended to the third dimension as well. The separation of real and imaginary part of (3.3) gives

$$u\frac{\partial\rho}{\partial t} = \frac{\partial^2\rho}{\partial x^2} + \frac{\partial^2\rho}{\partial y^2} + \rho\left[1 - \rho^2 - \left(\frac{\partial\theta}{\partial x} - a_x\right)^2 + \left(\frac{\partial\theta}{\partial y} - a_y\right)^2\right] \tag{3.25}$$

and

$$u\rho\left(\frac{\partial\theta}{\partial t} + \Phi\right) = \frac{1}{\rho}\frac{\partial}{\partial x}\left[\rho^2\left(\frac{\partial\theta}{\partial x} - a_x\right)\right] + \frac{1}{\rho}\frac{\partial}{\partial y}\left[\rho^2\left(\frac{\partial\theta}{\partial y} - a_y\right)\right], \tag{3.26}$$

where ρ is the amplitude, θ the phase of the complex order parameter ψ, x and y are the longitudinal dimensionless spatial coordinates, a_x and a_y are the components of the magnetic vector potential.

The mechanical analogy can still be used by writing the stationary solutions as:

$$\nabla^2\rho = -\frac{\partial U(\rho)}{\partial\rho} \tag{3.27}$$

with

$$U = \frac{1}{2}\left(\frac{j_s^2}{\rho^2} + \rho^2 - \frac{1}{2}\rho^4\right), \tag{3.28}$$

and

$$\mathbf{j_s} = \rho^2(\nabla\theta - \mathbf{a}). \tag{3.29}$$

The continuity equation yields $\nabla \cdot \mathbf{j_s} = 0$.

The value of the critical current is the same as before and solutions such as $\frac{\partial U}{\partial \rho} = 0$ which include all stationary solutions are described by

$$\rho = \sqrt{1 - \mathbf{Q}^2}\ , \text{ with } \mathbf{Q} = \frac{\mathbf{h}}{\rho^2} = \nabla\theta - \mathbf{a}, \tag{3.30}$$

under the condition that

$$1 - (\nabla\theta - \mathbf{a})^2 \geq 0 \tag{3.31}$$

For uniform solutions in ρ, the electroneutrality condition (3.5) gives here $\nabla^2\mathbf{j_s} = 0$. With the added hypothesis $\frac{\partial^2\theta}{\partial x^2} = \frac{\partial^2\theta}{\partial y^2} = 0$, we can write the uniform stationary solutions for the 2D case:

$$\psi_{k,p} = \sqrt{1 - (k\mathbf{e_x} + p\mathbf{e_y} - \mathbf{a})^2}e^{i(kx+py+\theta_0)}, \tag{3.32}$$

where ($\mathbf{e_x}$,$\mathbf{e_y}$) is the standard unitary basis of the 2D space and (k, p) are real constants.

3.3 Stability of the stationary solutions

We study the stability of the stationary solutions. We start the analysis by writing the equations for all stationary solutions but restrict our focus to the particular solutions of uniform amplitude found previously.

3.3.1 Linearizing the equations

The first step to study the stability of a particular solution $\psi_{k,p}$ is to linearize the time-dependent equations regarding small fluctuations of the order parameter.

$$\delta\psi(\mathbf{s}, t) = f(\mathbf{s}, t) = \psi(\mathbf{s}, t) - \psi_{k,p}. \tag{3.33}$$

The electrostatic potential Φ is of the order of $\delta\psi$, as seen for example from Eq. (3.26): close to the equilibrium, the potential appears with the variation of the density of electrons. Neglecting terms of order 2 and higher in $\delta\psi$, we have:

$$\psi|\psi|^2 = 2|\psi_{k,p}|^2 f + \psi_{k,p}^2 f^* + |\psi_{k,p}|^2\psi_{k,p}.$$

The first TDGL equation (3.3) becomes:

$$u(\dot{f} + i\Phi\psi_{k,p}) = f(1-2|\psi_{k,p}|^2) - f^*\psi_{k,p}^2 + \psi_{k,p} - \psi_{k,p}|\psi_{k,p}|^2 \\ +\nabla^2 f + \nabla^2\psi_{k,p} - 2i\mathbf{a}\cdot\nabla f - 2i\mathbf{a}\cdot\nabla\psi_{k,p} - a^2 f - a^2\psi_{k,p}$$

Knowing that $\psi_{k,p}$ is a solution of the stationary equations, it simplifies into

$$u(\dot{f} + i\Phi\psi_{k,p}) = f(1-2|\psi_{k,p}|^2) - f^*\psi_{k,p}^2 + \nabla^2 f - 2i\mathbf{a}\cdot\nabla.f - a^2 f. \tag{3.34}$$

Using the stationary solution found for 2D (3.32), we have:

$$u(\dot{f}+i\Phi\psi_{k,p}) = f[-1+2(k\mathbf{e_x}+p\mathbf{e_y}-\mathbf{a})^2-a^2]+f^*[-1+(k\mathbf{e_x}+p\mathbf{e_y}-\mathbf{a})^2]e^{2i(kx+py+\theta_0)}+\nabla^2 f-2i\mathbf{a}\cdot\nabla f$$

We use the substitution

$$f = \tilde{f}e^{i(kx+py+\theta_0)} \tag{3.35}$$

and obtain

$$u(\dot{\tilde{f}} + i\Phi|\psi_{k,p}|) = \tilde{f}[-1+2(k\mathbf{e_x}+p\mathbf{e_y}-\mathbf{a})^2 - a^2] + \tilde{f}^*[-1+(k\mathbf{e_x}+p\mathbf{e_y}-\mathbf{a})^2] \\ +\nabla^2\tilde{f} - (k^2+p^2)\tilde{f} + 2ik\frac{d\tilde{f}}{dx} + 2ip\frac{d\tilde{f}}{dy} + 2a_x k\tilde{f} + 2a_y p\tilde{f} - 2i\mathbf{a}\cdot\nabla\tilde{f},$$

which simplifies into

$$u(\dot{\tilde{f}} + i\Phi|\psi_{k,p}|) = \tilde{f}[-1+(k\mathbf{e_x}+p\mathbf{e_y}-\mathbf{a})^2] + \tilde{f}^*[-1+(k\mathbf{e_x}+p\mathbf{e_y}-\mathbf{a})^2] \\ +\nabla^2\tilde{f} + 2i(k\mathbf{e_x}+p\mathbf{e_y}-\mathbf{a})\cdot\nabla\tilde{f}.$$

Last, we write the first linearized equation:

$$u(\dot{\tilde{f}} + i\Phi|\psi_{k,p}|) = 2\Re(\tilde{f})[-1+(k\mathbf{e_x}+p\mathbf{e_y}-\mathbf{a})^2] + \nabla^2\tilde{f} + 2i(k\mathbf{e_x}+p\mathbf{e_y}-\mathbf{a})\cdot\nabla\tilde{f}, \tag{3.36}$$

with $\Re(z)$ and $\Im(z)$ denoting the real and imaginary part of a complex number z. After neglecting the terms of order higher than two in f, the second TDGL equation (3.4) reads

$$\kappa(\mathbf{j}-\mathbf{j}_{k,p}) = \frac{i}{2}(\psi_{k,p}^*\nabla f + f^*\nabla\psi_{k,p} - \psi_{k,p}\nabla f^* - f\nabla\psi_{k,p}^*) - \mathbf{a}(\psi_{k,p}^* f + \psi_{k,p}f^*) - (\dot{\mathbf{a}} - \nabla\Phi),$$

knowing that the stationary supercurrent is

$$\mathbf{j}_{k,p} = -\frac{i}{2}(\psi_{k,p}^*\nabla\psi_{k,p} - \psi_{k,p}\nabla\psi_{k,p}^*) - \mathbf{a}|\psi_{k,p}|^2. \tag{3.37}$$

We use the substitution described in Eq. (3.35)

$$\kappa(\mathbf{j}-\mathbf{j}_{k,p}) = 2\Re(\tilde{f})|\psi_{k,p}|(k\mathbf{e_x}+p\mathbf{e_y}-\mathbf{a}) + \Im(\nabla\tilde{f})|\psi_{k,p}| - (\dot{\mathbf{a}}-\nabla\Phi) \tag{3.38}$$

and obtain the linearized TDGL equations for the 2D case when $|\psi_{k,p}| = \sqrt{1-(k\mathbf{e_x}+p\mathbf{e_y}-\mathbf{a})^2}$:

$$u(\dot{\tilde{f}} + i\Phi|\psi_{k,p}|) = 2\Re(\tilde{f})[-1+(k\mathbf{e_x}+p\mathbf{e_y}-\mathbf{a})^2] + \nabla^2\tilde{f} + 2i(k\mathbf{e_x}+p\mathbf{e_y}-\mathbf{a})\cdot\nabla\tilde{f} \tag{3.39}$$

$$\kappa(\mathbf{j}-\mathbf{j}_{k,p}) = 2\Re(\tilde{f})|\psi_{k,p}|(k\mathbf{e_x}+p\mathbf{e_y}-\mathbf{a}) + \Im(\nabla\tilde{f})|\psi_{k,p} - (\dot{\mathbf{a}}-\nabla\Phi)|. \tag{3.40}$$

For the more general solution

$$\psi_{\nabla\theta} = \sqrt{1-(\nabla\theta-\mathbf{a})^2}e^{i\theta},$$

we have:

$$u(\dot{\tilde{f}} + i\Phi|\psi_{\nabla\theta}|) = 2\Re(\tilde{f})[-1+(\nabla\theta-\mathbf{a})^2] + \nabla^2\tilde{f} + 2i(\nabla\theta-\mathbf{a})\cdot\nabla\tilde{f} \tag{3.41}$$

$$\kappa(\mathbf{j}-\mathbf{j}_{\nabla\theta}) = 2\Re(\tilde{f})|\psi_{\nabla\theta}|(\nabla\theta-\mathbf{a}) + \Im(\nabla\tilde{f})|\psi_{\nabla\theta} - (\dot{\mathbf{a}}-\nabla\Phi)|. \tag{3.42}$$

3.3.2 Stability analysis

3.3.2.1 The general 2D case

We study the linearized equations in the case of homogeneous coefficients (see appendix C for a derivation including the coefficients) and we neglect the corrections to the magnetic vector potential. These simplifications will be important for the geometries we are interested in (see section 4.2 (1D) and section 5.1 (2D) for an explanation of this choice). The stationary solution has the form (3.32).

Let us separate the real and imaginary parts of the equations (3.39) and (3.40) using the notation $f_\mathbf{r} = \Re(\tilde{f})$ and $f_\mathbf{i} = \Im(\tilde{f})$. We apply once again the electroneutrality condition to the second equation and obtain

$$u\dot{f}_\mathbf{r} = 2[(k\mathbf{e_x}+p\mathbf{e_y}-\mathbf{a})^2-1]f_\mathbf{r} + \nabla^2 f_\mathbf{r} + 2(\mathbf{a}-k\mathbf{e_x}-p\mathbf{e_y})\cdot\nabla f_\mathbf{i} \tag{3.43}$$

$$u(\dot{f}_\mathbf{i} + \Phi|\psi_{k,p}|) = \nabla^2 f_\mathbf{i} + 2(k\mathbf{e_x}+p\mathbf{e_y}-\mathbf{a})\cdot\nabla f_\mathbf{r} \tag{3.44}$$

$$\nabla^2\Phi = 2|\psi_{k,p}|(k\mathbf{e_x}+p\mathbf{e_y}-\mathbf{a})\cdot\nabla f_\mathbf{r} + |\psi_{k,p}|\nabla^2 f_\mathbf{i}. \tag{3.45}$$

We perform Fourier transforms using the notation $\int_{-\infty}^{\infty}\int_{-\infty}^{\infty}\tilde{f}(x,y,t)e^{-i(xq+yr)}dxdy = \hat{f}(q,r,t) = \hat{f}_{\mathbf{r}}(q,r,t) + i\hat{f}_{\mathbf{i}}(q,r,t)$. For $q = r = 0$, we have

$$u\dot{\hat{f}}_{\mathbf{r}} = -2[1 - (k\mathbf{e_x} + p\mathbf{e_y} - \mathbf{a})^2\hat{f}_{\mathbf{r}}]$$
$$u(\dot{\hat{f}}_{\mathbf{i}} + \hat{\Phi}|\psi_{k,p}|) = 0$$

and thus

$$\hat{f}_{\mathbf{r}}(t) = e^{-2[1-(k\mathbf{e_x}+p\mathbf{e_y}-\mathbf{a})^2 t/u]} \tag{3.46}$$
$$\dot{\hat{f}}_{\mathbf{i}} = \frac{1}{u}\hat{\Phi}|\psi_{k,p}|. \tag{3.47}$$

As the growth rate in Eq. (3.46) is negative (see Eq. (3.19)), no instability will come from this term. The equation (3.47) resembles the Josephson equation [24] and implies that no instability will be developed from this term unless an external electrostatic potential is applied (for example, a voltage can be applied and implemented through the boundary conditions).

For $r \neq 0$ or $q \neq 0$ and $u \neq 0$, the system of equations becomes:

$$u\dot{\hat{f}}_{\mathbf{r}} = -2[1 - (k\mathbf{e_x} + p\mathbf{e_y} - \mathbf{a})^2]\hat{f}_{\mathbf{r}} - (q^2+r^2)\hat{f}_{\mathbf{r}} + 2i[q(a_x - k) + r(a_y - p)]\hat{f}_{\mathbf{i}}$$
$$u(\dot{\hat{f}}_{\mathbf{i}} + \hat{\Phi}|\psi_{k,p}|) = -(q^2+r^2)\hat{f}_{\mathbf{i}} + 2i[q(k - a_x) + r(p - a_y)]\hat{f}_{\mathbf{r}}$$
$$\hat{\Phi} = \frac{-2i}{q^2+r^2}|\psi_{k,p}|[q(k - a_x) + r(p - a_y)]\hat{f}_{\mathbf{r}} + |\psi_{k,p}|\hat{f}_{\mathbf{i}}.$$

Eliminating Φ from the equations, we have the linear system of equations:

$$\begin{pmatrix} u\dot{\hat{f}}_{\mathbf{r}} \\ u\dot{\hat{f}}_{\mathbf{i}} \end{pmatrix} = \begin{pmatrix} -2(1-(k\mathbf{e_x}+p\mathbf{e_y}-\mathbf{a})^2) - q^2 - r^2 & 2i[q(a_x-k)+r(a_y-p)] \\ 2i[q(k-a_x)+r(p-a_y)]\left(1+|\psi_{k,p}|^2\frac{u}{q^2+r^2}\right) & -(q^2+r^2) - u|\psi_{k,p}|^2 \end{pmatrix}\begin{pmatrix} \hat{f}_{\mathbf{r}} \\ \hat{f}_{\mathbf{i}} \end{pmatrix},$$

and this system is the most general eigenvalue problem corresponding to our case.

We use $\tilde{a}_x = a_x - k$ and $\tilde{a}_y = a_y - p$ (which are the components of the gauge invariant potential) and $|\psi_{k,p}|^2 = 1 - \tilde{a}_x^2 - \tilde{a}_y^2$. We can write the two eigenvalues of this dynamical system:

$$\lambda_1 = -\frac{1}{2u}\left[2(q^2+r^2) + |\psi_{k,p}|^2(u+2)\right]$$
$$+\frac{1}{2u(q^2+r^2)}\sqrt{(q^2+r^2)\left[(q^2+r^2)(u-2)^2|\psi_{k,p}^4| + 16(\tilde{a}_x q + \tilde{a}_y r)^2(q^2+r^2+u|\psi_{k,p}^2|)\right]}$$

$$\lambda_2 = -\frac{1}{2u}\left[2(q^2+r^2) + |\psi_{k,p}|^2(u+2)\right]$$
$$-\frac{1}{2u(q^2+r^2)}\sqrt{(q^2+r^2)\left[(q^2+r^2)(u-2)^2|\psi_{k,p}^4| + 16(\tilde{a}_x q + \tilde{a}_y r)^2(q^2+r^2+u|\psi_{k,p}^2|)\right]}$$

Those eigenvalues represent the Lyapunov exponents of the stationary solutions. We can immediately see that only λ_1 may be positive and therefore lead to instability.

Let us first isolate the first term in the root:

$$\tilde{\lambda}_1 = -\frac{1}{2u}\left[2(q^2+r^2)+|\psi_{k,p}|^2(u+2)\right]+\frac{1}{2u}\sqrt{(u-2)^2|\psi_{k,p}^4|}$$

if$(u \leq 2)$

$$\tilde{\lambda}_1 = -\frac{1}{u}(q^2+r^2+u|\psi_{k,p}|^2)$$

if$(u \geq 2)$

$$\tilde{\lambda}_1 = -\frac{1}{u}(q^2+r^2+2|\psi_{k,p}|^2).$$

Therefore, the second term

$$16(\tilde{a}_x q+\tilde{a}_y r)^2(u|\psi_{k,p}^2|+(q^2+r^2)) \tag{3.48}$$

is crucial for the development of the instability.

It contains as well the evolution of the 2D geometry of the instability regarding $\tilde{a}_x$ and $\tilde{a}_y$. Indeed, the only term in λ_1 that differentiates between q and r is

$$M = \frac{(\tilde{a}_x q+\tilde{a}_y r)^2}{q^2+r^2}.$$

Let us analyze the behavior of this term regarding r:

$$\frac{\partial M}{\partial r} = \frac{2\tilde{a}_y(\tilde{a}_x q+\tilde{a}_y r)}{r^2+q^2}-\frac{2r(\tilde{a}_x q+\tilde{a}_y r)^2}{(r^2+q^2)^2}$$

$$\frac{\partial M}{\partial r} = \frac{2}{(r^2+q^2)^2}\left[-\tilde{a}_x\tilde{a}_y q r^2+rq^2\left(\tilde{a}_y^2-\tilde{a}_x^2\right)+\tilde{a}_x\tilde{a}_y q^3\right],$$

which roots and sign can be easily studied. When $q \geq 0$ and $r \geq 0$ (we can extend to the other cases by symmetry), we find that

$$\frac{\partial M}{\partial r} \geq 0$$

if and only if

$$r \leq \frac{\tilde{a}_y}{\tilde{a}_x} q. \tag{3.49}$$

The inequality above tells us that the highest Lyapunov exponent will be found for wavenumbers satisfying:

$$\tilde{a}_x r = \tilde{a}_y q. \tag{3.50}$$

This equation gives the symmetry of the instability that will dominate the dynamics.

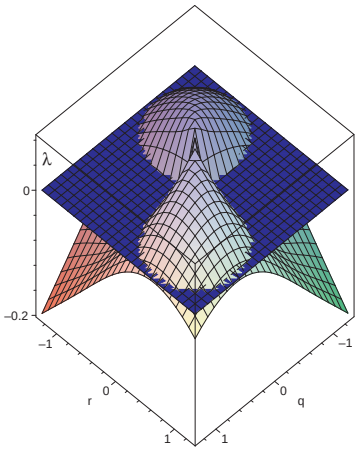

FIGURE 3.4: Eigenvalue λ_1 for the 2D case depending on q and r, with $\tilde{a}_x = \tilde{a}_y = 0.6$ and $u = 20$. The fastest growing mode is symmetric in both directions.

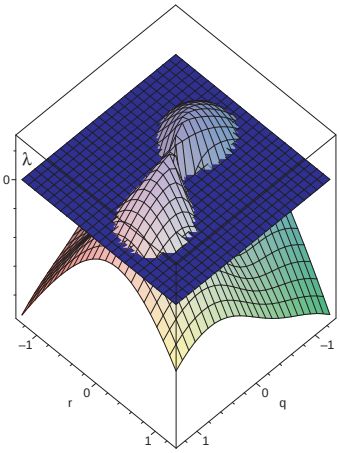

FIGURE 3.5: Eigenvalue λ_1 for the 2D case depending on q and r, with $\tilde{a}_x = 0.7$, $\tilde{a}_y = 0.3$ and $u = 20$. The fastest growing mode satisfies $r = 0.43q$.

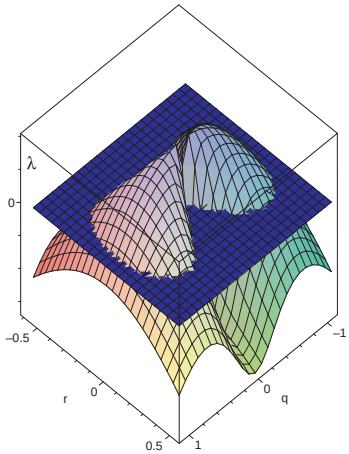

FIGURE 3.6: Eigenvalue λ_1 for the 2D case depending on q and r, with $\tilde{a}_x = 0.7$, $\tilde{a}_y = 0$ and $u = 20$. The instability is purely one dimensional.

We can intuitively interpret this result: when $\tilde{a}_x = \tilde{a}_y$, the situation is symmetric regarding q and r as seen in Fig. 3.4. However, as if we start to decrease $\tilde{a}_y$, the fastest growth rate is now found for $q > r$ (Fig. 3.5). As $\tilde{a}_y$ decreases, the q component of the instability will therefore decrease until the limit case $\tilde{a}_y = 0$. When $\tilde{a}_y = 0$, the instability with the fastest growth will be for $r = 0$ (Fig. 3.6). The instability is purely one dimensional: the other component stabilizes the initial stationary solution.

In practice we can always make a change of coordinates so that $\tilde{a}_y = 0$. The condition (3.50) thus means that *according to the linear stability analysis, the instability will always develop in a 1D fashion.* We can thus reduce the problem to the 1D case.

3.3.2.2 Stability in 1D and the Eckhaus bands

In 1D, we have the linearized system of equations:

$$\begin{pmatrix} \dot{\hat{f}}_{\mathbf{r}} \\ \dot{\hat{f}}_{\mathbf{i}} \end{pmatrix} = \tfrac{1}{u} \begin{pmatrix} -2(1-(k-a_x)^2) - q^2 & 2iq(a_x - k) \\ 2iq(k-a_x)\left(1 + |\psi_k|^2 \frac{u}{q^2}\right) & -q^2 - u|\psi_k|^2 \end{pmatrix} \begin{pmatrix} \hat{f}_{\mathbf{r}} \\ \hat{f}_{\mathbf{i}} \end{pmatrix}. \tag{3.51}$$

We use again the notation $\tilde{a}_x = a_x - k$. In 1D we also have $a_x = a$

The characteristic polynomial is:

$$\chi(\lambda) = \frac{1}{u^2}\left\{\lambda^2 u^2 + \lambda u\left[2q^2 + |\psi_k|^2(2+u)\right] + |\psi_k|^2\left[(2+u)q^2 + 2u(|\psi_k|^2) - 4\,u\tilde{a}_x^2\right] - 4\tilde{a}_x^2 q^2 + q^4\right\}. \tag{3.52}$$

The only eigenvalue that may be positive is:

$$\lambda_1 = -\frac{1}{2u}\left[2q^2 + |\psi_k|^2(u+2)\right] + \frac{1}{2u}\sqrt{(u-2)^2|\psi_k^4| + 16\tilde{a}_x^2(q^2 + u|\psi_k^2|)}. \tag{3.53}$$

It is easy to see that λ_1 is even regarding q and goes to $-\infty$ as $|q|$ goes to ∞.

As both eigenvalues are negative for $|q|$ large enough (they behave in $-q^2 + O(|\tilde{a}_x|)$, to have an instability, we need to see when we can have the solution $\lambda = 0$ in the equation (3.52). This can happen only if

$$|\psi_k|^2\left[(2+u)q^2 + 2u(|\psi_k|^2) - 4\,u\tilde{a}_x^2\right] - 4\tilde{a}_x^2q^2 + q^4 = 0.$$

This equation is a bi-quadratic equation in q^2 and therefore $\lambda = 0$ can be a solution of Eq. (3.52) if

$$q^2 = 4\tilde{a}_x^2 - 2|\psi_k^2|.$$

With $|\psi_k| = \sqrt{1-\tilde{a}_x^2}$ we have the solution,

$$q = \pm\sqrt{2}\sqrt{3\tilde{a}_x^2 - 1},$$

under the condition that

$$\tilde{a}_x \geq \frac{1}{\sqrt{3}}. \tag{3.54}$$

This solution corresponds to $\lambda_1 = 0$. To understand the behavior, we study

$$\frac{\partial\lambda_1}{\partial q} = -\frac{2q}{u} + \frac{8\tilde{a}_x^2 q}{u\sqrt{((u-2)^2|\psi_k^4| + 16\tilde{a}_x^2(q^2 + u|\psi_k^2|)}}. \tag{3.55}$$

The derivative has a maximum of three roots (including $q = 0$) and we thus know the variation of the eigenvalue regarding q, as plotted in figure 3.7 (knowing the number of roots and the limits, we can deduce the sign of $\frac{\partial\lambda_1}{\partial q}$). As a result, the instability in 1D (and in 2D with $a_y = p = 0$) develops under the conditions:

$$\begin{cases} |a_x - k| & > & \frac{1}{\sqrt{3}} \\ |q| & < & \sqrt{2}\sqrt{3(a_x-k)^2 - 1}. \end{cases} \tag{3.56}$$

$|a_x - k| > \frac{1}{\sqrt{3}}$ is the condition of the existence of modes satisfying $|q| < \sqrt{2}\sqrt{3(a_x-k)^2-1}$, which are the only possible unstable modes. Therefore, we obtain a simple sufficient stability condition:

$$|a_x - k| < \frac{1}{\sqrt{3}}. \tag{3.57}$$

This condition indicates as well which branch of the superconducting current plotted in Fig. 3.2 is stable.

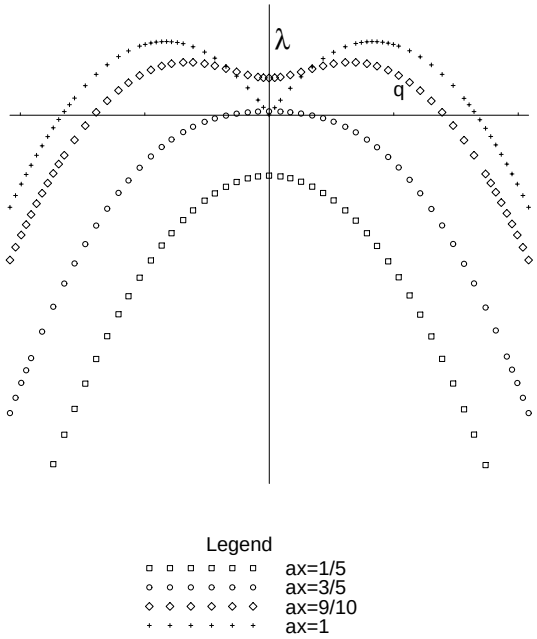

FIGURE 3.7: Sketch of λ_1 as a function of q for different values of a_x and $u = 0.5$.

For $|a_x - k| > \frac{1}{\sqrt{3}}$, the stability condition reads:

$$|q| > \sqrt{2}\sqrt{3(a_x - k)^2 - 1}. \tag{3.58}$$

The plot of λ_1 in figure 3.8 and 3.7 confirms our analysis. In 2D, when $a_y = 0$, with $\psi_k =$

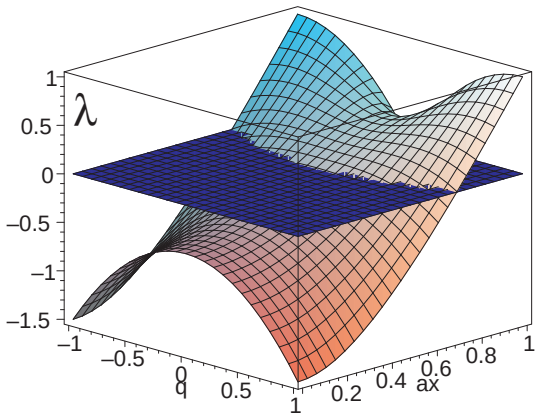

FIGURE 3.8: Eigenvalue λ_1 as a function of a_x and q at $u = 0.5$.

$\sqrt{1 - (a_x - k)^2 - p^2}e^{i(kx+py)+\theta_0}$, the stability condition is:

$$\begin{cases} 3(a_x - k)^2 + p^2 & < & 1 \\ \quad \text{or} & & \\ \quad |q| & > & \sqrt{2}\sqrt{3(a_x - k)^2 + p^2 - 1}. \end{cases} \tag{3.59}$$

It is most remarkable that the stability condition does not depend on the value of u (we excluded the case $u = 0$). However, we will see in section 4.3.3 that u does play a role in the development of the instability. The influence of u can be observed in Fig. 3.9 as well.

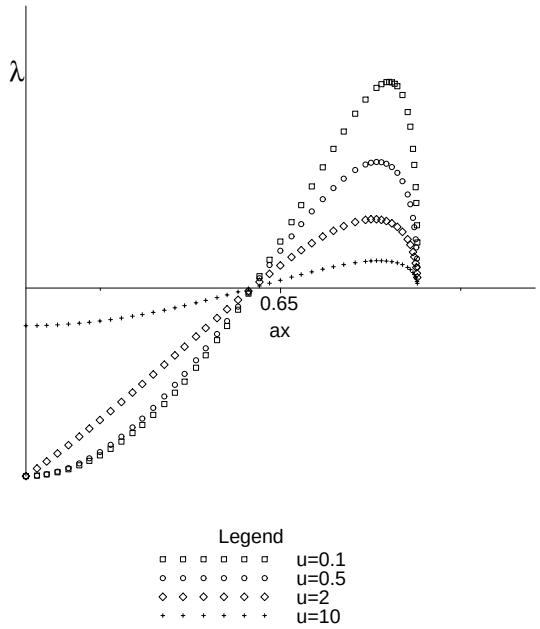

FIGURE 3.9: Eigenvalue λ_1 as a function of a_x for $q = 0$ and different values of u. We see that u does not play a role in the stability condition, but does have an influence on the growth rate.

The Eckhaus bands: Such a type of instability, which depends on the wave vector of the stationary solution, is often referred to as the Eckhaus instability. As we said in section 3.2.1, the time-dependent Ginzburg-Landau equation is sometimes studied in a more general context and referred to as the CGL equation. In our case we limit the analysis to the real coefficient α_r:

$$u\left(\frac{\partial\psi}{\partial t} + i\Phi\psi\right) = -\alpha_r\psi - \psi|\psi|^2 - (i\nabla + a_x)^2\psi$$

and, as derived in appendix C, the stationary solution assuming that α_r is constant is:

$$\psi_k = \sqrt{-\alpha_r - \tilde{a}_x^2}e^{ikx+\theta_0}.$$

Following the common mathematical analysis of the CGL equations we use α_r as the main parameter instead of the external magnetic vector potential $\mathbf{a}$.

The stability diagram can be written in the form:

$$\begin{cases} -\alpha_r & \geq & (k-a_x)^2 & \text{the stationary solutions exist} \\ -\alpha_r & \leq & 3(k-a_x)^2 & \text{the stationary solution is Eckhaus unstable} \\ -\alpha_r & < & 3(k-a_x)^2 - q^2 & \text{perturbations with wavenumber } q \text{ are unstable} \end{cases} \tag{3.60}$$

This is the common way to study the Eckhaus instability and the result is summarized in Fig. 3.10.

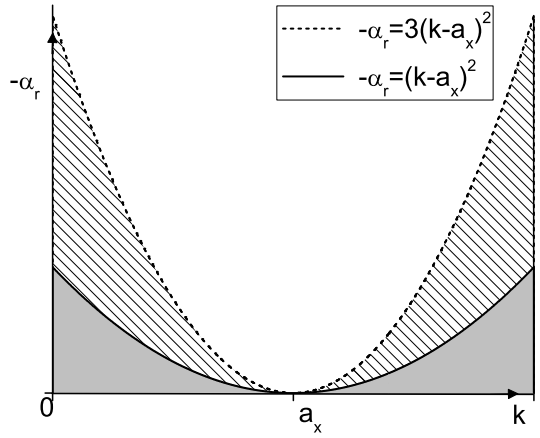

FIGURE 3.10: Representation of the Eckhaus instability as it is generally studied in the CGL framework. For$-\alpha_r \geq (k-a_x)^2$ (above the plain curve), the stationary solution of the form $\psi_k\sqrt{-\alpha_r-\tilde{a}_x^2}e^{ikx+\theta_0}$ exists. For $-\alpha_r \geq 3(k-a_x)^2$ (above the dashed curve), the solution is linearly stable. Between the Eckhaus bands: $(k-a_x)^2 \leq -\alpha_r \leq 3(k-a_x)^2$ (the dashed area), the solution of the form $\psi_k\sqrt{-\alpha_r-\tilde{a}_x^2}e^{ikx+\theta_0}$ exists and is unstable: this is the region where the instability forms. In the white region, the stationaty solution is stable. The instability depends on the wavenumber of the initial stationary solution.

Remark on the equation without potential: In the CGL equations and in other versions of the TDGL equation, the electrostatic potential is absent from the equations, as well as the equation for current. The stability analysis is simplified and leads to the same conditions with the addition of another case of stability for q=0 as we can see from the form of the only positive eigenvalue plotted in Fig. 3.11.

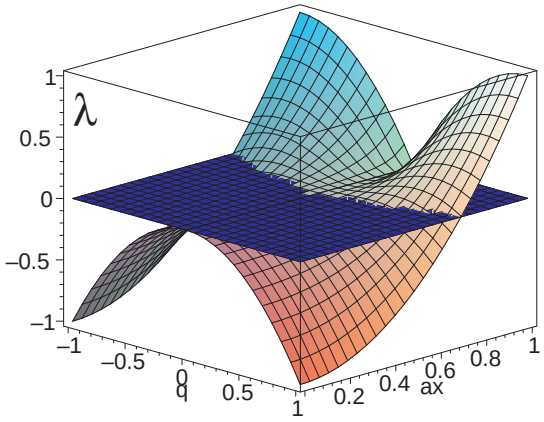

FIGURE 3.11: Eigenvalue λ_1 as a function of a_x and q for $\Phi = 0$

3.4 Conclusions of this chapter

We have formulated the dimensionless TDGL equations and included variables for the inhomogeneity:

$$\gamma_r u\left(\frac{\partial\psi}{\partial t}+i\Phi\psi\right)=-\alpha_r\psi-\beta_r\psi|\psi|^2-(i\nabla+\mathbf{a})^2\psi$$

$$\nabla\times(\nabla\times\mathbf{a})=\frac{1}{\kappa_0^2}\left[-\frac{i}{2}(\psi^*\nabla\psi-\psi\nabla\psi^*)-\mathbf{a}|\psi|^2-\sigma_r\left(\frac{\partial\mathbf{a}}{\partial t}+\nabla\Phi\right)\right].$$

Using nonhomogeneous coefficients in the TDGL equations appears like a simple tool to model complex experimental situations: impurities, assembly of different materials, time-dependence of the properties etc. However, these equations have a limited range of validity. As we saw in section 2.1, the GL equations and their coefficients are derived for the equilibrium case and close to the critical temperature T_c. The TDGL equations are generally considered to bring very good qualitative results even for a wider range of situations, but the quantitative predictions should be takled with caution.

We extended the study of stationary solutions to the case with magnetic vector potential and in 2D we found the solutions satisfying $\nabla^2\rho=0$:

$$\psi_{k,p}=\sqrt{1-(k\mathbf{e_x}+p\mathbf{e_y}-\mathbf{a})^2}e^{i(kx+py+\theta_0)}.$$

In the most frequently used boundary conditions these solutions have a uniform amplitude. Those solutions agree with those found in the literature for the CGL equations. The conditions of existence of such solutions are important as well.

We also have found a very interesting way of describing the 2D instabilities. Indeed we found that the Fourier wavenumbers (q,r) of the dominant growing mode satisfy the condition:

$$\tilde{a}_x r=\tilde{a}_y q.$$

This condition means that the instability will always develop in a 1D fashion.

The stability condition for the stationary solutions for $a_y=0$ yields

$$\begin{cases} 3(a_x-k)^2+p^2 & < & 1 \\ \quad \text{or} & & \\ |q| & > & \sqrt{2}\sqrt{3(a_x-k)^2+p^2-1}, \end{cases}$$

which is rich in content. It joins the analysis in terms of Eckhaus bands with the thermodynamical analysis of the stability of the branches of $j_s(\rho)$.

Chapter 4

Dynamics in 1D: The phase slip phenomenon

In this chapter, we investigate fluctuations of the superconducting state that lead to the appearance of resistivity in 1D superconductors. Most of the results of this chapter have been published in [40] and [41].

4.1 1D superconductors and phase slip theories

4.1.1 1D geometries

Low dimensional systems are interesting to study as they represent the limit of miniaturization for experiments and applications. Moreover, the recent trend towards nanosciences and nanotechnologies has lead scientists of all fields to investigate the new effects that appear when the size is reduced. The new measurement tools like the scanning tunneling microscope (STM), the atomic force microscope (AFM), photoemission based analysis etc. along with new techniques for the production of small geometries, can now be compared with older theories or need new theories to be compared with.

Low dimensional systems have always been of interest from the theoretical point of view because they sometimes exhibit new phenomena when some critical size is reached but as well because they can be more simple to study since the equations are reduced.

In superconductors, in the framework of the Ginzburg-Landau (GL) theory, the coherence length ξ is the characteristic value of the smallest distance over which fluctuations of the order parameter

can take place (see section 2.1.4 or [1]). Therefore, wires of width $d \ll \xi$ are considered one-dimensional.

4.1.2 The phase slip theory

Nonequilibrium phenomena in superconductors can bring up very intriguing problems. For instance, a resistive state can be observed without a complete destruction of the superconducting state by temperature, magnetic field or current. Such a situation can be at first confusing because the first hallmark of superconductivity is violated but it becomes clearer once one studies the responsible fluctuations in details.

The first idea that thermodynamical fluctuations can cause the decay of the current in a 1D superconductor was given by W. A. Little [42]. At the time, it was not clear whether or not the superconducting state was even possible in the limit of 1D and 2D samples [43, 44]. The idea which emerged and which is generally accepted is that in 1D geometries, there is no sharp transition: the resistivity drops smoothly with temperature, as thermal fluctuations decay. The critical temperature T_c in such samples is defined by the mean-field transition temperature. W. A. Little was soon followed by J. S. Langer and V. Ambegaokar [45] who derived a model to evaluate quantitatively the resistance in order to explain the experimental data that started to rise at that time [46, 47]. That model was later corrected by D. E. McCumber and N. B. Halperin [48]. It is now common to refer to the theory by the abbreviation of the name of all four authors: the LAMH theory.

4.1.2.1 The main ideas of the LAMH theory.

J. S. Langer and V. Ambegaokar [45] followed the experimental evidence that resistance and therefore voltage appeared in a superconducting wire with a current close to its critical current j_c [46, 47]. They claimed that the observed resistivity was due to fluctuations whose free energies are much higher than the thermal energy. Their idea was that if a voltage V appears between two points of a superconductor, according to the Josephson equation $\frac{\partial}{\partial t}(\Delta\theta) = V$ (see section 2.3.2 and [24]), the difference in the phase of the order parameter between these points will increase linearly with time. When looking at the expression of the superconducting current $\mathbf{j_s} = \rho^2(\nabla\theta - \mathbf{a})$, this would mean that the current would be constantly increasing, even over the critical value $j_c = 2/\sqrt{27}$ (see Eq. (3.15), which is impossible. However, such a situation is possible if fluctuations in the superconductor reduce the phase difference at the same rate as the voltage increases it.

To summarize, applying a sufficiently strong current to a superconducting wire can place it into a resistive state where superconductivity is not completely lost but where fluctuations allow the presence of a voltage within the wire.

To study the fluctuations responsible for this effect, J. S. Langer and V. Ambegaokar assumed that the 1D samples were indeed described by a complex order parameter: they based their theory on the 1D (stationary) GL equations. Their main assumption was that any stationary solution of the GL equations corresponding to a non-zero current was only metastable: a state of lower current and lower free energy is accessible at the cost of an energy barrier. The energy to overcome this barrier would come from thermal fluctuations: as the fluctuation rate decreases with temperature, at $T = 0$ the current should be purely superconducting (as proposed by W. A. Little [42]). To find the height of this energy barrier, one needs to find the solution of the GL equations corresponding to the saddle point of the free energy landscape.

4.1.2.2 Calculation of the saddle solution

We here revisit the calculation of the saddle state done by J. S. Langer and V. Ambegaokar. We use the formulation of section 3.2.2 in the homogeneous case. The stationary GL equations read:

$$\nabla^2\rho = -\frac{\partial U(\rho)}{\partial \rho} \tag{4.1}$$

with

$$U = \frac{1}{2}\left(\frac{j_s^2}{\rho^2} + \rho^2 - \frac{1}{2}\rho^4\right), \tag{4.2}$$

and

$$\mathbf{j_s} = \rho^2(\nabla\theta - \mathbf{a}). \tag{4.3}$$

We remind that ρ is the amplitude and θ is the phase of the complex order parameter $\psi = \rho e^{i\theta}$. The order parameter is a function of the position coordinate x and of the time t. The superconducting current is $\mathbf{j_s}$, $\mathbf{a}$ is the magnetic vector potential and U plays the role of a potential in the mechanical analogy of section 3.2.2. In the mechanical analogy, ρ plays the role of the position of a particle moving in the potential U and x plays the role of the time. Along with the mechanical analogy, we can write the equation for the conservation of the energy, which is the first integral of the GL equation:

$$\frac{\partial}{\partial x}\left[\frac{1}{2}\left(\frac{\partial \rho}{\partial x}\right)^2 + U\right] = 0 \tag{4.4}$$

Nonuniform solutions of Eq. (4.1) that do not diverge are periodic solutions in x: the position ρ of the particle will oscillate with time according to the potential well as described in Fig. 3.1. The maximum of the potential $U_{\max}$ is reached for $\rho = \rho_0$ (the position of the maximum) and $\rho = \rho_1 < \rho_0$ (on the left branch).

We describe a solution that starts from ρ_0 (or inferior and arbitrarily close to ρ_0). This solution will oscillate between ρ_0 and ρ_1 (see Fig. 3.1). The starting solution ρ_0 is the value of the uniform stationary solution (see section 3.2.2) and ρ_1 is the other possible solution of the equation

$U(\rho) = U_{\max}$. Such a choice is made to construct a solution as close as possible from the starting uniform solution ρ_0.

We can integrate Eq. (4.4)

$$x = \int_{\rho_1}^{\rho_{\text{saddle}}} \frac{d\rho}{\sqrt{2(U_{\max} - U)}}$$

We chose to integrate from ρ_1 which means that we put the origin of the time x when the position of the particle is ρ_1. We assume that the behavior of the fluctuation will be symmetric for the times $x < 0$. We immediately see that the time x goes to ∞ when $\rho = \rho_0$: the particle is "stuck" on the plateau for a very long time, which is the appropriate limit case.

The calculation of the previous integral gives

$$x = \int_{\rho_1}^{\rho_{\text{saddle}}} \frac{2\rho d\rho}{\sqrt{2\left(\rho^6 - 2\rho^4 - 2j_s^2 + 4\rho^2 U_{\max}\right)}}.$$

We make a change of variable $P = \rho^2$ and we have

$$\sqrt{2}x = \int_{P_1}^{P_{\text{saddle}}} \frac{dP}{\sqrt{P^3 - 2P^2 + 4PU_{\max} - 2j_s^2}}. \tag{4.5}$$

We know that $U_{\max} = U(P_1) = U(P_0)$ and we have as well $\frac{\partial(U_{\max}-U)}{\partial P}_{P=P_0} = 0$. Therefore, the denominator of the right hand side of equation (4.5) can be factorized into $\sqrt{(P-P_0)^2(P-P_1)}$ and the identification of the coefficients yields:

$$2P_0 + P_1 = 2 \tag{4.6}$$

$$2P_0P_1 + P_0^2 = 4U_{\max} \tag{4.7}$$

$$P_0^2 P_1 = 2j_s^2. \tag{4.8}$$

Using the factorized expression and the variable $(P - P_0)$ we can integrate Eq.(4.5) and we obtain

$$\sqrt{2}x = \frac{2}{\sqrt{P_0 - P_1}} \text{arctanh}\left(\sqrt{\frac{P_{\text{saddle}} - P_1}{P_0 - P_1}}\right),$$

which, using the notation $\Delta = P_0 - P_1 = \rho_0^2 - \rho_1^2$ yields:

$$P_{\text{saddle}} = \rho_{\text{saddle}}^2 = \rho_0^2 - \Delta \text{sech}^2\left(x\sqrt{\frac{\Delta}{2}}\right). \tag{4.9}$$

This solution is plotted in Fig .4.1(a).

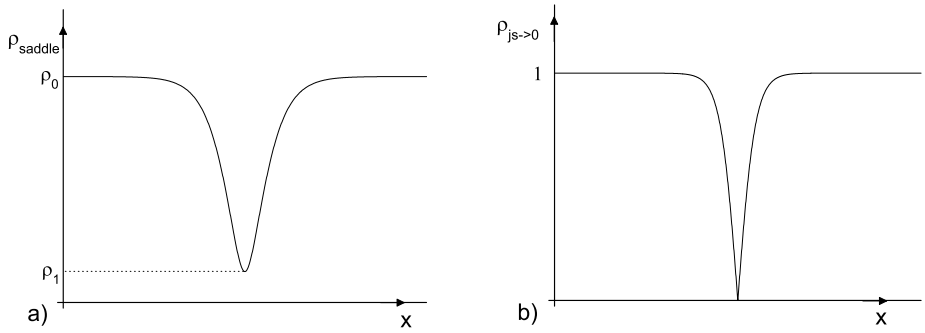

FIGURE 4.1: Solution ρ_{saddle} of the stationary GL equations corresponding to a saddle point of the free energy. For $j_s \to 0$, we have $\rho_1 \to 0$ and $\rho_0 \to 1$

For the case when $j_s \to 0$, the solution simply becomes:

$$\rho_{j_s \to 0} = \left| \tanh\left(\frac{x}{\sqrt{2}}\right) \right|, \tag{4.10}$$

and is plotted in Fig .4.1(b)

This solution, corresponding to a saddle point of the free energy, has a small region in which the amplitude of the order parameter is reduced. J. S. Langer and V. Ambegaokar assumed that from the solution of reduced order parameter ρ_{saddle} (4.9), the order parameter would continue to decrease and reach zero at a specific point: the phase slip center (like in the case of the solution $\rho_{j_s \to 0}$ (4.10)). At the phase slip center, the phase makes a 2π jump in order to satisfy the Josephson equation (2.40).

Physically, these solutions are intuitive: reducing the order parameter in a narrow region doesn't seem to be too costly regarding the free energy, yet it allows dissipation to happen. The mechanical analogy is very useful and helps as well to construct other non-uniform solutions: they will be solutions in which the order parameter will be reduced periodically (like for tanh but translated multiple times). Of course, the boundary conditions will restrain the possible solutions.

Last, as we noticed in section 3.2.2, the use of the potential U can be confusing because of the divergence with the limiting case $j_s = 0$. Moreover, as the order parameter is reduced in a narrow band, j_s which depends on ρ will be non-uniform as well.

4.1.2.3 Phase slip rate and other theories

From ρ_{saddle}, the corresponding free energy can be calculated. It leads to the rate at which phase slips will happen and to a prediction of the resistivity as a function of temperature. Indeed, the rate $\mathcal{P}$ at which phase slips occur at the temperature T is

$$\mathcal{P} = \Omega \exp\left(-\frac{\Delta F}{k_B T}\right), \tag{4.11}$$

where ΔF is the difference in free energies separating two neighboring metastable states and k_B the Boltzmann constant. The prefactor Ω was assumed from J. S. Langer and V. Ambegaogar to be obtainable from the relaxation time which appears in the conductivity of a normal metal. However, this lead to large disagreements with the experimental results.

This rate was later corrected by D. E. McCumber and N. B. Halperin [48] using the time-dependent Ginzburg-Landau equations [32, 48]. The correction of the prefactor leads to a difference about ten orders of magnitude which was coherent with most experiments. Due to the success of this correction, the theory is commonly referred to as the LAMH theory.

Many experimental works, have confirmed the resistivity of 1D samples by measuring the current-voltage characteristics of different superconductors. The main feature coming from most of the results is the presence of voltage steps: the resistivity increases by steps with increasing current. These voltage steps discovered by W. W. Webb and R. J. and Warburton [49] and can be linked to the effects of multiple phase slip centers. Many extensions of the LAMH theory have been derived in order to take into account different experimental results like the voltage steps and to add more details. T. J. Rieger, D. J. Scalapino and J. E. Mercereau [50] used the TDGL equations to describe the oscillations of the superconducting current at the Josephson frequency (see section 2.3). W. J. Skocpol, M. R. Beasley and M. Tinkham [51] added some aspects of the microscopic theory into the model by taking into account the quasiparticle excitations produced during the phase slip. They described the voltage steps with a system of individual phase slip centers. Overall the theories based on the LAMH derivations have been commonly accepted and are widely used. For a more complete review of theoretical and experimental works, see [1, 28, 52].

In superconducting rings, which is the configuration that will have most of our interest in this chapter, F. von Oppel and E. Riedel (VOR) [53] analyzed the currents induced by phase slip fluctuations. They were followed by X. Zhang and C. Price [54] who added susceptibility measurements by a SQUID (see section 2.3 for a simple description of a SQUID) and even more recently N. C. Koshnick *et. al.* [55] who attempted to fit the VOR theory with their experiments below and above the mean-field T_c.

The phase slip dynamics described above rely on the possibility to overcome the energy barrier between two distinct states. Close to T_c, such fluctuations are very important, but at lower temperatures, they should become negligible. Some experimental and theoretical works aim to prove the importance of another type of phase slip events: quantum phase slips. Indeed, for wires with very small cross section, N. Giordano [56, 57] observed a crossover from the thermally activated phase slips to the quantum phase slip regime as the temperature was reduced. However, the validity of the GL framework fades at low temperature and other theoretical developments were needed to describe and quantify what could be quantum tunneling between the metastable

states ([58]). At the present time, the observability and to a certain extent the description of quantum phase slips remains controversial.

Last, motivated by the analogy between quantum phase slips and Josephson tunnel junctions, a series of works studied the possibility of quantum bits (qubits) made from superconducting rings [59]. Indeed, rings containing Josephson junctions (see section 2.3 for a simple description of Josephson junctions) are largely studied as potential candidates for qubits [60]. By analogy, very thin nanowires exhibiting such quantum phase slip junctions might even have advantages over Josephson junctions [61]. As we see in Fig. 4.3, the free energy of the metastable states appear like a good starting point to build qubits. A recent review on 1D superconductors containing these modern questions can be found in [62].

In this chapter, we concentrate on thermally activated phase slips and we will develop a more detailed analysis of the phase slip transition without worrying about the statistical fluctuation rates.

4.2 Phase slips in a mesoscopic superconducting ring

4.2.1 Comparison with previous works

The LAMH theory described above gives a good global idea of fluctuations. However, it is still based on assumptions regarding the actual dynamics. Moreover a number of questions remain open: how do the supercurrent and the electrostatic potential behave ? What are the important parameters ? Does the geometry play a significant role ?

Recently, simulations were carried out on different versions of the TDGL equations in order to investigate the dynamics of the process. The case of the 1D ring can be particularly interesting for theoreticians because of the symmetry of the system and periodic boundary conditions. Moreover, experimental conditions such as contacts with the source of current or voltage as well as measuring devices do not need to be considered: one can assume a free standing ring placed in a solenoid producing a uniform magnetic field and a SQUID (see section 2.3) that measures the final state of the ring. Last as we will see in our analysis, single or a finite number of phase slip events can be described between distinct initial and final states [54], rather than observing an average rate.

In the work of M. B. Tarlie and K. R. Elder [63], the ring considered was in an external electromotive force which constantly accelerates the superconducting electrons. Another approach was used by D. Y. Vodolazov and F. M. Peeters [64], who increased the magnetic field gradually. The latter simulations were confirmed by the experiments made in [65] and [66].

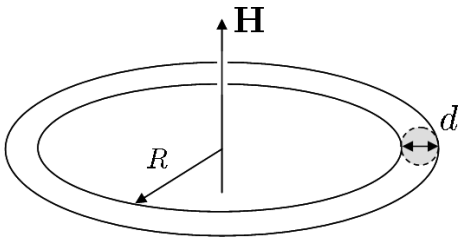

FIGURE 4.2: Geometry of the ring of radius R and thickness d with the magnetic field $\mathbf{H}$.

In the rest of this chapter, we consider a superconducting ring of thickness d, radius R and length L as represented in Fig. 4.2. We consider $d \ll \xi \ll \lambda_{\text{eff}}$, $R \gtrsim \xi$ and $R \ll \lambda_{\text{eff}}$, where ξ is the coherence length and λ_{eff} is the Pearl [18] penetration depth. The first two conditions allow us to treat the ring as one-dimensional and the last two conditions account for the mesoscopic size of the ring. We apply an external constant magnetic field $\mathbf{H}$, perpendicular to the 1D ring. The field $\mathbf{H}$ is an external parameter that controls the parameters (superfluid density, current etc.) of the ring.

Our approach is different from that of [63] and [64] because we investigate the stability of a stationary state and observe the relaxation process from the initial metastable state to a stable one, without any evolving external parameter influencing the dynamics. Indeed, starting from a solution of the stationary GL equations, we derived the stability condition regarding small time-dependent perturbations. For example starting from a stable state, an increase in the magnetic field can result in the superconducting state to evolve towards a new equilibrium. This new equilibrium is found via one or more phase slip processes. Moreover, using an instant increase in the magnetic field in contrast with the ramp applied in Ref. [64] allows us to investigate the competition between consecutive and simultaneous phase slips.

4.2.2 Adapting the analytical study

We study the phase slip process using the TDGL equations as derived in section 2.4. Here we consider a uniform mesoscopic ring. The dimensionless order parameter $\psi = \rho(x,t)e^{i\theta(x,t)}$ takes the value $\psi = 1$ in the equilibrium and in the absence of field. The space and time coordinates (x,t) are measured in units of the coherence length ξ and of the characteristic relaxation time of the phase $\tau_\theta = \frac{4\pi\lambda_{\text{eff}}^2\sigma_n}{c^2}$ (σ_n is the conductivity of the normal state and c is the speed of light). The Pearl penetration depth $\lambda_{\text{eff}} = \frac{\lambda_L^2}{d}$ has been used instead of the London penetration depth λ_L since the thickness d is small. The vector potential $\mathbf{a}$ is written in units of $\frac{\phi_0}{2\pi\xi}$ (ϕ_0 is the flux quantum) and the electrostatic potential Φ in units of $\frac{\hbar}{2e\tau_\theta}$, with e being the elementary charge and $\hbar$ as the reduced Planck constant.

The only dimensionless parameter left in the equation is the ratio $u = \frac{\tau_\rho}{\tau_\theta}$ between the two characteristic times: τ_ρ is the characteristic time of the evolution of the amplitude of the order parameter,

whereas τ_θ accounts for the dynamics of the phase (we will see a confirmation of this assertion in section 4.3.3).

We also add a Langevin noise η during the simulations. The intensity of the noise may vary considerably from one material to another and depends on the experimental conditions. Nevertheless, for the case of the second-order phase transition, the noise should be small and on the order of $\frac{k_B T}{d^2 H_{c_2}^2 \xi} \sim \frac{T}{T_c}(\frac{k_B T_c}{E_F})^2 \ll 1$ in dimensionless units when $d \lesssim \xi$. Here, k_B is the Boltzmann constant, T is the temperature, T_c is the critical temperature, H_{c_2} is the second critical field and E_F is the Fermi energy. The GL parameter $\kappa = \frac{\lambda_{\text{eff}}}{\xi}$ is large and the dimensions of the ring are small. Therefore, we neglect the corrections to the vector potential. Moreover, using the electroneutrality relation (3.5), Eq. (3.4) is again simplified. The two equations (3.3) and (3.4) yield:

$$u\left(\frac{\partial \psi}{\partial t} + i\Phi\psi\right) = \psi - \psi|\psi|^2 - (i\nabla + \mathbf{a})^2\psi + \eta \tag{4.12}$$

$$\nabla^2\Phi = -\nabla\left[\frac{i}{2}(\psi^*\nabla\psi - \psi\nabla\psi^*) + \mathbf{a}|\psi|^2\right]. \tag{4.13}$$

The uniform stationary solutions have been studied in section 3.2. For the present geometry, they are

$$\psi_k = \sqrt{1-(a-k)^2}e^{i(kx+\theta_0)}, \tag{4.14}$$

where k and θ_0 are real numbers. Periodic boundary conditions imply that $k = \frac{2n\pi}{l}$, where l is the dimensionless length of the wire and n is an integer that corresponds to the winding number or vorticity of the solution. Indeed, we have $n = \frac{1}{2\pi}\oint \frac{d\theta}{dx}$.

Let us now use the results of the stability analysis performed in section 3.3. For the case of periodic boundary conditions such as in the 1D ring, we use the Fourier expansion of the perturbation,

$$\hat{f}(q) = \sum_{m\in\mho} c_m(y)\delta\left(q - \frac{m}{l}\right), \tag{4.15}$$

where $c_m(f), m \in \mathbb{Z}$ are the Fourier coefficients of f and δ is the Dirac delta function. Therefore, the stability condition (3.58) transforms into

$$|k-a| \leq \frac{1}{\sqrt{3}}\sqrt{1+\frac{m^2}{2l^2}} \tag{4.16}$$

and is in agreement with those found in previous works [63, 64]. Let us rewrite this condition in the form,

$$m^2 \geq l^2\left[6(k-a)^2 - 2\right]. \tag{4.17}$$

It means that the higher modes corresponding to multiple simultaneous phase slips will be stable if the length of the wire is small enough. In other words, the length of the wire can restrict the

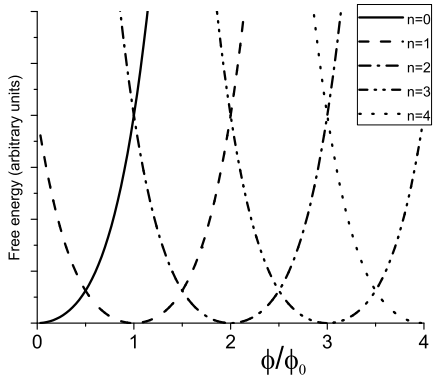

FIGURE 4.3: Shape of the free energy of the ring for the uniform stationary solutions ψ_n depending on the ratio $\frac{\phi}{\phi_0}$ and the winding number n.

number of phase slips that can happen at the same time. Moreover, the size of the ring plays an important role in the selection between multiple and consecutive processes as we discuss in section 4.3.3. Depending on the size of the ring, different modes can have highest eigenvalue.

We simplify the stability condition into:

$$|k - a| \leq \frac{1}{\sqrt{3}}. \tag{4.18}$$

This condition may be viewed as a generalization of Eq. (4.16). It corresponds to the thermodynamically stable supercurrent $j_s = \rho^2\sqrt{1-\rho^2}$ (see, for example, Fig. 18. in [32] or section 3.2.2 and Fig. 3.2). Rewriting the condition (4.18) in dimensional units, we find a stability condition relating the winding number n of the solution with the number $\frac{\phi}{\phi_0}$ of flux quanta penetrating the ring:

$$\left| n - \frac{\phi}{\phi_0} \right| \leq \frac{R}{\xi\sqrt{3}}. \tag{4.19}$$

This condition is consistent with the ground state found by minimizing the free energy with a solution in the form of Eq. (4.14). As seen in Fig. 4.3, the ground state is reached when the value of $\left| n - \frac{\phi}{\phi_0} \right|$ is minimal.

4.3 Phase slip Simulations

4.3.1 Mathematical formulation of the problem

According to Eq. (4.18), the winding number needs to be changed in order to reach a stable state. The new solution will be closer to the ground state. Therefore, the superconductor should reach a state with lower current and energy. Indeed, remembering that the superconducting current is

$\mathbf{j_s} = -\mathbf{a}|\psi|^2 - \frac{i}{2}(\psi^*\nabla\psi - \psi\nabla\psi^*)$, the transition to a state of lower current cannot occur without modifying the phase and hence the value of k. We observe a transition from the solution ψ_{k_0} to a different solution ψ_{k_1}. Because of periodic boundary conditions, the transition from k_0 to k_1 requires discontinuity in the phase. Since the order parameter is a single-valued function, this discontinuity or jump should be of $2\pi n$, n being an integer number. Moreover, $\psi = 0$ at the phase slip center to fulfill the continuity condition for the order parameter. Therefore, the transition between two solutions is a resistive phase slip. Once the slip is achieved, the phase recovers continuously.

In our simulation, we start with $k_0 = 0$. We expect the evolution to a state $k_1 = \frac{2\pi n_1}{l}$ after a number n_1 of 2π phase slips (or an equivalent number of bigger phase slips) corresponding to the final phase:

$$\theta = \frac{2\pi n_1}{l}x + \theta_0. \tag{4.20}$$

If the number n_1 of phase slips is equal to the integer part of the ratio $\frac{\phi}{\phi_0}$, the final state reached is the ground state, but as we show, this is not always the case and it is difficult to predict (see Sec. 4.3.3 for details). In other words, we observe the transition after an infinitesimal perturbation from the solution

$$\psi_0 = \sqrt{1 - a^2} \tag{4.21}$$

to another solution after n_1 phase slips

$$\psi_{\frac{2\pi n_1}{l}} = \sqrt{1 - (a - 2\pi n_1/l)^2}\, e^{i(2\pi n_1 x/l + \theta_0)}. \tag{4.22}$$

This solution may correspond to the ground state or a new metastable state of lower energy.

4.3.2 The single phase slip

In the simulations, we use Fast Fourier Transforms for spatial derivatives and Runge-Kutta method for time evolution. The algorithms and parts of the code are presented in appendix B. As discussed in section 4.3.1 and as described in the LAMH theory, the amplitude of the order parameter, vanishes in a very narrow region for a very short time (see Fig. 4.4(a)). Then, the amplitude relaxes to a uniform state with a higher value than it had initially. The saddle state solution predicted in section 4.1.2 and presented in Fig. 4.1 does indeed correspond to our simulation of the TDGL equations. Even though the value of the current is in the end lower, the superfluid density is higher. Comprehensively, stability comes together with a lower kinetic energy. The phase of the order parameter develops a sharper sinusoidal form, until the minimum and the maximum disconnect, at the very moment when the amplitude vanishes and in the same region,

as seen in Fig. 4.4(b). Afterwards, it relaxes to a sawtooth pattern corresponding to the new state (4.20) so that both amplitude and phase are consistent with the solution (4.22).

The superconducting current behaves similarly to the amplitude of the order parameter. It vanishes at the same point and time as the phase slip. This region becomes resistive at that moment. Contrary to the amplitude, the process occurs with a decrease of the supercurrent, as explained in section 4.3.1 and as one can observe in Fig. 4.4(c).

According to the Josephson equation $\frac{d\Delta\theta}{dt} = \Delta\Phi$, the electrostatic scalar potential (see Fig. 4.4(d)) and the phase are directly connected ($\Delta\theta$ and $\Delta\Phi$ are respectively the phase and electrostatic potential difference taken between two arbitrary points, see section 2.3.2). As the amplitude of the order parameter goes to zero, the average speed of the electrons is reduced and thus some of them gather before the region of the phase slip. Therefore, there is a deficit of electrons at the end of the region and the electric field is created. This voltage influences the phase of the order parameter, until it makes a slip of 2π when the amplitude vanishes. Then, the amplitude recovers and the voltage relaxes back to zero, as the electrons spread again uniformly along the wire. The "discontinuity" in the phase remains.

We have considered different types of perturbation to trigger the dynamics in absence of noise. We found out that in order to start a phase slip process, it is crucial that the perturbation is nonuniform. Indeed, if the symmetry is conserved after the perturbation, no region is selected for the phase slip and the transition does not occur.

The characteristic values for the process are deceiving because the values depend strongly on the material and the thickness of the ring. For example in NbN we estimate $\tau_\theta \approx 1$ ps. The total time of the transition between two states separated by a single phase is thus of the order of 100 ps and the characteristic voltage appearing in the ring of about $10\mu V$.

4.3.3 Multiple phase slips solutions

Here we investigate the case of a transition where the stable state and the initial state are separated by more than one phase slip. The stability condition (4.18) is insufficient to predict the final state and the number of phase slips that occur. The best prediction of the number of phase slips is given by finding the winding number of the ground state (see Fig. 4.3). In general, the maximum number of phase slips that can happen is equal to $\left|n - \frac{\phi}{\phi_0}\right|$. Starting with $n = 0$, a high magnetic flux will thus be a good condition to observe multiple phase slips. However, we found out that the ground state is reached only for certain values of the parameter u.

If $u \gg 1$, the phase θ relaxes faster than the amplitude ρ. It favors multiple phase slips to happen at the same spot, one after another, as seen in Fig. 4.5(a). The oscillations of the amplitude of

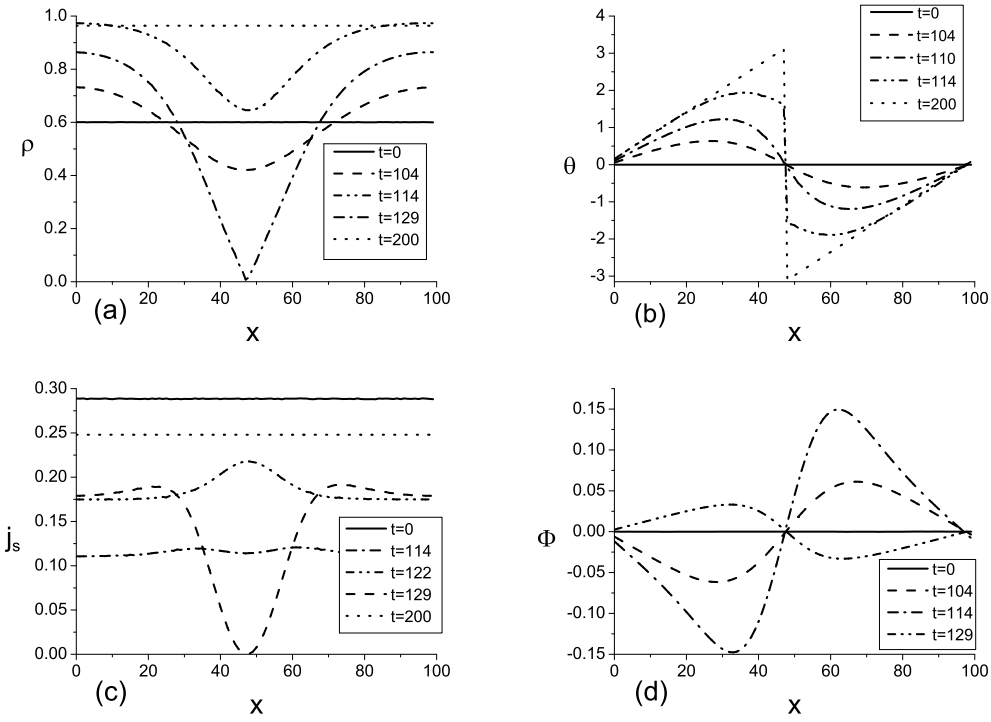

FIGURE 4.4: Distribution of the order parameter amplitude ρ (a), phase θ (b), supercurrent j_s (c) and electrostatic potential Φ (d) at different times during a single phase slip event.

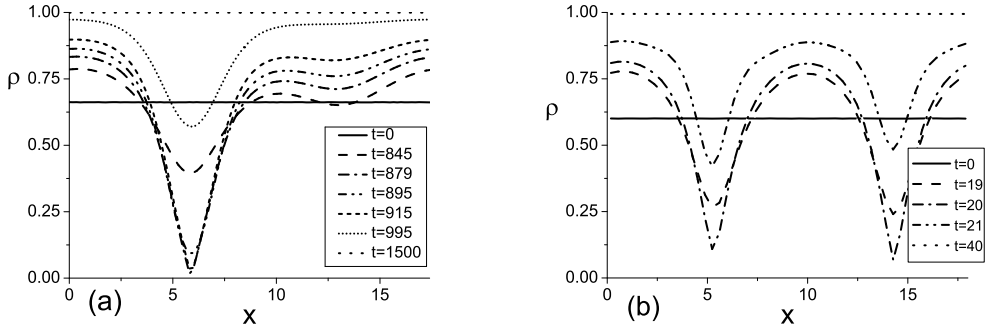

FIGURE 4.5: Evolution of the distribution of the order parameter amplitude ρ for two consecutive phase slips (a) and two simultaneous phase slips (b).

the order parameter during the time of the transition are similar to those observed in Ref. [64]. In this case, the order parameter almost always relaxes to the ground state, even if an intermediate state is stable according to condition (4.18).

If $u \ll 1$, the amplitude ρ relaxes faster than the phase. It favors processes where multiple phase slips happen more or less simultaneously at different phase slip centers as seen in Fig. 4.5(b). Therefore, after a certain number of simultaneous phase slips, the amplitude relaxes to a new uniform state which will be the final stable state. In that case, the final state is not necessarily the ground state. These observations are consistent with the observations made in Ref. [64] that for $u \ll 1$ the final state may be "further away" from the ground state than for $u \gg 1$.

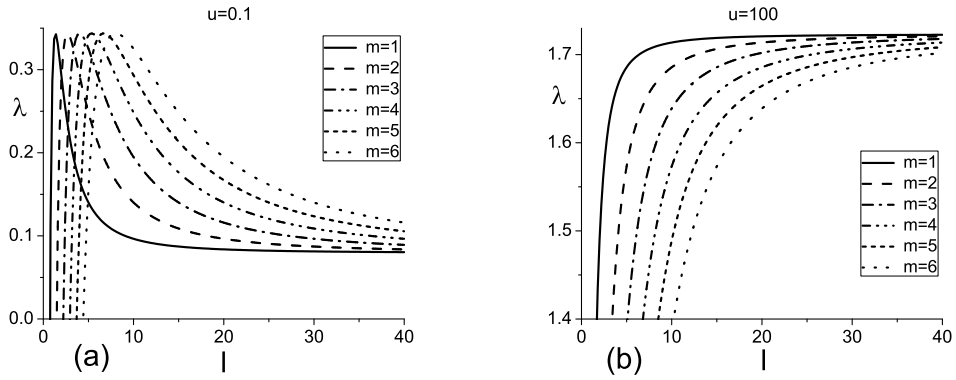

FIGURE 4.6: Eigenvalues λ corresponding to different modes m as a function of the size l of the ring for $u = 0.1$ (a) and $u = 100$ (b). Here $k = 0$ and $a = 0.8$. When $u \gg 1$ there is no competition between the modes and consecutive phase slip processes will always dominate. With $u \ll 1$, the highest eigenvalue depends on the size of the ring. For larger length the simultaneous phase slips will dominate.

Mathematically, the importance of the parameter u is emphasized by plotting different eigenvalues as a function of the size of the ring. For $u \gg 1$, the highest eigenvalues always correspond to single phase slips happening one at a time. However, for $u \ll 1$, different eigenmodes have highest eigenvalue depending on the size of the ring. For large sizes, the simultaneous multiple phase slips modes are the most unstable (see Fig. 4.6).

It is possible to differentiate three cases when multiple phase slips happen:

1. There is only one phase slip center and the amplitude of the order parameter reaches zero several times at the same location before relaxing to a stable state. This is the general consecutive phase slips case.

2. There are more phase slip centers and the amplitude reaches zero at the same time at all locations.

3. There are more phase slip centers but the amplitude reaches zero at a different time for each location.

Here we consider cases 2. and 3. as simultaneous phase slips. Indeed, the amplitude starts to decrease at the same time for all phase slip centers, so that the processes are called simultaneous. In Fig. 4.5(a) one can also see the competition between simultaneous and consecutive phase slips. Indeed, in that simulation, the amplitude decreases first on two separate spots, but in the end, both phase slips happen consecutively on the same spot. The Fig. 4.7 shows the different types of behavior depending on the parameter u. We confirm that the ground state is only reached for $u \gg 1$. Indeed, for those simulations, we have $\frac{\phi}{\phi_0} \simeq 5$ and we observe five phase slips only when $u = 100$. However, the number of phase slips does not necessarily grow monotonically with the value of u. Indeed, for $u = 1$, we observe less phase slips than for $u = 0.5$ and $u = 0.1$.

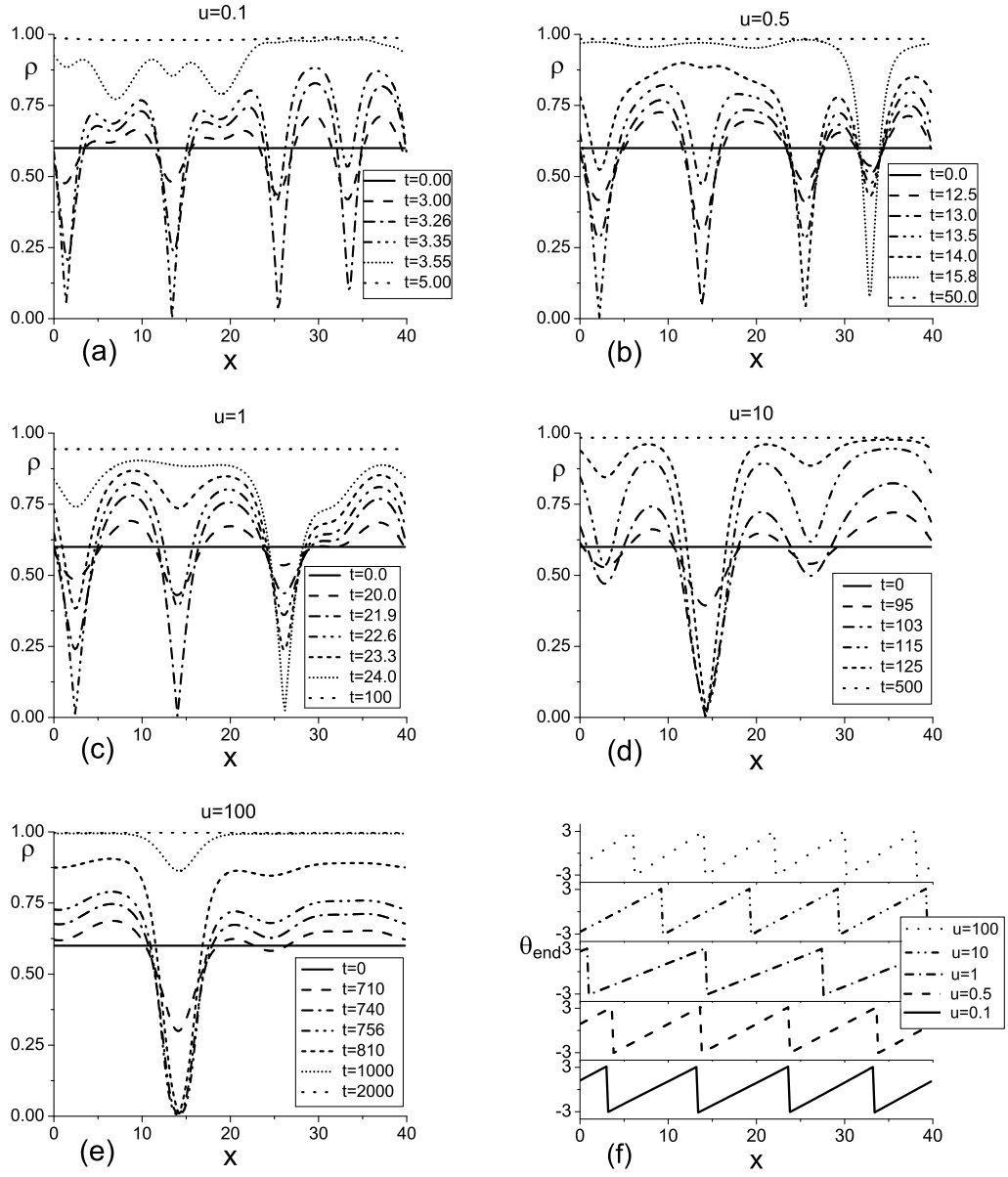

FIGURE 4.7: Evolution of the distribution of the order parameter amplitude ρ (a)-(e) exhibiting the competition between simultaneous and consecutive phase slips for different values of u and distribution of the corresponding phase θ_{end} at the final stable state (f).

According to Eq. (4.17) and Fig. 4.6, the size of the ring restricts the number of phase slip centers. However, at small sizes, multiple phase slips are often ruled out because the magnetic flux is too low or too high. In particular, the magnetic flux induces more phase slips than the number of phase slip centers allowed by the eigenmodes if

$$\left| n - \frac{la}{2\pi} \right| > \sqrt{l^2 \left[6 \left(\frac{2n\pi}{l} - a \right)^2 - 2 \right]}. \tag{4.23}$$

This condition restricts greatly the choice of parameters. In our case, with $k = 0$, we need

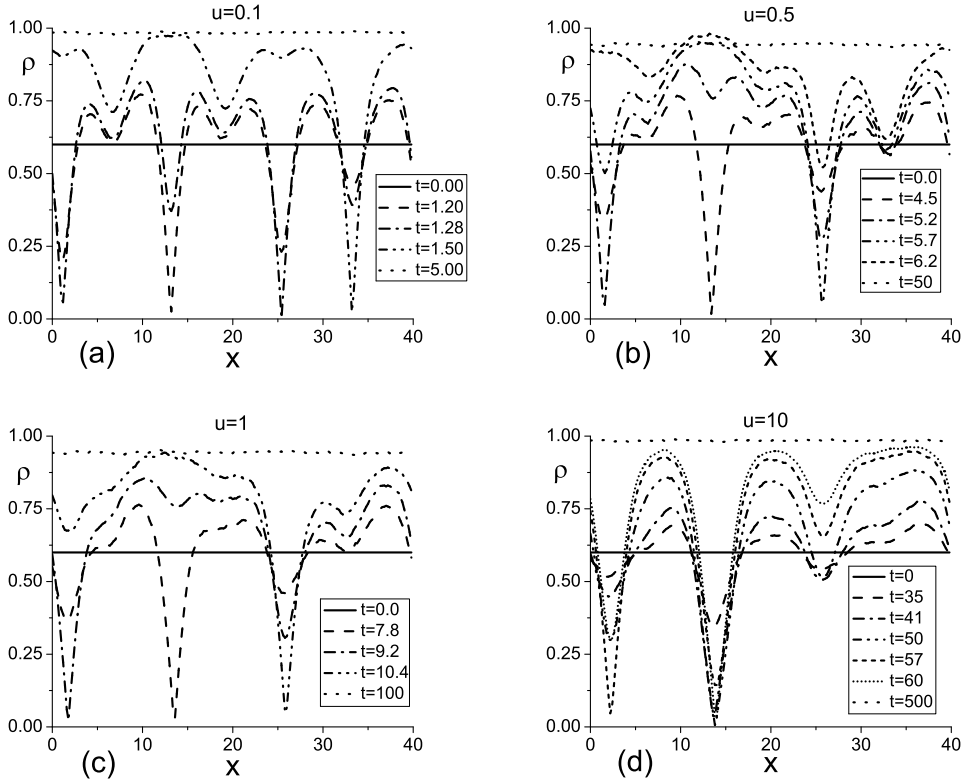

FIGURE 4.8: Evolution of the distribution of the order parameter amplitude ρ in the presence of a Langevin noise of the order of 10^{-1}. The phase slip are accelerated and happen less simultaneously. For $u = 10$ (d), we observe a mixing between consecutive and simultaneous phase slips.

$a < \sqrt{\frac{8\pi^2}{24\pi^2-1}} \simeq 0.578 \approx \frac{1}{\sqrt{3}}$. Therefore, it limits the simulations to an area which is almost stable and therefore intrinsically not prone to simultaneous phase slips.

As described in Eq. (4.12), we add a Langevin noise. The amplitude of the noise corresponding to typical experimental values is on the order of 10^{-3} which does not create any noticeable difference with the noiseless situation (all simulations excepting those shown in Fig. 4.8 were performed using a Langevin noise of this amplitude). However, according to our simulations the increase in the level of the noise leads to a stronger instability. We notice that the phase slips are accelerated, especially in the beginning of the process. In the multiple phase slips case, the behavior of the order parameter can be significantly altered. The phase slips tend to happen "less simultaneously" and we even observe a mixing of consecutive and simultaneous phase slips [see Fig. 4.8(d)]. Rather surprisingly, the increase in the noise does not necessarily lead to the relaxation of the order parameter closer to the ground state value. Sometimes we observe the opposite. For $u = 0.5$, increasing the noise reduced the number of phase slips from four to three as one can see by comparing Figs. 4.7(b) and 4.8(b). We also note that the general conclusions of the stability analysis and the role of the parameter u stay valid. Last but not the least, in the absence of noise, a nonuniform perturbation needs to be applied in order to initiate the phase slip process.

As pointed out in Ref. [64], a strong magnetic field might trigger strong normal currents and destroy superconductivity because of heating effects. In our simulations, a strong magnetic field is indeed required to trigger simultaneous phase slips. However, in the $u \ll 1$ case, we observe simultaneous multiple phase slips already at magnetic fields on the order of one Gauss for an aluminium sample of length $L = 40\xi$ and $\xi = 100$nm. This magnetic field is smaller than the value described as the maximum field sustainable by such a ring in Ref. [65]. The estimate of the heating of the ring may be made using Ohm's law, as we consider that during a phase slip event, a part of the ring of length ξ behaves like a normal conductor of conductivity σ_n during a time τ_θ and sustains a current J_s (in CGS units). The energy dissipated per unit of volume is then:

$$E = \frac{J_s^2}{\sigma_n}\tau_\theta = \frac{\left[\phi_0 a(1-a^2)\right]^2}{16\pi^3\xi^2\lambda_{\text{eff}}^2}. \tag{4.24}$$

This energy is less than a quarter of the condensation energy $\frac{H_{c2}^2}{16\pi\kappa^2}$ and such a small heating should not have any significant effect on the experimental detection of the phase slip. The case of multiple phase slips is more complicated and depends on the quality of the contacts of the sample with the thermostat. We believe that for the case of a free standing ring with a reasonable number of consecutive phase slips, the local temperature does not reach T_c because of the large time scales involved [see Figs. 4.7(d) and 4.7(e)]. In the case of simultaneous phase slips, simulations confirm that the phase slip centers spread along the whole sample and therefore the distances are large in comparison with the heat diffusion length [see Figs. 4.7(a) and 4.7(b)]. In that case, the local heating is similar to the single phase slip case.

4.4 Conclusions of this chapter

In this chapter, we gave a brief overview of the phase slip theories and explained in more details how the phase slip solution is derived in the LAMH theory.

We formulated the stability condition for the superconducting state of a 1D ring in a constant magnetic field. Using the TDGL equations, we found out that the state is stable when the difference between the vorticity and the number of flux quanta enclosed in the ring is small. The relaxation towards the stable state must therefore involve one or more phase slips. The simulation of the TDGL equations agreed with these predictions.

The study of the multiple phase slips case revealed the importance of the ratio u between the characteristic relaxation times of the amplitude and the phase of the order parameter. While $u \ll 1$ is favoring simultaneous phase slips, evolutions with $u \gg 1$ more often happen with consecutive phase slips. Therefore, $u \gg 1$ is often a necessary condition for the relaxation to the ground state. The effect of the Langevin noise present in the equations is also studied. It appears

that for higher values of the noise, the behavior may be different; but the general conclusions of the study are still valid. In some cases, phase slips may be favored by local inhomogeneities [67] which could favor the simultaneous phase slips case, but this goes beyond the scope of the present study.

Chapter 5

Vortex nucleation in 2D: from ordered to chaotic dynamics

We take the investigation on the phase slip phenomena of chapter 4 to the two dimensional (2D) case. Many different possible dynamics emerge and lead us to many aspects of the same problem: how topological defects are created ? Many results of this chapter have been published in [40, 68, 69].

5.1 Phase slip dynamics in 2D

5.1.1 Vortices in our geometry

The kinetics of vortex production in superconductors and superfluids is one of the intriguing problems of condensed matter physics. It is interesting not only in the field of solid state physics but as we will see in section 5.2 and 5.3, the creation of topological defects is a major area in other branches of physics. In the last few decades different scenarios for vortex production in superconductors and superfluids were proposed. The most common way to produce vortices is to increase the superfluid velocity in order to reduce the energy barrier between homogeneous flow and flow with vortices. This mechanism is observed in rotating ^{3}He where vortex nucleation and critical velocities are measured [70–72].

We saw in chapter 4 that fluctuations of the order parameter can lead to the 2π jump of the phase of the order parameter in a region where the amplitude of the order parameter is reduced to zero: the phase slip center. Such phase slip events should in theory happen in 2D geometries as well. The first idea that comes to mind when we bring the phase slip phenomena to the 2D case is the

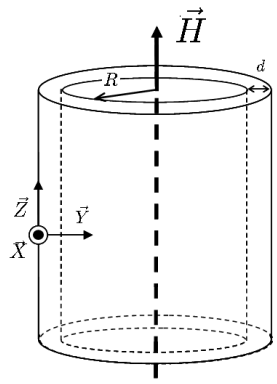

FIGURE 5.1: Geometry of the system: a 2D cylinder with an applied magnetic field **H**.

nucleation of vortices. Indeed, as noted in [3], the 1D phase slip center is the 2D topological analog of a vortex-antivortex (VaV) pair separating and moving towards the boundaries. The creation of VaV pairs has thus been the driving idea of our investigation. We model a superconducting film rolled on a cylinder in an external time-dependent magnetic field parallel to the cylinder axis as represented in Fig. 5.1. The thickness of the film d is small: $d \ll \xi \ll \lambda_{\text{eff}}$ and can thus be considered 2D. Here ξ is the coherence length and λ_{eff} is the Pearl penetration depth.

Like in 1D, we set up an external magnetic field. We discovered that the separation of a VaV pair was not created with the same conditions as phase slip centers in 1D: in fact, different dynamics are possible.

5.1.2 The phase slip line

The topology of a vortex as described in section 2.2 makes it an ideal object to create the 2π difference and to carry it along the sample. Indeed, the creation of a VaV pair in the sample and its separation towards the boundaries represent the topological analogue to the 1D phase slip center (see Fig. 5.3 for an idea of the topology of the phase corresponding to a VaV pair). However, for the homogeneous geometries, if we investigate the fluctuations between different metastable states, theoretical analysis predicts a purely 1D transition. As seen in section 3.3.2.1 with the analysis of Eq. 3.50, the instability develops in a 1D fashion. Our simulations confirmed this fact as seen in Fig. 5.2. The order parameter decreases to zero along a line traversing the whole sample. The phase then slips by 2π at the same moment along the whole line. These results contradict our intuition because during the separation of a VaV pair, the order parameter goes to zero at only two locations instead of a whole line and should therefore be energetically favorable. In reality, a VaV pair represents a complex topological configuration which has little probability to occur in a uniform configuration deprived of strong fluctuations. Moreover, the speed of the separation is slow with regard to the time required for a 1D-like phase slip. The VaV pair is therefore not necessarily the evolution that minimizes the energy.

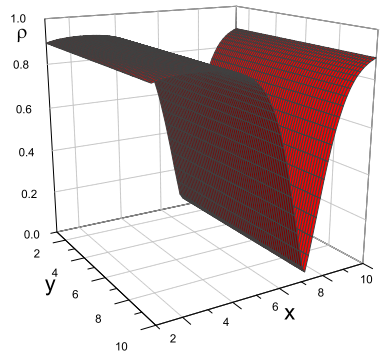

FIGURE 5.2: Amplitude of the order parameter during a 1D type phase slip (phase slip line) in a 2D simulation.

This 1D evolution in a 2D sample is called the phase slip line (PSL) and has the same characteristics as a phase slip center. It was first analyzed by A. Weber and L. Kramer [73] using the time-dependent Ginzburg-Landau (TDGL) equations. Phase slip lines have been first studied as the 2D extension for phase slip centers: experimental and theoretical works investigated the current-voltage characteristics when wider wires that could no longer be considered one dimensional were submitted to a current. In particular, the current-voltage characteristics of 2D microbridges were investigated. Microbridges are the intermediate geometry between 1D wires and 2D films: the thickness is less than the coherence length ξ and the width of the channel lies between ξ and the Pearl penetration depth λ_{eff} (see section 2.1.4 and 2.1.5 for a description of those quantities). The current-voltage characteristics of sample exhibiting PSLs present the same features (increasing resistivity and voltage steps) as the 1D phase slip centers (see [52] for a recent review).

5.1.3 Kinematic vortices and vortex rivers

When a little bit of disorder is present in the system, a slightly different evolution can occur. The order parameter is strongly suppressed along a straight line across the film like for a PSL but it reaches zero only at two points on this line. These weakly 2D dynamics involve a strongly anisotropic pair of vortices which was found for wider bridges by A. Weber and L. Kramer [73]. The inhomogeneity caused by current contacts leads as well to a certain inhomogeneity across the film and the qualitative picture of the phase slip phenomena is unchanged [74]. This pair of vortices is called kinematic vortex-antivortex pair [75]. It moves quickly in opposite directions along this line propagating the 2π jump of the phase. This line of reduced order parameter, where the vortices will be located, is referred to as a vortex street or a vortex river. There again, phase slips occur without formation of well defined VaV pairs. The velocity of kinematic VaV pairs is large because the value of the order parameter is small along this line. Kinematic vortices can be described as vortices whose motion is favored by the lower value of the order parameter in the direction of their travel.

In 2D samples penetrated by a magnetic field and carrying a transport current, kinematic vortices can form as well. A. I. Larkin and Yu. N. Ovchinnikov [76, 77] first predicted the nonlinearity of the conductivity in the flux flow regime due to the deformation of the vortex core during the vortex motion. Their non-trivial derivation is based on the difference between the relaxation time of the order parameter and the relaxation time of the nonequilibrium quasiparticles. Their prediction was supported by different experiments (see [78] and references therein). In the common flux flow regime, as explained in section 2.2, the Abrikosov lattice of vortices moves as a whole. However, when the velocity of the vortices reaches a certain value, the lattice is destroyed and it becomes favorable for vortices to follow one another and to form rows. Such formation of vortex rivers was first shown by numerical simulations of the TDGL equations [79, 80]. It has been as well confirmed by experiments by freezing the vortices in their river configuration on pinning centers [81]. Indeed, a moving vortex will leave behind it a region of reduced order parameter and the neighboring vortex will follow this region where its motion is favored. To simplify, it costs less energy if the order parameter is reduced only once. This is a purely dynamical configuration: when reasoning like in equilibrium, vortices of the same polarity always repel each other and form the Abrikosov Lattice (as seen in section 2.2), which does not apply here. As such, kinematic vortices represent a rare case of dynamic ordering through vortex-vortex *attraction*.

5.1.4 Creation from the phase topology

A simple way to witness the topological analogy between a VaV pair and the 1D phase slip center is to induce a 2π phase difference in the middle of the sample. This is actually an artificial way to induce a different current in one part of a sample (a similar idea was used in [82, 83]). We simulate the relaxation of the superconducting state using the TDGL equations from a solution where a phase difference line has been introduced. We use x and z as the spatial coordinates as defined in Fig. 5.1:

$$\begin{cases} \psi(x,z,t=0) = & \sqrt{1-a^2} & \text{for } 0<x<l_1 \text{ or } l_2<x<L \\ \psi(x,z,t=0) = & \sqrt{1-(a-\frac{2\pi}{L})^2}e^{i(\frac{2\pi}{L}x)} & \text{for } l_1<x<l_2 \end{cases} \tag{5.1}$$

From this initial state, containing a phase difference line between the position l_1 and l_2, we observe a VaV pair: the vortex and antivortex form at the singularity of the order parameter, at each end of the 2π phase difference. Initially they form at l_1 and l_2. The initial state can be adjusted to observe either the dissociation of the pair to the boundaries (the supercurrent between the vortex and antivortex drives them in opposite directions) or the attraction of the vortex and antivortex until the annihilation of the pair in the middle of the film. The amplitude is plotted in Fig. 5.6. Introducing more phase slip lines creates as many pairs as phase slip lines introduced as seen in Fig. 5.5.

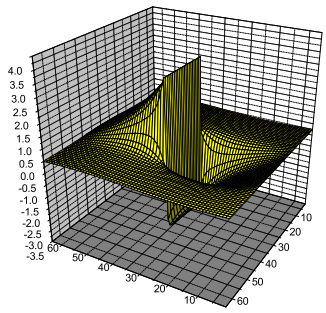

FIGURE 5.3: Phase of the order parameter showing a VaV pair. We notice the topological phase jump line of 2π.

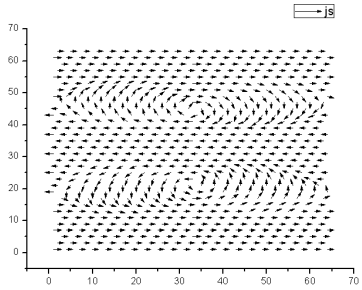

FIGURE 5.4: Superconducting current showing a VaV pair in a superconductor

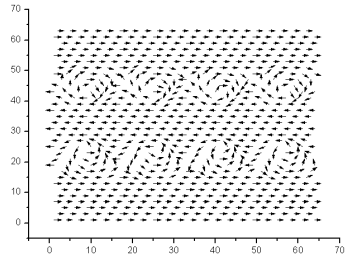

FIGURE 5.5: Superconducting current showing four VaV pairs in a superconductor

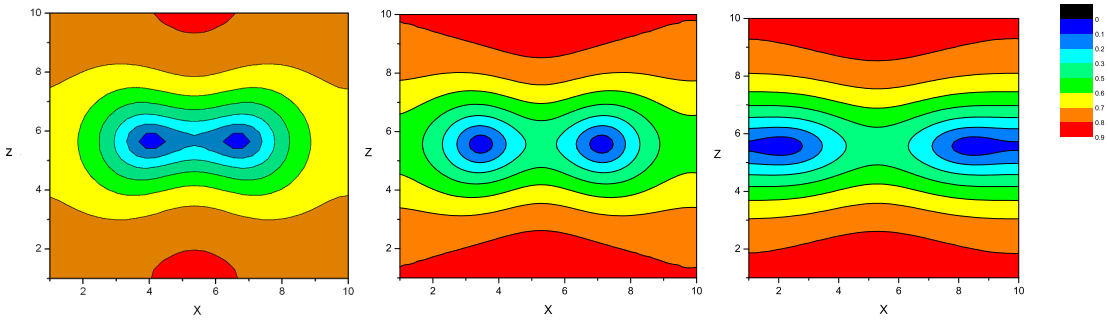

FIGURE 5.6: Distribution of the order parameter amplitude ρ at different times showing a vortex-antivortex pair dissociation.

These results confirm the VaV pairs as a potential vector for phase slippage in 2D, but we are not completely satisfied as we look primarily for natural transitions between metastable states.

5.2 The Kelvin-Helmholtz instability

5.2.1 The basic principles

The Kelvin-Helmholtz instability is a well known phenomenon of classical hydrodynamics which occurs at the interface of two fluids which are in relative motion with respect to each other [6]. It is characterized by the discontinuity of the velocity tangential to the surface of separation between the two fluids. It was first investigated by Lord Kelvin [84] to describe the waves created by wind on the surface of water which was unstable regarding the Helmholtz criteria [85]. Kelvin was followed by Rayleigh [86] who analyzed the flapping of sails and flags. The condition for instability is commonly derived for ideal fluids (inviscid incompressible flow). The situation where two ideal liquids sliding along each other starts to be unstable at a certain critical relative velocity v_{rc} given by:

$$\frac{1}{2}\frac{\rho_1\rho_2}{\rho_1+\rho_2}(v_{rc})^2 = \sqrt{\sigma_{st} g|\rho_1-\rho_2|} \tag{5.2}$$

where ρ_1 and ρ_2 are the mass density of the liquids, σ_{st} is the surface tension at the interface and g is the gravitational constant.

However, ordinary fluids are not ideal and the theory is difficult to check experimentally. Indeed, the initial state is impossible to prepare as the shear flow discontinuity is never an equilibrium state for viscous fluids since it is not a solution of the Navier-Stokes equation.

The discovery of the superfluidity of helium (He) by Pyotr Kapitsa, John F. Allen and Don Misener in 1937 brought a better way to confront the original theory with experiments as the viscosity is absent. For example, in superfluid ^{3}He, the critical velocity at which vortices start to form is lower in the ^{3}He-B phase than in the ^{3}He-A phase and one can prepare an experiment where vortices are present in the B side of the AB interface but not in the A side [87]. However, the critical velocity at which the vortices start crossing the AB interface is different from that of the original Kelvin-Helmholtz because one needs to take into account the specificities of ^{3}He. New theoretical derivations [88, 89] were then made in good agreement with the experimental results (for a review on these developments, see [90]).

5.2.2 Kelvin-Helmholtz in superconductors

In superconductors, a paradigm of the Kelvin-Helmholtz can be obtained where the superconducting current plays the role of the flow of the fluid while resistivity plays the role of the viscosity. A simple way to create the initial state of the Kelvin-Helmholtz instability is to have next to each other two superconducting materials with different coherence length ξ. Such a configuration, presented in Fig. 5.8, is described by using equation (3.6):

$$u\left(\frac{\partial\psi}{\partial t}+i\Phi\psi\right) = \psi-\psi|\psi|^2-\xi_r^2(i\nabla+\mathbf{a})^2\psi+\eta,$$

while the equation for the current (4.13) is unchanged:

$$\nabla^2\Phi = -\nabla\left[\frac{i}{2}(\psi^*\nabla\psi-\psi\nabla\psi^*)+\mathbf{a}|\psi|^2\right]$$

We remind that space and time coordinates (x,z,t) are measured in units of the coherence length ξ and of the characteristic relaxation time of the phase $\tau_\theta = \frac{4\pi\lambda_{\text{eff}}^2\sigma_n}{c^2}$ (σ_n is the conductivity of the normal state and c is the speed of light). The Pearl penetration depth $\lambda_{\text{eff}} = \frac{\lambda_L^2}{d}$ has been used instead of the London penetration depth λ_L since the thickness d is small. The vector potential $\mathbf{a}$ is written in units of $\frac{\phi_0}{2\pi\xi}$ (ϕ_0 is the flux quantum) and the electrostatic potential Φ in units of $\frac{\hbar}{2e\tau_\theta}$, with e being the elementary charge and $\hbar$ as the reduced Planck constant. The only

dimensionless parameter left in the equation is the ratio $u = \frac{\tau_\rho}{\tau_\theta}$ between the two characteristic times. The Langevin noise η has the same order of magnitude as in section 4.2.2

Here again, the corrections to the magnetic field are neglected due to the small thickness d of the film $d \ll \xi \ll \lambda_{\text{eff}}$. Applying a constant magnetic field to such a sample will induce a stronger current in the region which has the smallest coherence length. Following the derivation for the stationary case in appendix C, following equations (C.16) and (C.3), we have indeed $|j_s| = \left(1 - \xi_r^2(a - k_r)^2\right)\left(\frac{\partial\theta}{\partial x} - a\right)$. In section 5.4.7 we give an example of simulations using this geometry. Further developments, analytical and numerical, following the original theory might be interesting as well.

5.3 The Kibble-Zurek mechanism

Vortices, VaV pairs and in general 2π jumps in the phase of the order parameter can be seen as defects in the topology of the order parameter. The creation of such topological defects is a subject for many different fields and one can easily draw a parallel between our investigation and many other systems performing second order phase transitions. As a matter of fact, the greatest of all systems, our universe, might have been subject to series of symmetry-breaking phase transitions in its early stage after the Big Bang. Indeed, in the context of grand unified theories, Kibble [91] investigated the possibility of the creation of topological defects during the phase transitions that might have happened during the inflationary state of the creation of the universe. In that context, topological defects are cosmological objects (monopoles domain walls and cosmic strings) that might have a role in the configuration of our universe. Cosmology is an area where a lot of theories have to remain hypothetical due to the difficulty of finding observable evidences. However, Zurek ([92, 93]) proposed that the creation of topological defects may be tested in other phase transitions and more particularly in condensed matter systems undergoing second order phase transitions. The original Kibble-Zurek mechanism thus describes the creation of topological defects during a second order phase transition driven by a temperature quench.

When the sample is quickly quenched through the critical temperature T_c, the nucleation of the low temperature phase starts in different places with uncorrelated phases of order parameter. Then, domains grow and start to overlap leading to the formation of topological defects. The Kibble-Zurek mechanism has been experimentally investigated in different systems with promising results. Experiments in liquid crystals were carried out [94] [95] as well as in superfluid ^{4}He [96], which was the system originally proposed in [92]. Last, ^{3}He was investigated as well [97–99]. Of course as suggested in [93], superconductors are a system of choice as well. Evidence of topological defects in relative agreement with the KZ mechanism was found in high temperature superconductors [100]

after some unsuccessful attempts which shows that the temperature quench needs to be really fast [101].

Other works have been influenced by the KZ mechanism demonstrating the interest of the physics community for the problem of creation of topological defects [102–104]. It is interesting to note that on one hand these dynamics are stochastic and sensitive to small variations of the initial conditions. On the other hand the dependence of the vortex density on the quench time and their spatial correlation are universal.

5.3.1 Analytical description of the Kibble-Zurek mechanism

As the Kibble-Zurek mechanism occurs during a second order phase transition, the Ginzburg-Landau framework appears ideal to analyze it. We saw in section 3.1 that the relaxation time of the dynamics of the amplitude of the order parameter is $\tau_\rho = \tau_{GL} = \frac{\pi\hbar}{8(T_c - T)}$.

The dynamics are therefore considerably slowed down close to T_c. During a quench, the temperature is lowered rapidly through T_c and there exist a region where the relaxation time τ_ρ of the order parameter will be larger than the characteristic time τ_Q of the temperature quench . To simplify, in this region, the dynamics are "frozen" and the order parameter will start to relax only when τ_ρ starts to be comparable with τ_Q. At this "freeze-out" time, the dynamics of the order parameter start: it grows rapidly, but the coherence will be limited to domains, the typical size of which is ξ^2. As seen in section 2.1.4, the coherence length grows with the temperature: $\xi = \sqrt{\frac{\hbar^2}{4m|\alpha|}} \propto \sqrt{\frac{T_c}{T_c - T}}$. Hence, the faster the quench, the lower will be the freeze-out temperature and the smaller will be the freeze-out coherence length. Topological defects will appear at the boundary of the domains, once they grow and overlap. As a consequence, the faster the quench, the higher should be the density of topological defects created at the freeze-out time. A simple derivation of this analysis can be found in [93].

In superfluid helium, the transition can easily be controlled by the pressure: the critical temperature can be shifted as well. However, it is not so easy in superconductors and one needs to rely on pure temperature quench which in bulk superconductors is governed by the heat diffusion which is a slow process. Using high T_c superconductors like in [101] and later [100] does permit to increase the temperature gradient and therefore the quench rate. Using thin films as suggested in [93] is also a potential direction, as well as using annular geometries where the magnetic flux can be trapped and measured [105].

5.3.2 Quenching a superconductor using the magnetic field

The time-dependent equations can be coupled with the heat diffusion equation in order to simulate the temperature quench required for the KZ mechanism (see [106] and section 6.2). However, as the characteristic time τ_{GL} diverges at T_c, one needs to be careful about the validity of the results and some corrections to the equations might be necessary.

Our idea here is that the superconducting phase transition can be driven by a magnetic field as well: the density of the topological defects might even be easier to predict as the temperature stays fixed. A first possibility is to apply an external field that we will decrease below the upper critical field H_{c2}. Here, we look for a constant field that will involve a transition from the initial metastable state going through a state where the order parameter is uniformly reduced to zero.

Analytically, we linearize the TDGL Eq. (3.3) in small fluctuations of order parameter $f(\mathbf{s},t) = \psi(\mathbf{s},t) - \psi_0$ and search for a solution in the form $f(\mathbf{s},t) = \sum_{\mathbf{k}} C_{\mathbf{k}} \exp\left(i\mathbf{k}\cdot\mathbf{s} + \lambda_{\mathbf{k}} t\right)$. It is clear that the transverse k_z component always contributes to the stability of the initial state as we saw in chapter 3. Therefore, the condition $\lambda_{\mathbf{k}} > 0$ is the same as in 1D: $|n - \frac{\phi}{\phi_0}| < \frac{R}{\xi\sqrt{3}}$, where ϕ is the magnetic flux through the ring at $t > 0$ and n the winding number of the stationary solution. It defines the first critical value of the external field $a_{c1} = 1/\sqrt{3}$. Therefore, in the low field limit $a_{c1} \leq a \leq 1$, the dynamics will be similar to the 1D case with very weak z-dependence.

The situation is different when the field a increases further. Dropping $k_z = 0$, the eigenvalues are:

$$\lambda_{\mathbf{k}}^{(1,2)} = -\psi_0^2/2 + (1 - 2\psi_0^2 - a^2 - k^2)/u \pm \sqrt{(16u\psi_0^2 a^2 + \psi_0^4(u-2)^2 + 16k^2a^2)/4u^2}, \qquad (5.3)$$

and $\lambda_{\mathbf{k}=0} = \frac{1-2\psi_0^2-a^2}{u} - \frac{\psi_0^2}{2} - \sqrt{(16u\psi_0^2a^2 + \psi_0^4(u-2)^2)/4u2}$ describes the decay rate of the uniform solution. On the other hand for finite k, $\lambda_{\mathbf{k}}$ is positive and characterizes the growth of the corresponding Fourier components $C_{\mathbf{k}}$. The fastest growth is found for

$$k = \frac{1}{4a}\sqrt{-16u\psi_0^2a^2 - \psi_0^4(u-2)^2 + 16a^4}$$

and the rate is determined by

$$\lambda_{\max} = \frac{1}{16ua^2}(8(u-4)\psi_0^2a^2 + 16a^2 + \psi_0^4(u-2)^2).$$

The qualitative difference in kinetics takes place when the decay rate of the uniform solution becomes faster than the growth of the new phase.

This effect is similar to the quench through T_c in the KZ mechanism [91–93]. We find that at $a > a_{c2} = \sqrt{2}$, the order parameter is suppressed to zero and the growth of the phase with finite k is accompanied by the rapid development of vortices.

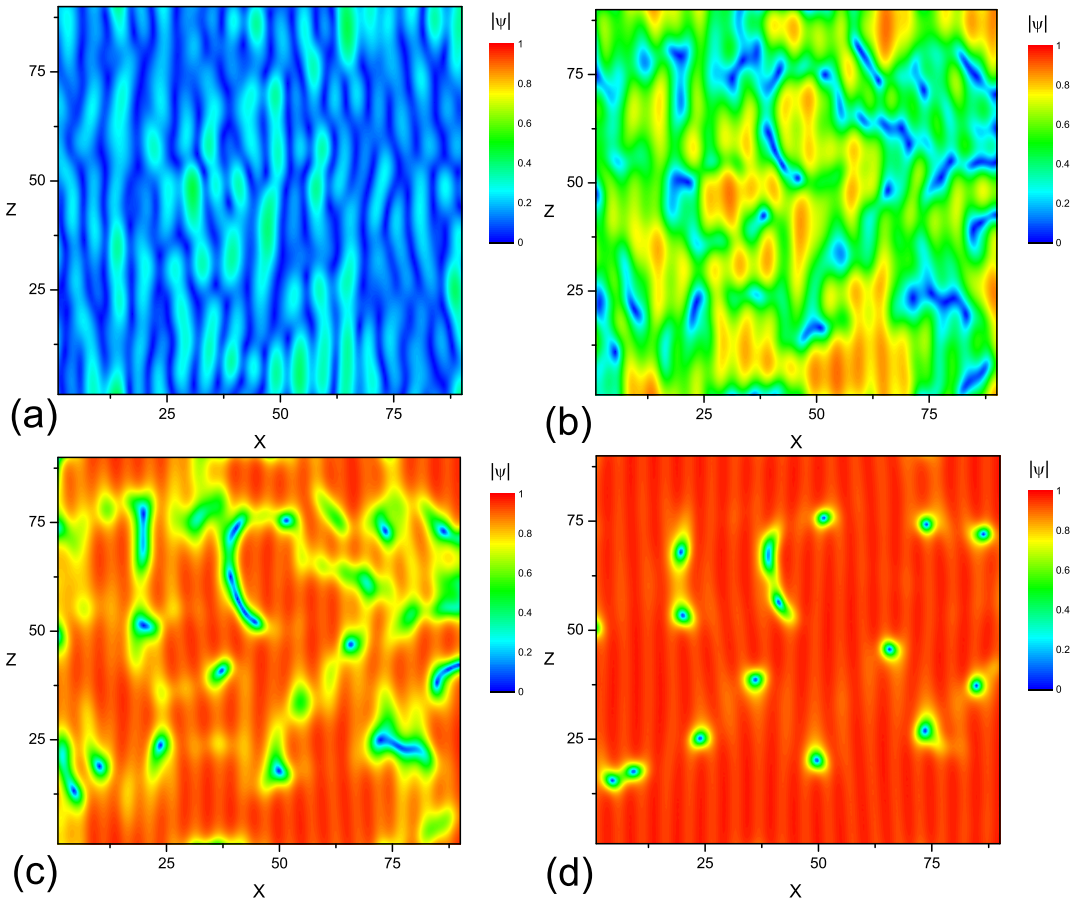

FIGURE 5.7: Evolution of the distribution of the amplitude of the order parameter after a current induced quench: t=50 (a), 65 (b), 75 (c) and 90 (d).

We remind that a_{c1} and a_{c2} do not correspond to the lower and upper critical field of the superconductor. Indeed, the magnetic field is applied longitudinally with respect to the film and these fields correspond to unstable states that will relax to states with lower current. In the case of $a > a_{c2}$, the transition is predicted to pass by a state where the order parameter is entirely decreased to zero.

The density of vortices may be estimated using Zurek arguments where the quench time should be replaced by $\tau_Q = (a^2 - 1)^{-1}$ leading to a density $n_v \propto \tau_Q^{-1/2}$ [93, 107, 108].

5.3.3 Quenching in presence of a tangential discontinuity of the velocity

In Refs. [109, 110], it was proposed that the quench occurs not only due to fast temperature change but also due to the temperature front propagation. I. S. Aranson *et al.* [111] considered the case of a temperature quench in the presence of external current. The new phase with zero current grows after the quench. Therefore on the border of the quenched region, the superfluid velocity has tangential discontinuity, leading to vortex formation, similarly to the classical hydrodynamic

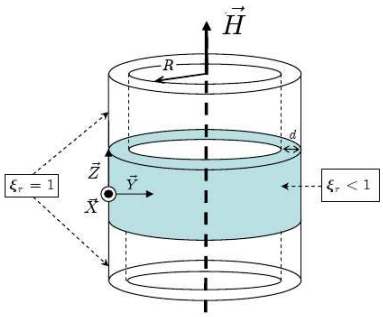

FIGURE 5.8: Geometry of a system exhibiting Kelvin-Helmholtz instability: a 2D cylinder with an applied magnetic field **H**, with a section of reduced coherence length.

Kelvin-Helmholtz (KH) instability. Moreover, the KH instability suppresses the development of KZ vortices [111]. The interplay between the different mechanisms was also analyzed in [112]. In our geometry, if we quench the sample in one region and not in the other, we have a similar situation.

5.4 From ordered to chaotic dynamics

In the geometry of the cylinder (see Fig. 5.1 and Fig. 5.8), the magnetic field is the only external parameter that needs to be adjusted in order to observe the different cases described above. Depending on the applied magnetic field and the dimensions of the ring, we follow the evolution from the deterministic PSL dynamics to the stochastic behavior described by the KZ mechanism. In this section, kinematic VaV, KZ and KH vortices are distinguished by their production mechanism although they are topologically equivalent. In the proposed model, topological defects are generated by the intrinsic quench induced by the external field. The evolution towards stochastic behavior is strongly influenced by the KH instability which develops in the presence of inhomogeneities. To model the inhomogeneity of the film we assume that there is a thin stripe of superconductor along the film with a different coherence length. The thickness of the film d is small $d \ll \xi \ll \lambda_{\text{eff}}$. Here ξ is the coherence length and λ_{eff} is the Pearl penetration depth. Therefore we can neglect all corrections to the external magnetic field **H** caused by the current in the film. The radius of the film is $R \gtrsim \xi$.

5.4.1 The magnetic field as the main parameter

To model the process of vortex formation we assume that at time $t < 0$, the external magnetic field is absent. At $t = 0$, the field suddenly appears and stays constant for $t > 0$ i.e. tangential component of the vector potential is $a\mathcal{H}(t)$, where $\mathcal{H}(t)$ is the Heaviside step function. We thus study the kinetics of the vortex generation as a function of a with different values of u.

Like in 1D, we start from an initial solution in the form $\psi_{0,0}(x,z) = \sqrt{1-(a_x)^2}$ and predict to observe the transition to the new state $\psi_{k,0}(x,z) = \sqrt{1-(k-a_x)^2}e^{i(kx+\theta_0)}$ after some 2D phase slip dynamics.

We already know that below a_{c1} the stationary solution will be stable and no dynamics should occur. When $a > a_{c1}$, some dynamics should occur, resembling qualitatively to the PSL solution. When a reaches a_{c2}, our simplified analysis predicts a quench of the superconducting phase. The criterion for kinematic vortices and KH vortices is difficult to derive analytically and the role of the size of the sample is difficult to predict. We therefore solve the TDGL equations (4.12) and (4.13) numerically and analyze the dynamics depending on the value of a.

We use the Runge-Kutta method of fourth order as well as the predictor corrector algorithm. The spatial derivatives are evaluated using a finite difference scheme of second order or using a fast Fourier transform algorithm depending on the boundary conditions. The choice of the algorithm is made to optimize the convergence and the calculation times (see appendix B for a short description of the algorithm). The calculations are performed for the vector potential $0 < a < 5$ and for the total flux ϕ through the ring ranging from 0 to $50\phi_0$.

5.4.2 The phase slip line

We investigate the flux penetration into the homogeneous ring for two different boundary conditions. In the case of periodic boundary conditions we identify different regimes in accordance with Eq. (5.3). In the small field limit $a < a_{c1}$, the ring is in a stable state and the penetration of the magnetic flux into the ring can only be induced by a very strong noise η in Eq. (4.12). When $a_{c1} < a < a_{c2}$, in agreement with the stability analysis, the phase slip kinetics depend on the external magnetic field. When $\frac{\phi}{\phi_0} < 10$, the kinetics are similar to the 1D case. The transition is characterized by one or more lines in the z-direction where the order parameter decreases to zero (the PSL case [75]). These lines may appear simultaneously or consecutively in time, depending on u, exhibiting a similarity with the 1D case of multiple phase slip centers. As expected, the number of phase slip events is determined by the ratio $\frac{\phi}{\phi_0}$. These PSLs represent the limiting case of kinematic VaV pairs traveling with infinite velocity.

5.4.3 Kinematic vortices

When the flux is increased ($\frac{\phi}{\phi_0} > 10$), the kinematic vortices become clearly distinguishable. In Fig. 5.9(a), we present the time evolution of the average value of the order parameter together with the time-dependence of the number of vortices in the sample. The kinetics are characterized by series of consecutive phase slip events well separated in time (Fig. 5.9(a)). As it was noticed

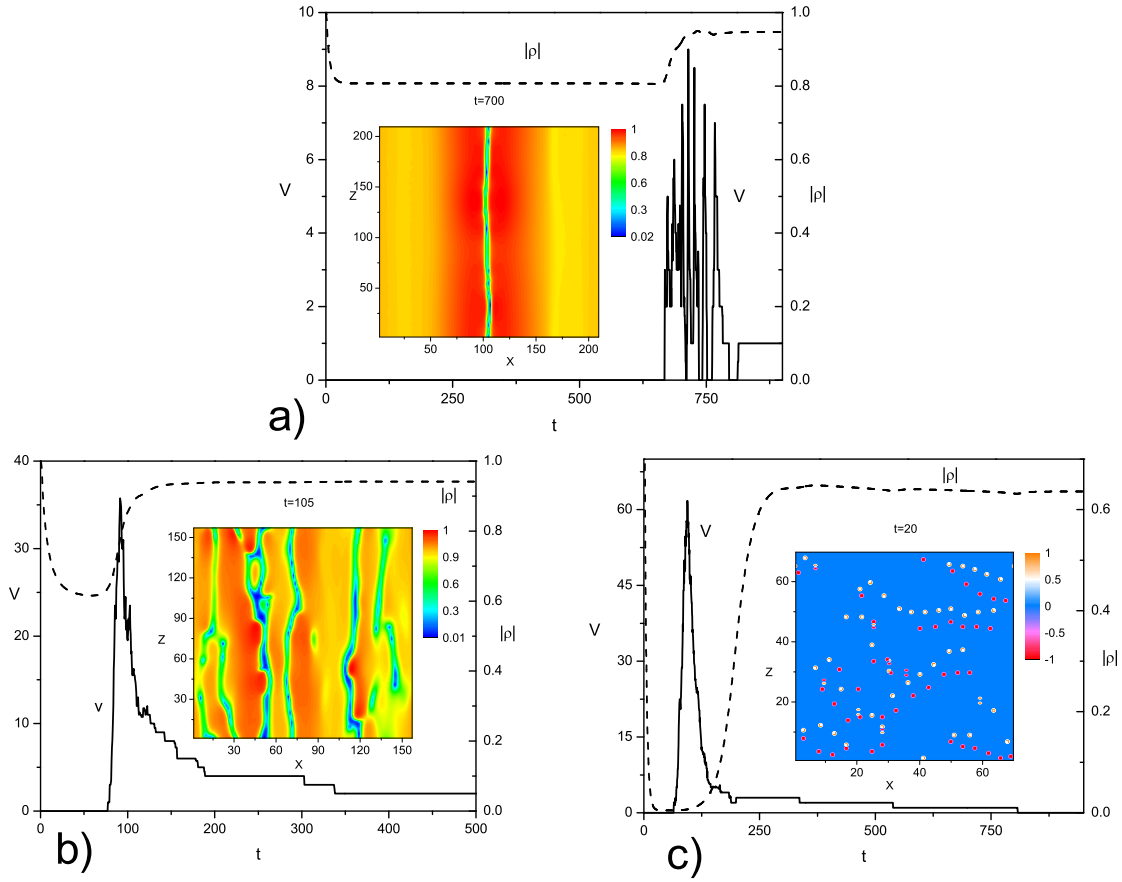

FIGURE 5.9: Total number of vortices v in the system and the sample average value $|\rho|$ of the order parameter as a function of time for $\phi/\phi_0 = 20$ and $a = 0.6$ (a), $a = 0.8$(b) and $a = 1.8$ (c). The insets represent snapshots of the amplitude of order parameter at $t = 700$ (a) and $t = 105$ (b). For the quenched case (c), the snapshot displays the local vorticity at $t = 20$.

[80], few VaV pairs may propagate along the same line at the same time. Phase slip events are produced by kinematic VaV pairs propagating along the same line where the amplitude of order parameter is reduced. Kinematic vortices can propagate in the same direction, one after another or in opposite direction leading to annihilation of VaV pairs and accelerating the dynamics. Contrary to [74], kinematic VaV pairs are formed without any inhomogeneity in the film. At higher fluxes kinematic VaV pairs are randomly created on the line like in the case of a "1D quench". In the x direction, the dynamics remain very ordered with values of the standard deviation of the position (on the x axis) of the vortices $\sqrt{\delta\bar{x}^2}$ approaching 0.5ξ.

5.4.4 Vortex rivers

With the further increase of a, the number of PSLs increases and the kinetics become more stochastic because of the interaction of different PSLs. As a result, straight lines are replaced by vortex rivers which become broader and have finite curvature (Fig. 5.9 (b)). The vortex rivers are comparable to the vortex self-organization discussed in [113] under different boundary conditions.

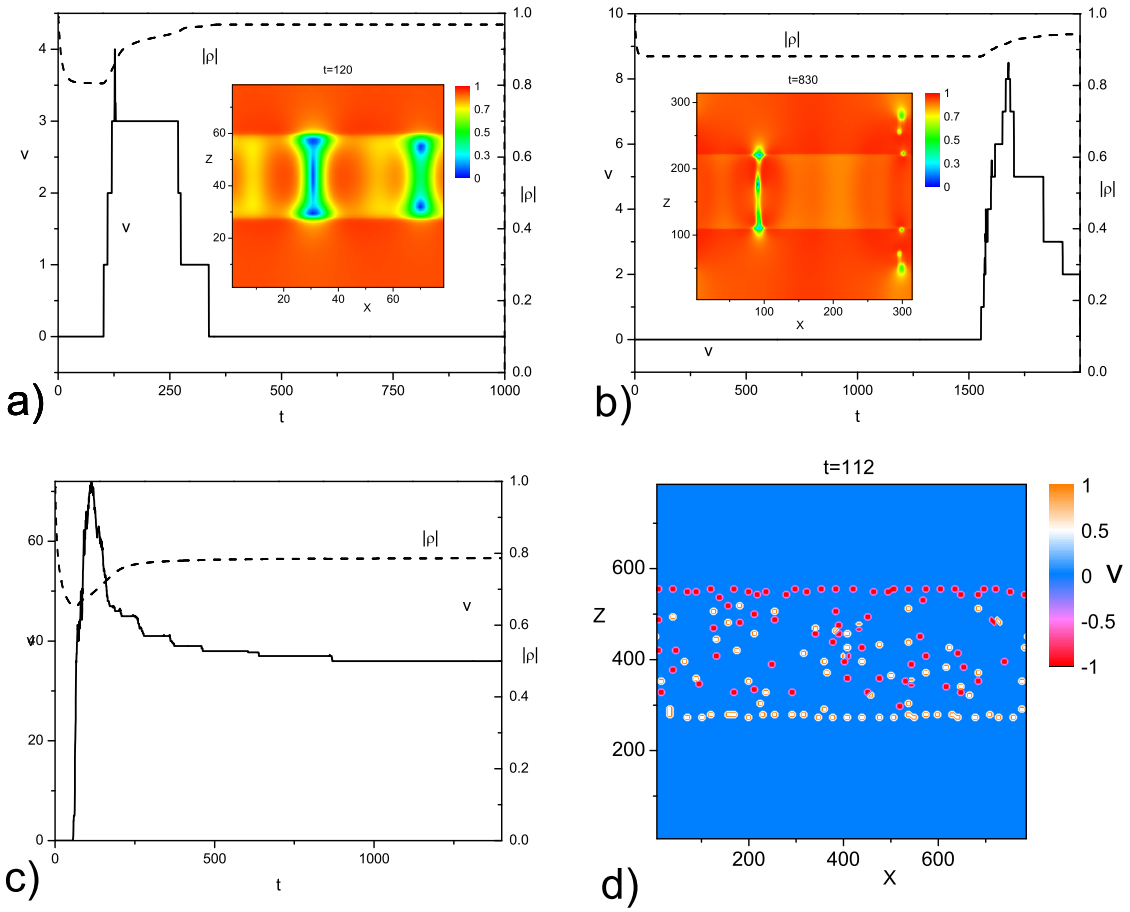

FIGURE 5.10: Total number of vortices v in the system and the sample average value $|\rho|$ of the order parameter as a function of time for $a = 0.4$, $\phi/\phi_0 = 5$ and $b = 4$ (a); $\phi/\phi_0 = 20$ and $b = 2.25$ (b); $\phi/\phi_0 = 50$ and $b = 12.25$ (c). The insets represent snapshots of the amplitude of the order parameter at $t = 120$ (a) ; $t = 830$ (c). For the quasi quenched case (d), the snapshot displays the local vorticity at $t = 112$.

Along one vortex river, few VaV pairs are propagated. The kinetics are determined by the motion of these pairs along the rivers and finally by their annihilation. Importantly, the sample average of order parameter never reaches zero, contrarily to the case of the large field $a > a_{c2}$. The total number of vortices in the beginning of the process is larger than $\frac{\phi}{\phi_0}$ (Fig. 5.9(b)) which is also an indication of the growing importance of chaotic behavior in the dynamics. The values of $\sqrt{\delta\bar{x}^2}$ are also strongly enhanced, reaching $2\pi R/3$. The velocity of vortices along the rivers becomes smaller which is seen from the time-dependence of the vortex number (Fig. 5.9(d)). Nevertheless, the velocity is still high compared to the case when the order parameter has recovered to its equilibrium value.

5.4.5 Kibble-Zurek quench

The last regime $a > a_{c2}$ is presented in Fig. 5.9(c). Here the quench condition is satisfied and the order parameter decreases uniformly until it reaches zero (Fig. 5.9(c)). As a result, the new

phase starts to grow uncorrelated and the vortices are created randomly. The number of vortices is substantially larger than $\frac{\phi}{\phi_0}$. Most of these vortices recombine rapidly. The remaining vortices move slowly through the sample propagating the 2π phase jump. The random dispersion of these vortices is a fingerprint of the KZ mechanism. Indeed, $\sqrt{\delta\bar{x}^2}$ reaches now $2\pi R/2$, which means that vortex distribution is completely random. Another characteristic of the KZ scenario is that the vortices are created while the order parameter is very close to zero and not during the fast growth like in the previous cases as one can see by comparing Fig. 5.9(a) and (b) with Fig. 5.9(c). It is important to notice that the total net vorticity is strictly equal to zero at any time in the case of periodic boundary condition in the z direction.

5.4.6 Finite cylinder

We model a free standing finite cylinder by applying vacuum boundary conditions [2] and find that the kinetics are very similar. When $a_{c1} < a < a_{c2}$ and $\frac{\phi}{\phi_0} < 10$, one or more lines with reduced order parameter are formed. The difference is that the PSLs here have finite curvature, because they start to grow from the edges of the film and finally connect each other. Further increase of the flux, keeping a constant leads to the formation of flux rivers. The most important difference is that not all "rivers" necessarily connect two edges of the film. As a result some of them ended in the middle of the film, leading to the relatively small vorticity. These remaining vortices and antivortices propagate slowly to the edges of the film and kinetics are determined by the slow vortex motion. The dynamics when $a > a_{c2}$ is governed by KZ mechanism, as in the previous case, but the total net vorticity may be finite.

5.4.7 Kelvin-Helmholtz influence

In the case of an inhomogeneous superconductor, the effective coherence length is now z-dependent $\xi(z) = \xi_0\xi_r(z)$ and the cylinder is divided into three regions as seen in Fig. 5.8. We choose $\xi_r = 1/\sqrt{b}$ in the central region and $\xi_r = 1$ in the outer regions. The parameter b is a positive constant and only the middle part of the cylinder may be unstable while the other parts of the film remain in the metastable state. The introduction of z-dependence of the parameters in Eq. (4.12) is designed to enhance the transverse vortex dynamics and allows to demonstrate different mechanisms of vortex formation. As expected, the phase slip dynamics start first in the region with stronger current and is characterized by a and $\frac{\phi}{\phi_0}$.

In the region $a_{c1} < a < a_{c2}$ and small flux $\frac{\phi}{\phi_0} < 10$, the initial stage of the kinetics is similar to kinetics in the homogeneous film. The VaV pairs are not well defined. However, when kinematic VaV pairs approach the low current regions, they become well defined and are slowing down (Fig. 5.10(a)). Therefore vortices are stabilized near the line where the tangential velocity has

discontinuity. These vortices represent another case of KH instability in superconductors. This instability leads to the formation of well defined vortices and governs the kinetics of the phase slip. To the best of our knowledge this is the only instability which allows vortex production in the low flux limit.

When the flux through the ring is large $\frac{\phi}{\phi_0} > 10$, the initial fast dynamics are similar to the dynamics in the homogeneous case until vortices reach the low current regions. Then they become slow and well defined. As it is seen in Fig. 5.10(b), the vortices propagate one after another to the film edge, demonstrating the vortex-vortex attraction even when the order parameter has already recovered.

The further increase of $a > a_{c2}$ leads to the quench in the middle part of the film (Fig. 5.8). During the quench many KZ vortices are created as seen in Fig. 5.10(c) and (d). Most of them annihilate on a very short time scale. The rest of them reach the line separating the region with different currents. The vortices almost stop near this line. Further dynamics are determined by the diffusion of these vortices to the film edges (see Fig. 5.11 and 5.12). When a is large enough, the KH vortices become well defined before the recovery of the order parameter in the middle part of the film and therefore the inhomogeneity suppresses the KZ mechanism in agreement with [111], making kinetics less stochastic.

5.5 Discussion

5.5.1 Phase diagram

We observe different dynamics in the homogeneous case depending on the value of the magnetic field and on the size of the sample. In order to judge between the different dynamics, one needs to look at different facts. The extreme situations are easy to define. For example, the PSL occurs without any vortices. Kinematic vortices, which travel on a single line, have a very small standard variation of their x coordinate $\sqrt{\delta\bar{x}^2}$. However, it is harder to distinguish between the KZ dynamics from scenarios with multiple vortex rivers based on the value of $\sqrt{\delta\bar{x}^2}$ alone. One needs to look at a different criterion to characterize the alignment of the vortices in the rivers because overall, the distribution of the rivers is close to being random. Moreover, KZ mechanism differs from the vortex river evolution because the vortices are created when the order parameter is very close to zero and in a larger number than in the vortex river case, where they are created only when the order parameter is already relaxing. Last one can look at the complete evolution of the order parameter in order to understand the picture.

In order to plot a phase diagram and display the different types of dynamics, we needed to choose an objective criterion. We found out that the stochasticity is a good approach to this problem

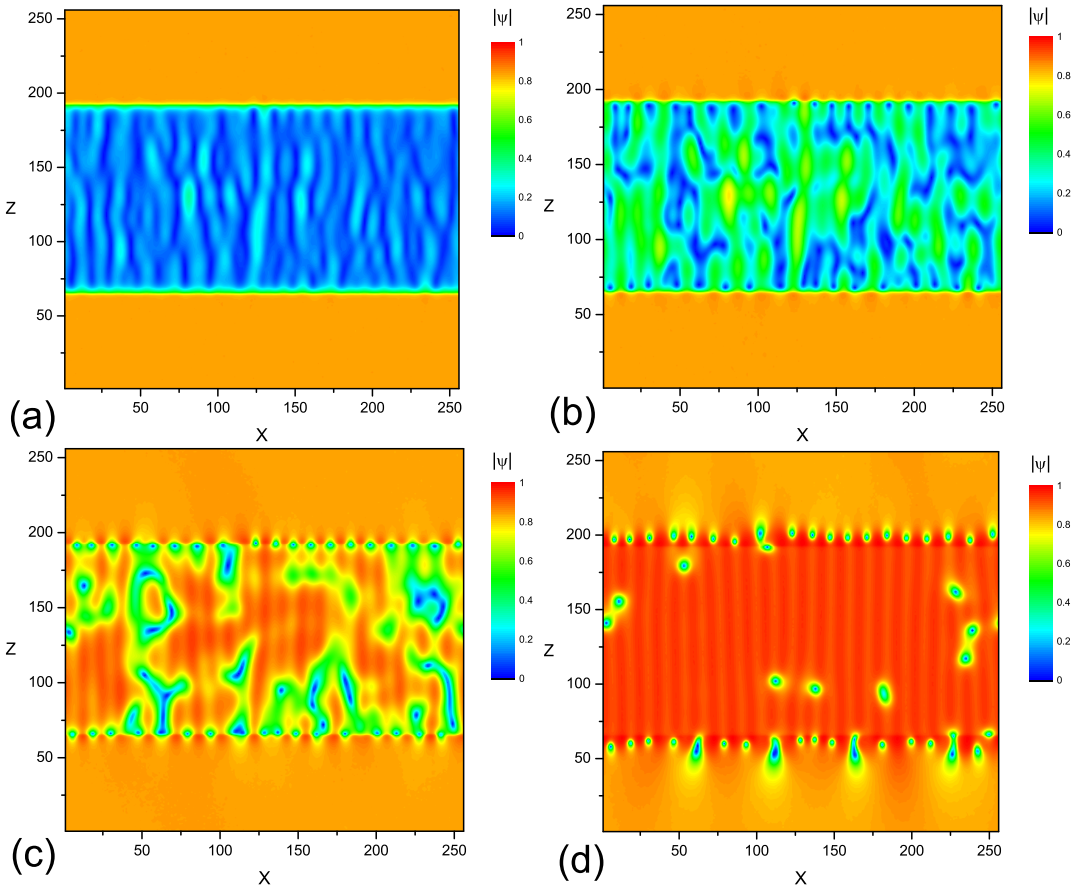

FIGURE 5.11: Evolution of the distribution of the amplitude of the order parameter during a KZ quench in presence of a KH interface. Here $a = 0.4$ $\phi/\phi_0 = 50$ and $b = 12.25$, for t=90 (a), 120 (b), 150 (c) and 210 (d).

and chose the standard deviation of the x coordinate of vortices to define regions where the dynamics are comparable. The normalized standard deviation $\frac{\sqrt{\delta x^2}}{\pi R}$ is shown in Fig. 5.13. The different regions where the standard deviation is similar are separated by lines of constant standard deviation.

- Part 1 of the phase diagram corresponds to the PSL solution. No vortices are present and we define there $\frac{\sqrt{\delta x^2}}{\pi R} = 0$ because the dynamics are very ordered.
- Part 2 ($0 < \frac{\sqrt{\delta x^2}}{\pi R} \leq 0.23$) corresponds to kinematic vortices traveling on a single line.
- Part 3 ($0.23 < \frac{\sqrt{\delta x^2}}{\pi R} < 0.48$) is assigned to multiple vortex rivers: stochasticity is increased by the increasing number of rivers.
- Part 4 ($0.55 < \frac{\sqrt{\delta x^2}}{\pi R}$) corresponds to Kibble-Zurek (KZ) type dynamics which display the highest possible stochasticity.
- Part 5 ($0.48 < \frac{\sqrt{\delta x^2}}{\pi R} \leq 0.55$) represents the region where the standard deviation fails to clearly distinguish between KZ and vortex rivers. In this region, the area with low a corresponds to vortex rivers and should belong to the part 3. Indeed, when the flux is increased

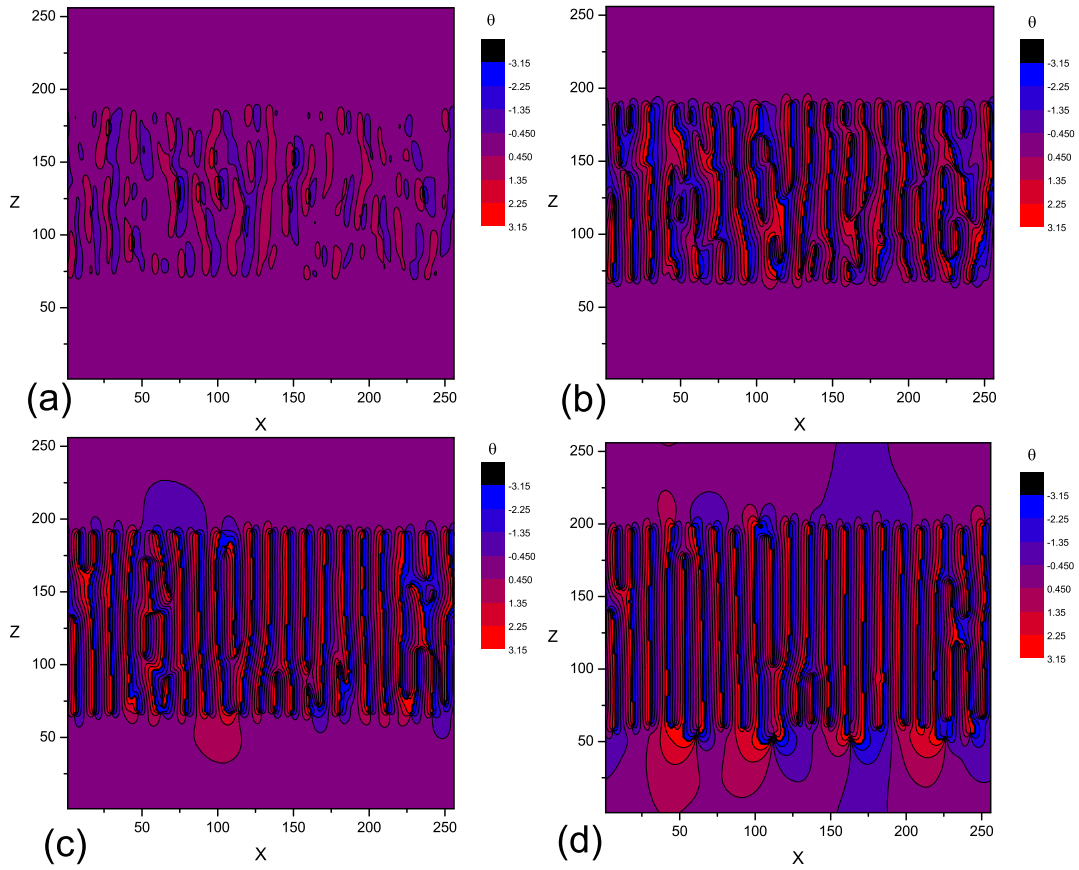

FIGURE 5.12: Evolution of the distribution of the phase of the order parameter during a KZ quench in presence of a KH interface. Here $a = 0.4$ $\phi/\phi_0 = 50$ and $b = 12.25$, for t=90 (a), 120 (b), 150 (c) and 210 (d).

at low a, the number of vortex river increases and the vortices often travel from one river to the other: their position becomes stochastic. On the opposite, at low flux, the area with high a should belong to part 4.

5.5.2 Experimental considerations

Experimentally, observing such dynamics of vortices might be a real challenge because the short characteristic times do not allow the use of instruments with sufficient space resolution. However, recent works [81, 100] showed that freezing the dynamics can characterize both KZ and vortex river scenarios. Another idea is to use time resolved femtosecond optical spectroscopy as proposed in [114]. In section, we will propose yet another geometry that could characterize a KZ quench driven by a laser pump.

As we saw in 1D in section 4.3.3, the role of heating is not important for the proposed geometry of the film. Indeed, the estimate of the heating of the cylinder may be done using Ohm's law. We consider that a part of the cylinder of area $\pi\xi^2$ for the vortex or $2\pi R\xi$ for the PSL, behaves like

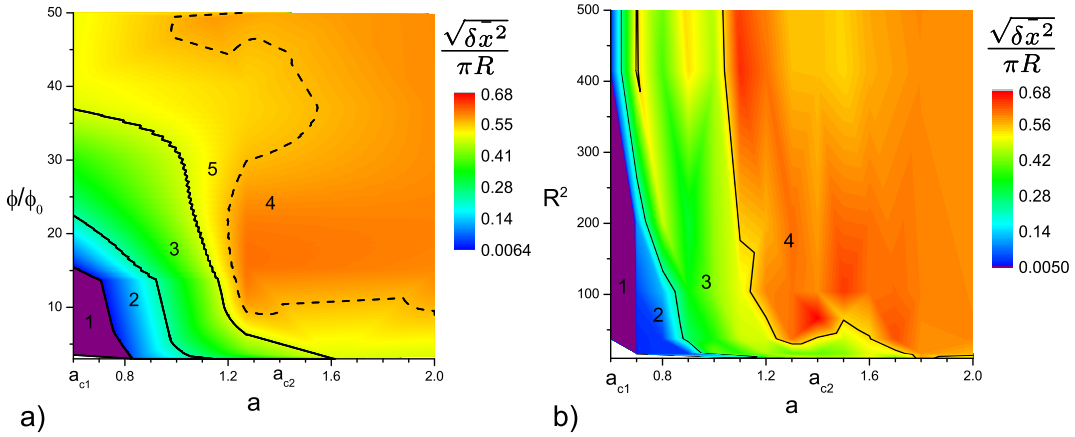

FIGURE 5.13: Phase diagram of the possible evolutions drawn from the normalized standard deviation $\frac{\sqrt{\delta\bar{x}^2}}{\pi R}$ of the x coordinate of the vortices. We chose to define $\frac{\sqrt{\delta\bar{x}^2}}{\pi R} = 0$ when no vortices are present (Part 1). Part 1 corresponds to the PSL, part 2 to the kinematic vortices, part 3 to vortex rivers and part 4 to KZ type dynamics. The part 5 represents a region where the standard deviation is not sufficient to distinguish between the dynamics. The standard deviation is plotted as a function of the vector potential a and of the number of flux quanta (a) or R^2 (b) for $u = 10$. a_{c1} is the critical value under which dynamics are very improbable and a_{c2} is the critical value over which we calculated KZ dynamics would occur.

a normal conductor of conductivity σ_n until its annihilation and sustains a current J_s (in CGS units). The energy dissipated per unit of volume is, as in section 4.3.3:

$$E = \frac{J_s^2}{\sigma_n}\tau_\theta = \frac{\left[\phi_0 a(1-a^2)\right]^2}{16\pi^3\xi^2\lambda_{\text{eff}}^2}. \tag{5.4}$$

This energy is less than a quarter of the condensation energy $\frac{H_{c_2}^2}{16\pi\kappa^2}$. In the case of PSLs and kinematic vortices, when dynamics are fast and the areas behaving as normal conductors are small, the heat will be dissipated along the sample and through the contacts. It will not impact the dynamics. However, in the case of multiple vortex rivers or in the quenched KZ scenario, the total heating will be much larger but can be tackled by modern experimental techniques. Indeed, modern cooling methods are fast enough [100].

5.6 Conclusions of this chapter

In this chapter, we have considered the kinetics of the flux penetration to the 2D ring. Using the knowledge of different mechanisms for the production of vortices, we adapted the different theories to our system where the main parameter is the external magnetic field.

We found out that for small values of the external magnetic vector potential **a**, the kinetics are deterministic and essentially 1D. Increasing the flux ϕ creates kinematic vortices and even leads to a 1D quench along the PSL which is a first step towards stochastic behavior. Further increase

of a leads to the formation of vortex rivers and ultimately to the quench of the sample leading to the stochastic dynamics of KZ vortices. Therefore, we believe that the parameter a is responsible for transversal dynamics while ϕ governs the longitudinal dynamics. This is demonstrated by the PSL at low a and ϕ limit, in comparison to the total quench of the sample for high a and ϕ limit. We used the standard deviation to characterize the different dynamics in a phase diagram but a more sophisticated statistical function could improve our analysis.

Analytical work on the TDGL equations allowed us to define two different critical values for the magnetic vector potential: $a_{c1} = \frac{1}{\sqrt{3}}$ above which the flux can start to penetrate the sample and $a_{c2} = \sqrt{2}$ above which KZ dynamics start to be the leading process. However, as the phase diagram shows, those values and especially a_{c2} are only rough approximations.

Introducing a 2π phase difference in the initial solution and simulating an inhomogeneous film demonstrate that the VaV pairs are a 2D topological analog of phase slip centers but this analogy is not as straightforward as is often believed. Finally, our calculations for a partially quenched film indicate that KH vortices at the interface are strongly predominant.

As we show throughout this chapter, the field of creation of topological defects is vast and many extensions of our results are possible. For instance, the analysis and simulations of the purely KH instability could be done for superconductors. Experiments could be done as well. Comparison with the original derivation and with works in superfluid helium could be very interesting. The KZ context is even richer and one could study the case of a quench of a superconductor by driving the transverse magnetic field above the upper critical field H_{c2}. Moreover, we could as well study in more details the role of the magnetic field and of the induced current on the vortex dynamics during the quench of the superconductor. Last, the original idea of Zurek was to get from such works an insight on the hypothesis made by Kibble for the early creation of the universe, but we will leave that hazardous question to cosmologists.

Chapter 6

New scenarios for ultrafast optical spectroscopy

In this chapter we present preliminary investigations for new experimental setups in ultrafast optical spectroscopy where the heat generated by the laser pulse can no longer be overlooked. We discuss the theoretical model chosen to describe the non-equilibrium situation that we will encounter in such experiments. We present the results of numerical simulations and more specifically the variation of the order parameter in the probe region and we interpret the data in terms of experimentally observable quantities.

6.1 Ultrafast optical spectroscopy

6.1.1 The common setup

In the last two decades, many new experimental techniques have been used to study the superconducting state. The main idea is of course to investigate the new high temperature superconductors in order to get a better understanding of the underlying mechanisms. As such, the time resolved pump probe optical spectroscopy technique has been used in various works with constructive results [115–118]. It is indeed a powerful tool to describe ultrafast phenomena and in particular to study the local superfluid dynamics. The underlying idea is simple: the first laser pulse excites the sample and the second laser pulse is used to measure the optical characteristics. The first pulse, called "pump", excites electron-hole pairs which relax to states around the Fermi energy. This relaxation is made via electron-electron and electron-phonon scattering and results in the

multiplication of quasiparticles. The distribution of quasiparticles might modify the optical characteristics of the material such as the absorbance and the reflectivity. In particular in the case of superconductors, the gap will induce a nonuniform distribution of the quasiparticles which will accumulate near the gap. The second laser pulse, called probe, will detect the change of reflectivity. By changing the delay between pump and probe, one can then obtain the time-dependency of the reflectivity which can be linked to the intrinsic mechanisms after further analysis. Of course, the probe pulse should have a low intensity not to alter the superconducting state. The heating effects of the laser pulse [119] are minimized and can be neglected in most experiments.

6.1.2 New scenarios for high fluences

As we saw in chapter 5, some interesting dynamics like the Kibble-Zurek (KZ) mechanism can happen during the transition between the normal state and the superconducting state. For the particular case of the KZ mechanism, part of the dynamics happen at very short timescales and it seems natural to think about possibilities to use ultrafast optical spectroscopies to characterize such effects. In such an experimental setup, the first laser pulse would completely destroy the superconducting state by breaking the Cooper pairs or simply by bringing the local temperature above the critical temperature T_c. In such a case, the effects of local heating might have an influence on the properties that are probed during the measurements. New techniques need to be developed to investigate such situations. The first possibility is to have the second pulse probing at a different location than the first pump pulse. Such split pump probe technique might be appropriate for configurations where the perturbation of the superconducting state can be transmitted to the probe location without heating effects reaching this area. In particular, in the case of a ring, the current induced by an external magnetic field can act as a vector for the transmission of the dynamics. Another possibility is to use three laser pulses: first a high fluence destruction pulse, a second conventional pump pulse and last the probe pulse.

6.2 Ginzburg-Landau model of laser pulses

For the GL equation, the perturbation corresponding to a laser pulse can be modeled as a modification of a type of local temperature obeying the classical heat diffusion equation. This first approximation is justified for laser pulses of high intensities where the heat diffusion processes can no longer be neglected [119].

6.2.1 The heat diffusion equation

Let us write the heat equation for the temperature T with the dimensionless units adapted to our problem. The spatial coordinate $\mathbf{s} = (x, y, z)$ is written in units of ξ, the time in units of the characteristic relaxation time τ_θ and the diffusion coefficient D is in units of $\frac{\xi^2}{\tau_\theta}$.

$$\frac{\partial T(t, \mathbf{s})}{\partial t} = D\nabla^2 T \tag{6.1}$$

The laser pulses are characterized by an initial temperature profile $T(0, \mathbf{s})$. In this chapter, we consider a ring that is effectively one-dimensional (1D) because its thickness is smaller than the coherence length ξ. For periodic boundary conditions, we use the following solution to the initial value problem: for $-\infty < x < \infty$ and $0 < t < \infty$,

$$T(t, x) = \frac{1}{\sqrt{4\pi D t}} \int_{-\infty}^{\infty} e^{\frac{-(x-w)^2}{4Dt}} T(0, x) dw. \tag{6.2}$$

The initial condition $T(0, \mathbf{r})$ is given by the profile of the laser pulse. Most of the time, we will use a Gaussian profile, which in 1D, is written: $T(0, x) = c_1 e^{-x^2/\lambda_p^2}$, with λ_p^2 being the characteristic width of the pulse.

Using this initial condition yields:

$$T = c_1 \frac{e^{\left(\frac{-x^2}{4Dt+\lambda_p^2}\right)} \lambda_p}{\sqrt{4Dt + \lambda_p^2}}. \tag{6.3}$$

When we want to model consecutive pulses, we simply add the heat generated by the consecutive pulses. Moreover, we take into account the possibility of heat loss by adding a term in the right hand side of equation (6.2) which becomes:

$$\frac{\partial T(t, \mathbf{r})}{\partial t} = D\nabla^2 T - \frac{T(t, \mathbf{r})}{\tau_T}, \tag{6.4}$$

where τ_T is a relaxation time related to the heat losses in the sample: it is related primarily to the temperature gradient with the environment (substrate, contacts, air), but can also include more complex mechanisms. With this modification, the solution (6.3) simply becomes:

$$T = c_1 \frac{e^{\left(\frac{-t}{\tau_T}\right)} e^{\left(\frac{-x^2}{4Dt+\lambda_p^2}\right)} \lambda_p}{\sqrt{4Dt + \lambda_p^2}}. \tag{6.5}$$

6.2.2 Temperature-dependence in the TDGL equations

In order to take into account the variation of temperature during the heating of the sample, we use the fact that in the GL theory, as derived in section 2.4, the expansion coefficient α depends linearly on temperature. Moreover, we neglect the temperature-dependence of the characteristics of the material embedded in the dimensionless units. We therefore write the TDGL equation with α depending on time, as written in section 3.1:

$$u\left(\frac{\partial\psi}{\partial t}+i\Phi\psi\right)=-\alpha_r(t,x)\psi-\psi|\psi|^2-(i\nabla+\mathbf{a})^2\psi+\eta \tag{6.6}$$

$$\nabla^2\Phi=-\nabla\Big[\frac{i}{2}(\psi^*\nabla\psi-\psi\nabla\psi^*)+\mathbf{a}|\psi|^2\Big].$$

The vector potential $\mathbf{a}$ is written in units of $\frac{\phi_0}{2\pi\xi}$ (ϕ_0 is the flux quantum) and the electrostatic potential Φ in units of $\frac{\hbar}{2e\tau_\theta}$, with e being the elementary charge and $\hbar$ the reduced Planck constant. The only dimensionless parameter left in the equation is the ratio $u=\frac{\tau_\rho}{\tau_\theta}$ between the two characteristic times. The Langevin noise η has the same order of magnitude as in section 4.2.2

Knowing that $\alpha\propto\frac{T-T_c}{T_c}$ and using the solution (6.5) found above, we write:

$$\alpha_r(t,x)=-1+\mu\frac{e^{\left(\frac{-t}{\tau_T}\right)}e^{\left(\frac{-x^2}{4Dt+\lambda_p^2}\right)}\lambda_p}{\sqrt{4Dt+\lambda_p^2}} \tag{6.7}$$

with μ being proportional to the pulse intensity.

6.2.3 Limits of the temperature-dependent TDGL

A similar coupling was used in [106] in order to simulate the KZ mechanism in a 2D film. We obtained similar results by simulating a temperature quench of a 2D sample as well: as in section 5.4, we obtained stochastic creation of vortices and antivortices and their rapid recombination. However, if the coupling of TDGL with the heat equation seems to give a good qualitative picture of the dynamics, the strict validity might be more questionable. Indeed, as discussed in section 2.4, the TDGL are valid only in a close vicinity to T_c. The microscopic derivation also does not take into account a variation of temperature and the relaxation rates are strongly temperature-dependent (as might be other characteristics of the materials). Last, the generalized TDGL equations described in section 2.4 and in [37] might be more appropriate further away from T_c. However, as we are doing a preliminary investigation with no quantitative conclusions as far as the heating effects are concerned and since the characteristic time of variation of temperature is slower than the relaxation rate of the order parameter, we believe that the use of these equations is appropriate.

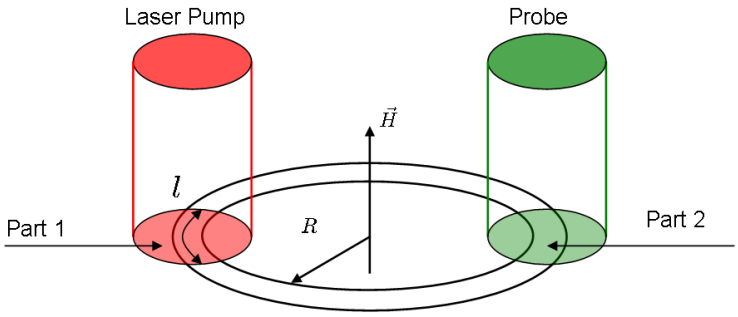

FIGURE 6.1: Geometry of the proposed setup for split pump probe experiments.

6.3 The split pump probe in a 1D ring

We investigate the possibility of a novel kind of optical pump probe spectroscopy where the two laser pulses are focused on different areas of the sample. The response to the destruction of the superconducting state in a large part of a mesoscopic ring is studied numerically.

With modern lasers delivering pulses in the femtosecond regime, one can study the ultrafast response in superconductors and try to get a better understanding of the dynamics linked to the superconducting gap. However, one needs to take into account local effects due to the intensity of the pump pulses and in particular, the local heating and the change in the local carrier concentration. These effects can be minimized and it is generally accepted that they do not threaten the general validity of such measurements, at least for low fluences.

Nevertheless, it is possible to completely get rid of these parasite effects by modifying the original setup which could be very useful for studies at high fluences. The idea is to apply the pump and probe pulses at two different places as seen in Fig. 6.1. Indeed, in the case of a ring, the modification of the state in one half of the ring directly affects the state in the other half of the ring due to the coherence of the superconducting state. Using a magnetic field to induce a current in the ring can also help to spread the dynamics along the whole ring. Such a setup should enable experimentalists to apply pump pulses with high fluences without the usual drawbacks. However, the geometry might be more complex to realize and the dynamics involved at the probe will not necessarily be large enough to be detected. This work therefore constitutes a preliminary investigation to determine whether this setup would be relevant.

6.3.1 The relaxation process

As studied in section 3.2, the stable state will depend on the applied magnetic field. When the initial state is unstable, the order parameter will undergo one or more resistive phase slip events. For the proposed setup, we believe that the presence of magnetic field is important in order to

trigger interesting dynamics. Indeed, we might need the presence of a superconducting current to transmit the dynamics from one side to the other side of the ring. We will study the influence of the induced current in the forthcoming section.

The simplest way to model the laser pump pulse is to consider that the order parameter is completely destroyed in the pump region. We thus start from a solution where the superconducting state has been destroyed on a partial length l of the ring, where L is the total length of the ring:

$$\begin{cases} \psi(x, t=0) = & 0 & \text{, for } 0 < x < l\text{: part 1} \\ \psi(x, t=0) = & \sqrt{1-a^2} & \text{, for } l < x < L\text{: part 2.} \end{cases} \tag{6.8}$$

According to the stability condition found in section 3.3.2.2 and in [40, 41], we can also prevent phase slip phenomena from happening by fixing the magnetic flux to one half of the flux quantum. Here we want to observe the simple dynamics of relaxation from the TDGL equations without taking into account the coupling with the heat equation.

6.3.2 Results

Starting from the initial state (6.8), we study the recovery of the ring to the stable state. When we destroy superconductivity, we immediately create a voltage in the ring caused by the normal region and therefore a charge imbalance and resistivity. We can describe two mechanisms that happen in the simple framework of the phenomenological theory.

Mechanism A: In the superconducting part (part 2), the density of superconducting electrons stays constant, but they are slowed down by the voltage: we observe a decrease of the total current. In this situation, we consider that we have a very low normal current appearing in that region. In the part where the superconductivity has been destroyed (part 1), we observe a strong normal current going in the same direction as the superconducting current before the pump pulse. The Cooper pairs are broken but the electrons continue to move in the same direction. This normal current is progressively reduced as the superconducting state is recovered: the normal electrons are accelerated by the voltage and reduce the charge imbalance and the voltage. However, if in part 1 the superconducting current gets too low and if in part 2 the total current gets too high, we have an inversion of the voltage and the relaxation will be similar to a damped oscillator.

Last, as the voltage is reduced, the normal current disappears and the superconducting current and density will grow in part 1, which brings more superconducting electrons in part 2 where the density of the superconducting electrons will reach a maximum before relaxing to the stable state. During that phase, the total current increases and reaches its original value as well.

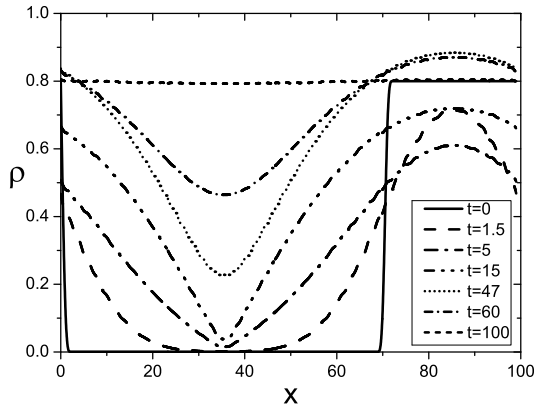

FIGURE 6.2: Distribution of the order parameter amplitude ρ at different times, for $l/L = 70\%$ and $a = 0.6$

Mechanism B: We can also imagine that in part 2, the density of the superconducting electrons is reduced i.e. Cooper pairs are broken in that part as well due to their deceleration induced by the voltage. Therefore, a strong normal current will also appear in part 2 with an opposite direction to the superconducting current. As a result, the total current will be reduced. In part 1, the situation is similar to the mechanism A. Again, if the mechanism is too strong, we will observe an inversion of the voltage and damped oscillations.

To summarize, in part 2, the mechanism A induces an increase of the amplitude of the order parameter before relaxing to the stable state, whereas the mechanism B results in a decrease of the amplitude before relaxation.

We simulate the relaxation process with different values for the vector potential a and for the size l of the part 1. The TDGL equations are solved numerically using Runge-Kutta method of the fourth order for time derivatives and fast Fourier transform for the space derivatives (see appendix B).

Qualitatively, we observe that the mechanisms A and B are in fact mixed as seen in Fig. 6.2. The mechanism A is dominant for small l and low a and the mechanism B is dominant for large l and high a like shown in Fig. 6.3(a) and 6.3(b). We believe that the competition between the two processes is the cause of the two-step increase of the superfluid density as shown in Fig. 6.3(a): for $l/L = 50\%$, the amplitude starts to increase and then stalls (or even decreases), before increasing again. As we expected, the variations of the order parameter in the part 2 are stronger when a is larger as seen in Fig. 6.4. Indeed, the superconducting current greatly contributes to spread the dynamics from one part of the ring to the other part as one can understand from the preceding description of the mechanisms.

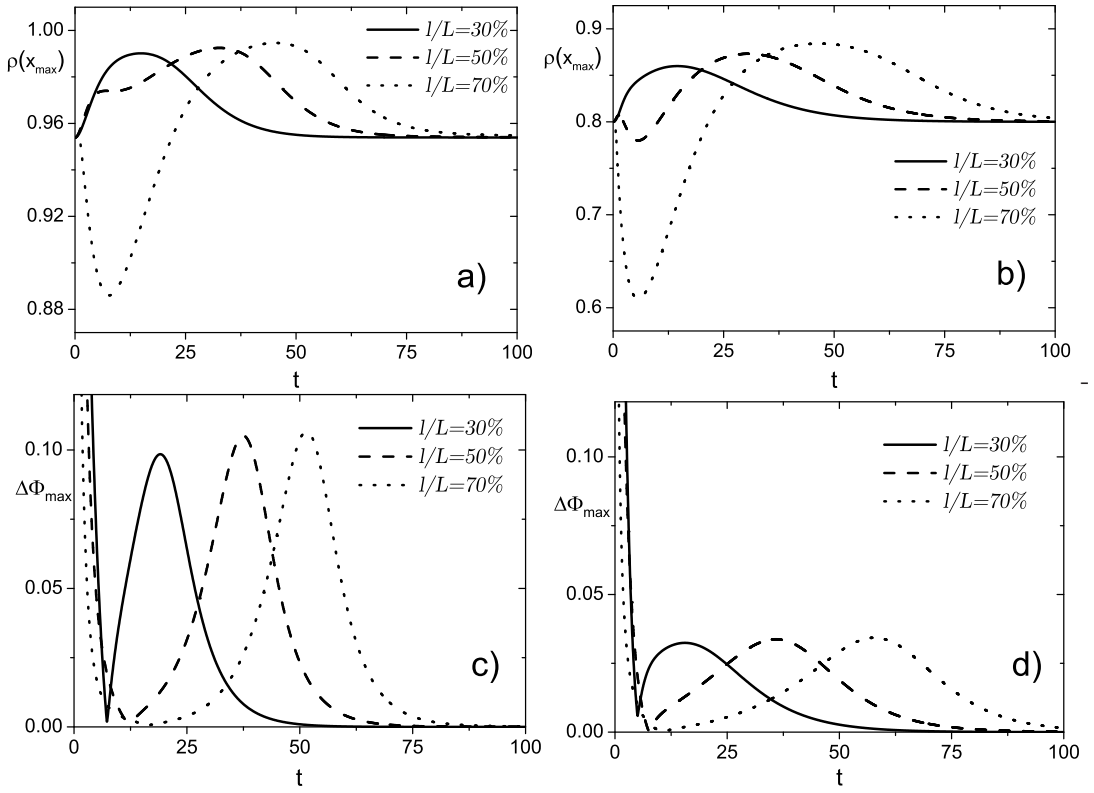

FIGURE 6.3: Evolution of the order parameter amplitude ρ taken at the location x_{max}, where the amplitude reaches its maximum for different values of the perturbed area l/L and $a = 0.3$ (a) or $a = 0.6$ (b) and the corresponding maximum voltage $\Delta\Phi_{max}$ (c) and (d). The larger l/L, the greater will be the influence of the process B. With $l/L = 50\%$ one can clearly see the competition between both processes.

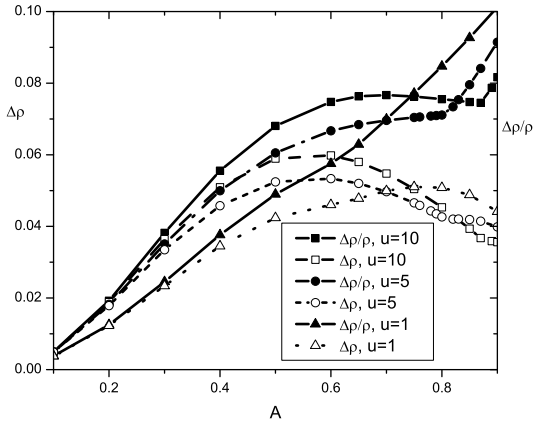

FIGURE 6.4: Maximum variation of the order parameter amplitude $\Delta\rho$ and $\Delta\rho/\rho$ depending on the vector potential a for different values of u.

6.3.3 Discussion

Quantitatively, we can define a maximum of three different relaxation times to characterize the dynamics in the probing region: the time τ_{min} to the minimum of ρ in part 2, the time τ_{max} to the maximum of ρ in part 2 and the time τ_r of the total recovery. Different predictions have been made for recombination times in diverse situations [117]. In our case, in order to predict relaxation times for different materials, we need to have their characteristics which are embedded in the dimensionless variables. Indeed, the time scale is determined by $\tau_\theta = \frac{4\pi\lambda_{\text{eff}}^2\sigma_n}{c^2}$. For the case of NbN we evaluate $\tau_\theta \approx 1$ ps and thus $\tau_{min} \approx 10$ ps $< \tau_{max} \approx 25$ ps $< \tau_r \approx 100$ ps. We believe those values to be representative for a wide range of superconductors. The time range of these processes should therefore be reachable with modern femtosecond pulse lasers.

We also need to compare these values with the characteristic time of the self inductance of the ring. Indeed, as we put part of the ring in the normal state, one needs to evaluate the effects of classical electromagnetism. In our case, we can estimate the characteristic time of the inductance $\tau_L = \frac{4\pi d^2\sigma_n}{c^2}$. Therefore, if the condition that was assumed for the ring $d \ll \lambda_{\text{eff}}$ is true (in other words, if the thickness d is small), the self inductance of the ring can be neglected.

The problem of the strength of the effect in the superconducting phase still needs to be solved. According to a derivation of the Mattis-Bardeen [120] formula in [118] we have:

$$\Delta R_s \propto \left(\frac{\Delta_T}{\hbar\omega}\right)^2 \log\left(\frac{3.3\hbar\omega}{e\Delta_T}\right), \tag{6.9}$$

where ΔR_s is the relative change in reflectivity, $\hbar\omega$ is the photon energy and Δ_T is the temperature-dependent gap.

In the superconducting regime, the superconducting gap is proportional to the amplitude of the order parameter and therefore, the variation of C_s are comparable to the variation of the order parameter. As seen in Fig. 6.3(a) and 6.3(b), we have $\Delta_r\rho \approx 10\% \propto \Delta_r\Delta_T$, where $\Delta_r\rho$ are Δ_r Δ_T the relative variation of ρ and of the gap Δ_T. According to (6.9), the changes in the gap in part 2 induce modifications in the optical properties which are measurable by the probe laser pulse.

The induced voltage is of the order of a few millivolts as seen in Fig. 6.3(c) and 6.3(d) and should be measurable as well. However, it is slightly more complicated to find the right spot to measure the voltage as the extrema of the electrostatic potential are shifting during the relaxation process.

6.3.4 The quench dynamics in 1D

At high fluences, a laser pulse can completely destroy the superconducting phase and with a sufficiently fast cooling, the quench of the sample should lead to the Kibble-Zurek mechanism described in chapter 5. In 1D, the KZ mechanism works in the same way as for 2D. The topological defects are simply 1D jumps of 2π in the phase of the order parameter ψ. The number of those jumps will scale with the characteristic time of the quench. For the geometry of the ring proposed above (see Fig. 6.1), the simplest model is to consider that the laser pulse are increasing the temperature of the sample locally and to use the TDGL equations coupled with the heat equation as written in section 6.2.

For the 1D ring, we simulate the coupled equations of section 6.2 and obtain the expected stochastic creation of topological defects in the part 1 of the ring as seen in Fig. 6.6 and Fig. 6.8. The dynamics now depend on the speed of the temperature cooldown and on the speed of the relaxation of the order parameter. However, to stay close enough to the validity of the TDGL equation, the relaxation of the order parameter should be fast compared to the temperature change below T_c.

The importance of the heat diffusion depends on the material used for the experiments as well as on the intensity of the pulse. We simulated different behaviors using the coupled equations and found out that the effects of the KZ mechanism are difficult to distinguish from the simple relaxation of the order parameter if the relaxation rates involved are comparable. In Fig. 6.5, we made a simulation where the pulse is modeled with a step profile and for very low magnetic potential a and with negligible effect from diffusion. In this case, the effects in part 2 are absent as the order parameter grows in domains that are uncorrelated not only between themselves as described in section 5.3, but they are also uncorrelated with the part 2 of the ring. However, when the external magnetic field is increased, similarly as shown in Fig. 6.4, the suppression of the order parameter will start affecting the part 2 of the ring and a finer analysis is needed to distinguish the cases where topological defects are created.

Moreover, when the diffusion is taking place, it becomes difficult to tell what part of the dynamics is caused by the diffusion and what part is caused by the superconducting current. In Fig. 6.7, we see the diffusion process coupled with the dynamics of the order parameter when the pulse is modeled by the Gaussian profile of section 6.2. In general, the difference in the behavior of the part 2 between the simple relaxation and with the KZ dynamics can be seen in simulations or by predicting the different relaxation rates but it will be difficult to observe experimentally.

As mentioned in [93], the ring geometry is very interesting for simulations of KZ dynamics in superconductors because the number of topological defects can be measured directly through the flux of the ring and any trapped flux can be distinguished as well. Indeed, in many simulations, the final state of the superconductor was one phase slip away from the equilibrium solution according

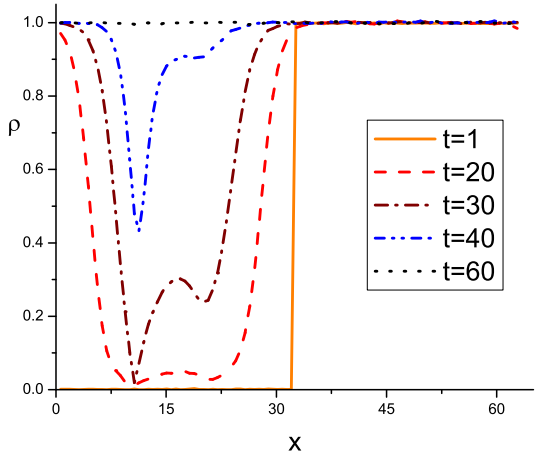

FIGURE 6.5: Distribution of the order parameter amplitude ρ at different times, for $l/L = 50\%$ and $a = 0.03$ during a temperature quench triggered by a laser pulse in part 1 of the ring.

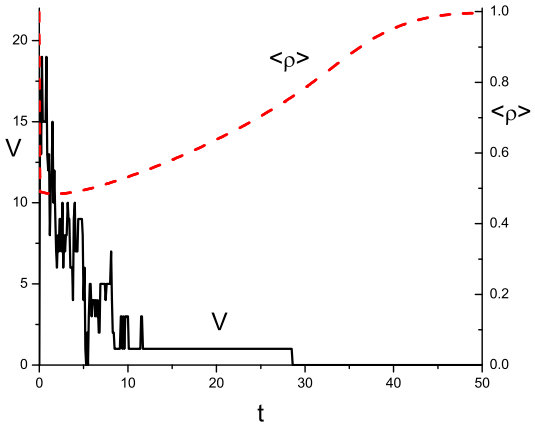

FIGURE 6.6: Total number of topological defects v in the system and the sample average value $< \rho >$ of the order parameter as a function of time.

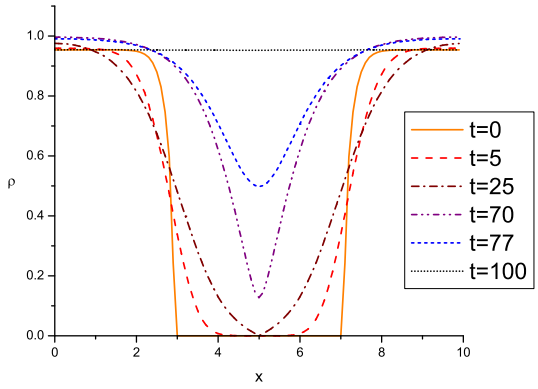

FIGURE 6.7: Distribution of the order parameter amplitude ρ at different times, for $a = 0.3$ and a temperature quench triggered by a laser pulse with a Gaussian profile on the center of the ring and with effects of heat diffusion. Here the laser pulse hits the center of the sample.

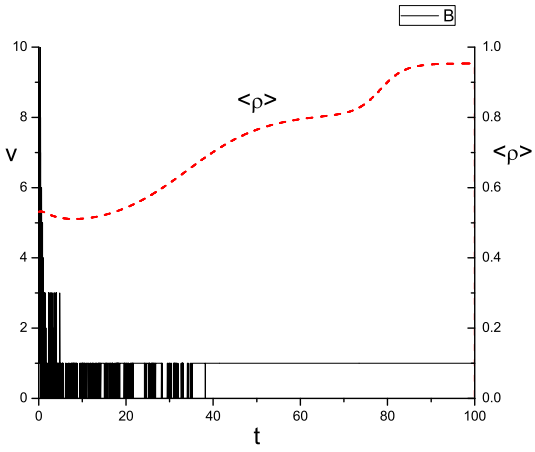

FIGURE 6.8: Total number of topological defects v in the system and the sample average value $< \rho >$ of the order parameter as a function of time for $a = 0.3$ and a temperature quench triggered by a laser pulse with a Gaussian profile on the center of the ring and with effects of heat diffusion.

to the stability condition (4.18). This trapped flux could be easily measured using a SQUID (see section 2.3) as was done for common phase slips [55] and remains the best way to characterize the KZ mechanism from the experimental point of view.

6.4 Conclusions of this chapter

We described a new possibility of femtosecond optical spectroscopy where the pump and the probe laser pulses are applied at different areas of a superconducting ring. This setup allows

the study of pure superconducting dynamics even for high values of the intensity of the pump pulse. As a preliminary investigation, we simulated the setup using the TDGL equations with periodic boundary conditions. We described two different mechanisms that can compete during the relaxation process. The results show three different relaxation times that can be measured in the femtosecond range. The associated variation of the amplitude of the order parameter should be measurable as well as the voltage. We observed the dynamics by simulating the relaxation of the order parameter as well as by coupling the heat equation to the TDGL equations as a first approximation. When the intensity of the pulses destroy the superconducting state and induce a quench, the global dynamics are similar with a smaller effect on the probe region, but by measuring the flux of the ring, one should be able to characterize the KZ mechanism.

Chapter 7

General conclusion

In this thesis, we have analyzed different transitions between the stationary solutions of the TDGL equations. We found out that increasing the magnetic field can drive the superconductor out of equilibrium and we studied the different relaxations towards the final state. In the 1D ring, the phase of the order parameter can jump by 2π at different phase slip centers where the order parameter is reduced. Our study of the multiple phase slips case revealed the importance of the parameter u. While $u \ll 1$ is favoring simultaneous phase slips, cases with $u \gg 1$ are very likely to lead to relaxations with consecutive phase slips. Therefore, $u \gg 1$ is often a necessary condition for the relaxation to the ground state. In wires, it should be very interesting to link the current-voltage characteristics to the number of phase slip centers and even to predict their configuration and evolution from consecutive to simultaneous.

In the 2D case of a cylinder, the dynamics show very different aspects and we found out that the magnetic field made the transition evolve from a very ordered process to the stochastic dynamics governed by the Kibble-Zurek mechanism. Indeed, we predicted analytically and simulated the phase slip line, then the kinematic vortices, vortex rivers and last the Kibble-Zurek vortices. For an inhomogeneous material, we observed a reduction of the stochasticity driven by the Kelvin-Helmholtz instability. Although these different processes are all known for a long time, the Kibble-Zurek mechanism and the Kelvin-Helmholtz instability have not been previously analyzed thoroughly in superconductors and many extensions of this work are possible.

Last, we proposed new scenarios for ultrafast spectroscopy where high intensity pulses are used. We describe the split pump probe setup in a 1D ring, where the laser pump pulse excites the sample at a different location than the laser probe pulse is applied to measure the changes in optical properties. We first considered the simple relaxation of the order parameter and found out that a strong suppression of the order parameter in the pump region would be measurable by its effect on the remote probe location. Indeed, when a superconducting current runs in the ring, the

variations of the amplitude of the order parameter as well as of the voltage are strong enough to be detected. We coupled the heat equation to the TDGL to investigate a quench triggered by a laser pulse. If the dynamics are similar, the possibility to trap a magnetic flux resulting from the stochastic creation of topological defects remains the best way to differentiate simple relaxation from the Kibble-Zurek mechanism.

Appendix A

On the CGS units system

The centimeter-gram-second system (CGS) is a system of physical units with several variations for the electromagnetic quantities: electrostatic units (ESU), electromagnetic units (EMU) and Gaussian CGS units. In this thesis, we use the Gaussian CGS units that we describe shortly in this appendix.

While for most units the difference between CGS and SI are just powers of ten, the differences in electromagnetic units are more complex: formulas for physical laws of electromagnetism are adjusted depending on what system of units one uses.

The use of the CGS system simplifies theoretical calculations but it has the disadvantage that the units are hard to define by experiments. SI on the other hand starts with a unit of current, the ampere which is easy to determine by experiments, but which requires that the constants in the electromagnetic equations take a more complicated form. A key virtue of the Gaussian CGS system is that electric and magnetic fields have the same units and the only dimensional constant appearing in the equations is c, the speed of light.

The quantities used in mechanics can be converted as follows:

Quantity	SI unit (abbreviation)	CGS unit (abbreviation)	Equivalence in SI units
length	meter(m)	centimeter(cm)	1 cm= 10^{-2} m
mass	kilogram(kg)	gram(g)	1 g= 10^{-3} kg
time	second(s)	second	1 s= 1 s
velocity	meter per second	centimeter per second	1 $\frac{\text{cm}}{\text{s}} = 10^{-2}$ m/s
force	Newton(N)	dyne(dyn)	1 dyn= 1$\frac{\text{g}\cdot\text{cm}}{\text{s}^2} = 10^{-5}$ N
energy	Joule(J)	erg	1 erg= 1$\frac{\text{g}\cdot\text{cm}^2}{\text{s}^2} = 10^{-7}$ J
power	Watt(W)	erg per second	1 erg$\cdot$s^{-1} = 1 $\frac{\text{g}\cdot\text{cm}^2}{\text{s}^3} = 10^{-7}$ W
pressure	Pascal(Pa)	barye(Ba)	1 Ba= 1 $\frac{\text{g}}{\text{cm}\cdot\text{s}^2} = 10^{-1}$ Pa

The quantities used in electromagnetism can be converted using speed of light $c = 29,979,245,800 \approx 3 \cdot 10^{10}$:

Quantity	SI unit (abbreviation)	Gaussian CGS unit (abbreviation)	Equivalence in SI units
electric charge	Coulomb(C)	franklin(Fr)	1 Fr= $10c^{-1}$ C
electric current	Ampere(A)	franklin per second	1 Fr$\cdot$s^{-1} = $10c^{-1}$ A
electric potential voltage	Volt(V)	statVolt(statV)	1 statV= $10^{-8}c$ V
magnetic induction	Tesla(T)	Gauss(G)	1 G= 10^{-4} T
magnetic field strength	A/m	Oersted (Oe)	1 Oe= $\frac{10^3}{4\pi}$ A/m
magnetic flux	Weber(Wb)	(G$\cdot$cm^2)	1 G$\cdot$cm^2 = 10^{-8} Wb
resistance	Ohm(Ω)	(s/cm)	1 s/cm= $10^{-9}c^2$ Ω
capacitance	Farad(F)	centimeter(cm)	1 F= $10^9 c^{-2}$ cm
inductance	Henry(H)	(cm^{-1}s^2)	1 cm^{-1}s^2 = $10^{-9}c^{-2}$ H

Appendix B

Choices in the code and algorithms

In this thesis, we solve the simple version of the dimensionless time-dependent Ginzburg-Landau (TDGL) equations as written in section 3.1. The most general form of the equations that we solved is:

$$u\left(\frac{\partial\psi}{\partial t}+i\Phi\psi\right)=-\alpha_r\psi-\psi|\psi|^2-(i\nabla+\mathbf{a})^2\psi+\eta \tag{B.1}$$

$$\nabla^2\Phi=-\nabla\left[\frac{i}{2}(\psi^*\nabla\psi-\psi\nabla\psi^*)+\mathbf{a}|\psi|^2\right], \tag{B.2}$$

where ψ is the order parameter, Φ is the electrostatic potential, $\mathbf{a}$ is the constant vector potential, u is constant parameter, α_r is an external variable that can vary with time and position and η is a Langevin noise.

The code was written in Fortran 95 using some routines from the NAG libraries. The time integration is made using a Runge-Kutta (RK) method of order 4 or a predictor corrector method and the spatial derivative are calculated either with Fourier transform, or with a second order finite difference scheme.

B.1 Time integration

Let us first look at the time integration in the first TDGL equation (B.1). The general form of such an equation is

$$\frac{d\psi(t,x)}{dt}=f(t,\psi), \tag{B.3}$$

with the initial condition

$$\psi(t_0, x) = \psi_0(x), \tag{B.4}$$

where f is a function defined by the problem to solve. In our case, the function f is:

$$f(t, \psi) = -\phi(t, x)\psi(t, x) + \frac{1}{u}\left[-\alpha_r\psi - \psi|\psi|^2 - (i\nabla + \mathbf{a})^2\psi + \eta\right]. \tag{B.5}$$

B.1.1 The Runge-Kutta method

The basis of the Runge-Kutta method is the Euler method. We solve the equations in the time interval $[t_0, t_{\text{end}}]$ that we descriptive with a time step τ_s: $t_n = n\tau_s$, where n is an integer. The calculation will be made such as if t is in $[t_0+n\tau_s, t_0+(n+1)\tau_s]$, we write $\psi(t, x) \approx \psi(t_0+n\tau_s, x) = \psi(t_n, x) \approx \psi_n(x)$

The Euler method makes the following linear approximation:

$$\psi_{n+1} = \psi_n + \tau_s f(t_n, \psi_n). \tag{B.6}$$

The Runge-Kutta is based on an approximation that takes the same linear form as the Euler method for the first order, but that is more accurate at higher orders. Instead of using only one additional point to calculate the slope a Runge-Kutta of order p will use p points and will have the accuracy $\psi_n - \psi(t_0 + n\tau_s) = O(\tau_s^{p+1})$. The algorithm is the following:

$$\begin{aligned}
k_1 &= \tau_s f(t_n, \psi_n) \\
k_2 &= \tau_s f\left(t_n + c_2\tau_s, \psi_n + a_{21}k_1\right) \\
k_3 &= \tau_s f\left(t_n + c_3\tau_s, \psi_n + a_{31}k_1 + a_{32}k_2\right) \\
&... \\
k_p &= \tau_p f\left(t_n + c_p\tau_s, \psi_n + a_{s1}k_1 + ... + a_{p,p-1}k_{p-1}\right) \\
\psi_{n+1} &= \psi_n + b_1k_1 + ... + b_pk_p.
\end{aligned}$$

The coefficients a_{kp-1}, b_k and c_p, depend on the method chosen: at higher orders, different sets of coefficients are possible. In our simulations, we mostly used the Runge-Kutta method of fourth

order defined by:

$$\begin{aligned} k_1 &= \tau_s f(t_n, \psi_n) \\ k_2 &= \tau_s f\left(t_n + \frac{\tau_s}{2}, \psi_n + \frac{k_1}{2}\right) \\ k_3 &= \tau_s f\left(t_n + \frac{\tau_s}{2}, \psi_n + \frac{k_2}{2}\right) \\ k_4 &= \tau_s f\left(t_n + \tau_s, \psi_n + k_3\right) \\ \psi_{n+1} &= \psi_n + \frac{k_1}{6} + \frac{k_2}{3} + \frac{k_3}{3} + \frac{k_4}{6}. \end{aligned}$$

B.1.2 The predictor corrector method

The Runge-Kutta uses intermediate points or steps to obtain an accurate approximation. However, it does not reuse the information contained by the steps that have been already calculated. The idea of linear multistep method like the Adams method is to use the those previous steps: the principle again converges with the Euler method for the first order. The best accuracy is found for implicit formulas but the calculations take a long time.

The predictor corrector takes the benefit of the accuracy of the implicit formula but with shorter calculation times. The idea is to make a less accurate first (explicit) prediction of the quantity to calculate and to correct this result at the next step to obtain a higher accuracy which is almost as accurate as using the implicit formula from the beginning. Different versions exits but the most common is to predict, evaluate, correct and evaluate once again (PECE).

In some of our simulations, we used the predictor corrector based on the Adams method of fourth order:

$$\begin{aligned} \psi^P_{n+1} &= \psi_n + \frac{\tau_s}{24}(55f(t_n, \psi_n) - 59f(t_{n-1}, \psi_{n-1}) + 37f(t_{n-2}, \psi_{n-2}) - 9f(t_{n-3}, \psi_{n-3})) \\ \psi^C_{n+1} &= \psi^P_{n+1} - \frac{251}{720}(\psi_n - \psi^P_n) \\ \psi_{n+1} &= \psi_n + \frac{\tau_s}{24}(9f(t_{n+1}, \psi^C_{n+1}) + 19f(t_n, \psi_n) - 5f(t_{n-1}, \psi_{n-1}) + f(t_{n-2}, \psi_{n-2})). \end{aligned}$$

In this description, ψ^P_n is the predicted value, ψ^C_n is the corrected value and ψ_n is the (final) evaluated value for the step n.

B.1.3 Potential during the spatial integration

The variations of the potential Φ and α_r being slow compared to those of the order parameter, we made the calculus with the same values for ϕ and α_r during the intermediate steps of the

Runge-Kutta method and we did not predict and correct those values in the predictor corrector method.

B.2 The spatial derivatives

B.2.1 Finite differences and Fourier transforms

Let us now describe the algorithm we chose to calculate the spatial derivatives and to solve the Poisson equation (B.2). When dealing with a discrete problem, using the value $ik\hat{\psi}(k)$ to approximate the Fourier transform of the derivative of ψ is only a rough approximation. We can refine this evaluation by writing the finite difference for spatial derivative to the second order, with h as the spatial step:

$$\frac{d\psi_p}{dx} = \frac{\psi_{p+1} - \psi_{p-1}}{2h}.$$

The discretization is written with the same notation as was done previously for the time integration as it is not ambiguous here. Writing Fourier transform from a sequence of n values we have:

$$\left(\frac{\hat{d\psi}}{dx}\right)_k = \frac{1}{2h\sqrt{n}} \sum_{j=0}^{n-1} (\psi_{j+1} - \psi_{j-1}) e^{-i\frac{2\pi jk}{n}}.$$

After a change of variable on both sides, it yields

$$\left(\frac{\hat{d\psi}}{dx}\right)_k = \frac{1}{2h}\hat{\psi}\left(e^{i\frac{2k\pi}{n}} - e^{-i\frac{2k\pi}{n}}\right) = \frac{i}{h}\hat{\psi}\sin\left(\frac{2k\pi}{n}\right). \tag{B.7}$$

Taking inverse Fourier transform of the last quantity will now give a good evaluation of the derivatives.

B.2.2 Solving the Poisson equation

To solve the TDGL equations, we must also calculate the potential Φ at each step and therefore solve the equation (B.2).

Using the definition of the dimensionless superconducting current j_s, it yields:

$$\mathrm{div}\mathbf{j_s} = \nabla^2\Phi. \tag{B.8}$$

We write the finite difference formula of order 2:

$$\frac{d^2\Phi_p}{dx^2} = \frac{\Phi_{p+1} - 2\Phi_p + \Phi_{p-1}}{h^2}. \tag{B.9}$$

As before, we pass to Fourier transform.

$$\left(\frac{d^2\hat{\Phi}}{dx^2}\right)_k = \frac{1}{h^2\sqrt{n}}\sum_{j=0}^{n-1}(\Phi_{j+1} - 2\Phi_j + \Phi_{j-1})e^{-i\frac{2\pi jk}{n}}. \tag{B.10}$$

We make a variable change on both sides to have:

$$\left(\frac{d^2\hat{\Phi}}{dx^2}\right)_k = \frac{1}{h^2}\hat{\psi}\left(e^{i\frac{2k\pi}{n}} + e^{-i\frac{2k\pi}{n}} - 2\right) = \frac{2\hat{\psi}}{h^2}\left(\cos\left(\frac{2k\pi}{n}\right) - 1\right). \tag{B.11}$$

Last, we have:

$$\hat{\Phi} = \hat{j_s}\frac{ih\sin\left(\frac{2k\pi}{n}\right)}{2\left(\cos\left(\frac{2k\pi}{n}\right) - 1\right)}, \tag{B.12}$$

which we use along with the Fourier transform package from NAG to solve the Poisson equation at each time step.

Appendix C

Derivation with inhomogeneous coefficients

In this appendix, we extend the derivations made in chapter 3 by using the inhomogeneous coefficients in the stationary solution as well as in the linearized equations. These derivations are only valid for a limited range of situations (for example when a slow temperature-dependence is introduced or when we solve the equations in different materials) and are placed in this appendix informatively.

C.1 Inhomogeneous coefficients in the Ginzburg-Landau equations

Let us remind the TDGL equations as derived in chapter 3. We recall the dimensionless variables: $\psi = \rho(\mathbf{s},t)e^{i\theta(\mathbf{s},t)}$ is the dimensionless order parameter depending on the spatial coordinate $\mathbf{s}$ and the time t; $\mathbf{a}$ is the magnetic vector potential and Φ is the electrostatic potential. The coefficient $\alpha_r(\mathbf{s},t)$, $\beta_r(\mathbf{s},t)$, $\gamma_r(\mathbf{s},t)$, $\sigma_r(\mathbf{s},t)$ and $\xi_r(\mathbf{s},t)$ are normalized according to Eq. (3.1). The dimensionless parameter u is a real positive constant. The first equation in dimensionless units reads:

$$\gamma_r u\left(\frac{\partial\psi}{\partial t}+i\Phi\psi\right) = -\alpha_r\psi-\beta_r\psi|\psi|^2-(i\nabla+\mathbf{a})^2\psi,$$

or, using ξ_r:

$$u\left(\frac{\partial\psi}{\partial t}+i\Phi\psi\right) = \psi-\psi|\psi|^2-\xi_r^2(i\nabla+\mathbf{a})^2\psi.$$

The second equation is the decomposition of the total current into the superconducting and the normal current:

$$\nabla \times (\nabla \times \mathbf{a}) = \frac{1}{\kappa_0^2}\left[-\frac{i}{2}(\psi^*\nabla\psi - \psi\nabla\psi^*) - \mathbf{a}|\psi|^2 - \sigma_r\left(\frac{\partial \mathbf{a}}{\partial t} + \nabla\Phi\right)\right].$$

The total current $\mathbf{j} = \nabla \times (\nabla \times \mathbf{a})$ is the sum of the superconducting current $\mathbf{j_s} = -\frac{i}{2}(\psi^*\nabla\psi - \psi\nabla\psi^*) - \mathbf{a}|\psi|^2$ and the normal current $\mathbf{j_n} = -\sigma_r\left(\frac{\partial \mathbf{a}}{\partial t} + \nabla\Phi\right)$ in dimensionless units.

The dimensionless total current also obeys the electroneutrality equation (2.55):

$$\mathrm{div}\mathbf{j} = 0.$$

C.2 Stationary solutions

Here we derive the stationary solutions using the coefficients of the inhomogeneity and assume $\alpha_r \leq 0$ i.e. the material is in the superconducting state.

C.2.1 The 1D case

The stationary solutions of the CGL equation have been studied in details [38, 39] and in 1D, one can derive the conditions of the Eckhaus type instability. Here, we derive the stationary solutions for our equations which include magnetic field, electrostatic potential and the possibility of inhomogeneities. We used a similar method as what is used for the CGL equation with real coefficients.

Indeed, we can rewrite equation (3.3) in the same way as in [39] by separating real and imaginary parts:

$$u\gamma_r\frac{\partial \rho}{\partial t} = \frac{\partial^2 \rho}{\partial x^2} + \rho\left[-\alpha_r - \beta_r\rho^2 - \left(a - \frac{\partial \theta}{\partial x}\right)^2\right] \tag{C.1}$$

and

$$u\gamma_r\rho\left(\frac{\partial \theta}{\partial t} + \Phi\right) = \frac{1}{\rho}\frac{\partial}{\partial x}\left[\rho^2\left(\frac{\partial \theta}{\partial x} - a\right)\right], \tag{C.2}$$

where ρ is the amplitude, θ the phase of the complex order parameter $\psi = \rho e^{i\theta}$ and x is the longitudinal dimensionless spatial coordinate.

We recognize in Eq. (C.2) the superconducting current

$$|\mathbf{j_s}| = j_s = -\frac{i}{2}\left(\psi^*\frac{\partial \psi}{\partial x} - \psi\frac{\partial \psi^*}{\partial x}\right) - a|\psi|^2 = \rho^2\left(\frac{\partial \theta}{\partial x} - a\right), \tag{C.3}$$

and we will therefore be able to use the electroneutrality condition (3.5).

We can use the common mechanical analogy to describe the stationary solutions of equations (C.1) and (C.2) by rewriting them in the form:

$$\frac{\partial^2 \rho}{\partial x^2} = -\frac{\partial U(\rho)}{\partial \rho} \tag{C.4}$$

with

$$U = \frac{1}{2}\left(\frac{j_s^2}{\rho^2} - \alpha_r \rho^2 - \beta_r \frac{1}{2}\rho^4\right). \tag{C.5}$$

These equations describe the motion of a particle with spatial coordinate ρ in the field U. In this analogy, the time is represented by x.

C.2.1.1 Case $j_s \neq 0$

We see that $\lim_{\rho^2 \to \infty} U = -\infty$ and $\lim_{\rho^2 \to 0} U = \infty$. Bounded solutions of Eq. (C.4) exist if and only if U has local extrema and has the shape sketched in Fig. C.1. The condition for U to have local

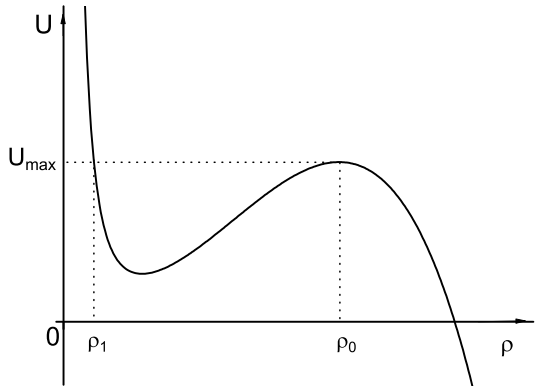

FIGURE C.1: The potential $U = \frac{1}{2}\left(\frac{j_s^2}{\rho^2} - \alpha_r \rho^2 - \beta_r \frac{1}{2}\rho^4\right)$. For $j_s < j_c$, there is a local maximum and minimum and stationary solutions can be seen as either stable states or oscillating states in the potential well.

extrema is

$$\frac{\partial U}{\partial \rho} = \frac{1}{\rho^3}\left(-j_s^2 - \alpha_r \rho^4 - \beta_r \rho^6\right) = 0.$$

Therefore ρ must satisfy:

$$-\rho^4(\alpha_r + \beta_r \rho^2) = j_s^2. \tag{C.6}$$

By studying the shape of $-\rho^4(\alpha_r + \beta_r \rho^2)$, which is positive on $[0, -\frac{\alpha_r}{\beta_r}]$ and has a local maximum for $\rho^2 = -\frac{2\alpha_r}{3\beta_r}$ (see Fig. C.2), we find that the condition (C.6) is only achievable if:

$$j_s^2 < j_c^2, \tag{C.7}$$

with

$$j_c = -\frac{2\alpha_r^{3/2}}{\sqrt{27}\beta_r} \tag{C.8}$$

which is the definition of the Ginzburg-Landau critical (depairing) current. Indeed, the critical current is calculated from the uniform stationary state of the GL equations for which the superconducting current is $j_s = \rho^2\sqrt{-\alpha_r - \beta_r\rho^2}$. For $j_s > j_c$, the only uniform stationary solution is $\rho = 0$: the superconductivity is destroyed. For $j_s < j_c$, there are two different solutions possible which define the two branches seen in Fig. C.2. They correspond to

$$\rho > \sqrt{\frac{-2\alpha_r}{3\beta_r}} \tag{C.9}$$

and

$$\rho < \sqrt{\frac{-2\alpha_r}{3\beta_r}}. \tag{C.10}$$

The stability of each branch can be deduced from thermodynamical arguments (see [1] for example) or by further stability analysis as we see in section 3.3.2.2. Surprisingly, the stable solution is the one satisfying Eq. (C.9) which corresponds to the local maximum of U.

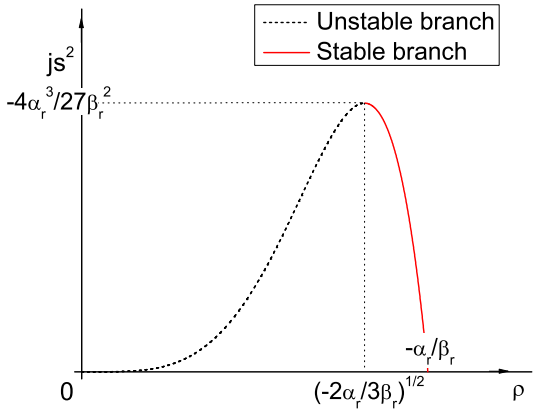

FIGURE C.2: The superconducting current $|\mathbf{j_s}|^2 = -\rho^4(\alpha_r + \beta_r\rho^2)$. It defines as well the Ginzburg-Landau critical (depairing) current $j_c = -\frac{2\alpha_r^{3/2}}{\sqrt{27}\beta_r}$. A further analysis also determines which part of the curve corresponds to the stable branch.

The local extrema of U correspond to solutions which satisfy $\frac{\partial^2\rho}{\partial x^2} = 0$ and in particular, solutions of uniform amplitude. They are described by:

$$\rho = \sqrt{-\frac{1}{\beta_r}(\alpha_r + Q^2)}\ , \text{ with } Q = \frac{j_s}{\rho^2} = \frac{\partial\theta}{\partial x} - a. \tag{C.11}$$

Under the condition that

$$(\alpha_r + Q^2) = \alpha_r + \left(\frac{\partial\theta}{\partial x} - a\right)^2 \leq 0. \tag{C.12}$$

This condition restricts the intensity of the magnetic field and even more accurately the gauge invariant vector potential $a - \frac{\partial\theta}{\partial x}$. Moreover, when a is uniform and in a region where α_r and β_r

are constant, Eq. (3.5), $\frac{\partial}{\partial x}\left[\rho^2\left(\frac{\partial\theta}{\partial x}-a\right)\right]=0$ leads to

$$\begin{cases} \frac{\partial^2\theta}{\partial x^2} & = & 0 \\ \text{or} & & \\ \frac{\partial\theta}{\partial x} & = & \pm\sqrt{\frac{-\alpha_r}{3}}-a. \end{cases} \tag{C.13}$$

Therefore, we write $\frac{\partial\theta}{\partial x}=k_r$, and

$$j_s=-\frac{1}{\beta_r}\left(\frac{\partial\theta}{\partial x}-a\right)\left[\alpha_r+\left(\frac{\partial\theta}{\partial x}-a\right)^2\right]. \tag{C.14}$$

Last, we obtain a family of solutions in the well known twisted plane wave form:

$$\psi_{k_r}=\sqrt{-\frac{1}{\beta_r}\left[\alpha_r+(a-k_r)^2\right]}e^{ik_rx+\theta_0} \tag{C.15}$$

where k_r can depend on α_r and θ_0 is a real number. When k_r is constant, we will simply write $k_r=k$. When the inhomogeneity is written with ξ_r like in equation (3.6) we have:

$$\psi_{k_r}=\sqrt{(1-\xi_r^2(a-k_r)^2)}e^{ik_rx+\theta_0}. \tag{C.16}$$

C.2.1.2 Case $j_s=0$

In this case, the potential becomes $U_0=\frac{1}{2}(-\alpha_r\rho^2-\frac{1}{2}\beta_r)$ with $\lim\limits_{\rho^2\to\infty}U_0=-\infty$ and $\lim\limits_{\rho^2\to0}U_0=0$. The shape of U_0 is plotted in Fig. C.3. Solutions satisfying $\frac{\partial U}{\partial\rho}=0$ have the form:

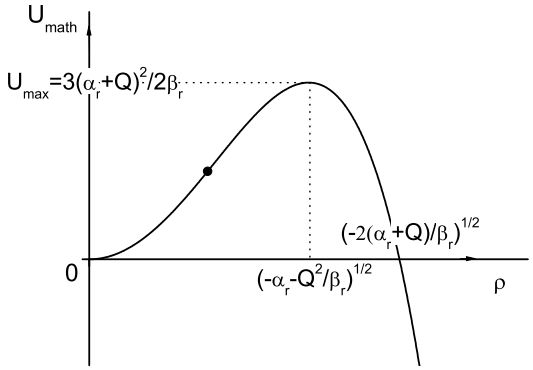

FIGURE C.3: The potential U_{math} as a function of the amplitude ρ. The shape and values correspond as well to the case $j_s=0$ by applying $Q=0$.

$$\rho_0=\sqrt{-\frac{\alpha_r}{\beta r}} \tag{C.17}$$

and when a is uniform, $j_s = 0$ requires the stationary solution to be in the form

$$\psi_0 = \sqrt{-\frac{\alpha_r}{\beta r}} e^{iax+\theta_0}, \tag{C.18}$$

which is in agreement with Eq. (C.15).

C.2.1.3 Comments on this analysis

The choice to write the potential $U = \frac{1}{2}\left(\frac{j_s^2}{\rho^2} - \alpha_r\rho^2 - \beta_r\frac{1}{2}\rho^4\right)$ brings a very beautiful way to describe many particular solutions of the CGL and TDGL equations as we discuss in section 4.1.2. Indeed, common "interesting" solutions will be seen as reflecting the periodic or oscillating movement of the particle in the potential well. However, this choice can be misleading, because of the "diverging limiting case" and because j_s does depend on ρ. Moreover if its expression is substituted, a sign problem emerges. A more purely mathematical way of treating the problem would be to write the potential $U_{\text{math}} = \frac{1}{2}\left[-\rho^2\left(\left[\frac{\partial\theta}{\partial x} - a\right]^2 + \alpha_r\right) - \frac{1}{2}\beta_r\rho^4\right]$. The shape of the potential, plotted in Fig. C.3 does this time converge with the shape of U_0. Solutions corresponding to $\frac{\partial U_{\text{math}}}{\partial\rho} = 0$ are consistent with the ones found before, but in this case, the requirement to have $j_s < j_c$ does not emerge, although it can be brought up artificially.

C.2.2 The 2D case

The 2D case is treated similarly, bringing only minor modifications to the derivation. It could easily be extended to the third dimension as well. The separation of real and imaginary part of (3.3) gives

$$u\gamma_r\frac{\partial\rho}{\partial t} = \frac{\partial^2\rho}{\partial x^2} + \frac{\partial^2\rho}{\partial y^2} + \rho\left[-\alpha_r - \beta_r\rho^2 - \left(\frac{\partial\theta}{\partial x} - a_x\right)^2 + \left(\frac{\partial\theta}{\partial y} - a_y\right)^2\right] \tag{C.19}$$

and

$$u\gamma_r\rho\left(\frac{\partial\theta}{\partial t} + \Phi\right) = \frac{1}{\rho}\frac{\partial}{\partial x}\left[\rho^2\left(\frac{\partial\theta}{\partial x} - a_x\right)\right] + \frac{1}{\rho}\frac{\partial}{\partial y}\left[\rho^2\left(\frac{\partial\theta}{\partial y} - a_y\right)\right], \tag{C.20}$$

where ρ is the amplitude, θ the phase of the complex order parameter ψ, x and y are the longitudinal dimensionless spatial coordinates, a_x and a_y are the components of the magnetic vector potential.

The mechanical analogy can still be used by writing the stationary solutions as:

$$\nabla^2\rho = -\frac{\partial U(\rho)}{\partial\rho} \tag{C.21}$$

with

$$U = \frac{1}{2}\left(\frac{j_s^2}{\rho^2} - \alpha_r\rho^2 - \beta_r\frac{1}{2}\rho^4\right), \tag{C.22}$$

and

$$\mathbf{j_s} = \rho^2(\nabla\theta - \mathbf{a}). \tag{C.23}$$

The continuity equation yields $\nabla \cdot \mathbf{j_s} = 0$.

The value of the critical current is the same as before and solutions such as $\frac{\partial U}{\partial \rho} = 0$ which includes all stationary solutions are described by

$$\rho = \sqrt{-\frac{1}{\beta_r}(\alpha_r + \mathbf{Q}^2)}\ \text{, with } \mathbf{Q} = \frac{\mathbf{h}}{\rho^2} = \nabla\theta - \mathbf{a}, \tag{C.24}$$

under the condition that

$$\alpha_r + (\nabla\theta - \mathbf{a})^2 \leq 0 \tag{C.25}$$

For uniform solutions in ρ, the electroneutrality condition (3.5) gives here $\nabla^2\mathbf{j_s} = 0$. With the added hypothesis $\frac{\partial^2\theta}{\partial x^2} = \frac{\partial^2\theta}{\partial y^2} = 0$, we can write the uniform stationary solutions for the 2D case:

$$\psi_{k,p} = \sqrt{\frac{-\alpha_r - (k\mathbf{e_x} + p\mathbf{e_y} - \mathbf{a})^2}{\beta_r}}e^{i(kx+py+\theta_0)}, \tag{C.26}$$

where $(\mathbf{e_x}\ \mathbf{e_y})$ is the standard unitary basis of the 2D space and (k, p) are real constants.

C.3 Stability of the stationary solutions

We study the stability of the stationary solutions. We start the analysis by writing the equations for all stationary solutions but restrict our focus to the particular solutions of uniform amplitude found previously.

C.3.1 Linearizing the equations

The first step to study the stability of a particular solution $\psi_{k,p}$ is to linearize the time-dependent equations regarding small fluctuations of the order parameter.

$$\delta\psi(\mathbf{s}, t) = f(\mathbf{s}, t) = \psi(\mathbf{s}, t) - \psi_{k,p}. \tag{C.27}$$

The electrostatic potential Φ is of the order of $\delta\psi$, as seen for example from Eq. (C.20): close to the equilibrium, the potential appears with the variation of the density of electrons. Neglecting

terms of order 2 and higher in $\delta\psi$, we have:

$$\psi|\psi|^2 = 2|\psi_{k,p}|^2 f + \psi_{k,p}^2 f^* + |\psi_{k,p}|^2 \psi_{k,p}.$$

The first TDGL equation (3.3) becomes:

$$\begin{aligned} u\gamma_r(\dot{f} + i\Phi\psi_{k,p}) = f(-\alpha_r - 2\beta_r|\psi_{k,p}|^2) - \beta_r f^* \psi_{k,p}^2 - \alpha_r \psi_{k,p} - \beta_r \psi_{k,p}|\psi_{k,p}|^2 \\ +\nabla^2 f + \nabla^2 \psi_{k,p} - 2i\mathbf{a}\cdot\nabla f - 2i\mathbf{a}\cdot\nabla\psi_{k,p} - a^2 f - a^2\psi_{k,p} \end{aligned}$$

Knowing that $\psi_{k,p}$ is a solution of the stationary equations, it simplifies into

$$u\gamma_r(\dot{f} + i\Phi\psi_{k,p}) = f(-\alpha_r - 2\beta_r|\psi_{k,p}|^2) - \beta_r f^* \psi_{k,p}^2 + \nabla^2 f - 2i\mathbf{a}\cdot\nabla.f - a^2 f. \tag{C.28}$$

Using the stationary solution found for 2D (C.26), we have:

$$u\gamma_r(\dot{f}+i\Phi\psi_{k,p}) = f[\alpha_r+2(k\mathbf{e_x}+p\mathbf{e_y}-\mathbf{a})^2-a^2]+f^*[\alpha_r+(k\mathbf{e_x}+p\mathbf{e_y}-\mathbf{a})^2]e^{2i(kx+py+\theta_0)}+\nabla^2 f-2i\mathbf{a}\cdot\nabla f$$

We use the substitution

$$f = \tilde{f}e^{i(kx+py+\theta_0)} \tag{C.29}$$

and obtain

$$\begin{aligned} u\gamma_r(\dot{\tilde{f}} + i\Phi|\psi_{k,p}|) = \tilde{f}[\alpha_r + 2(k\mathbf{e_x} + p\mathbf{e_y} - \mathbf{a})^2 - a^2] + \tilde{f}^*[\alpha_r + (k\mathbf{e_x} + p\mathbf{e_y} - \mathbf{a})^2] \\ +\nabla^2\tilde{f} - (k^2+p^2)\tilde{f} + 2ik\frac{d\tilde{f}}{dx} + 2ip\frac{d\tilde{f}}{dy} + 2a_x k\tilde{f} + 2a_y p\tilde{f} - 2i\mathbf{a}\cdot\nabla\tilde{f}, \end{aligned}$$

which simplifies into

$$\begin{aligned} u\gamma_r(\dot{\tilde{f}} + i\Phi|\psi_{k,p}|) = \tilde{f}[\alpha_r + (k\mathbf{e_x} + p\mathbf{e_y} - \mathbf{a})^2] + \tilde{f}^*[\alpha_r + (k\mathbf{e_x} + p\mathbf{e_y} - \mathbf{a})^2] \\ +\nabla^2\tilde{f} + 2i(k\mathbf{e_x} + p\mathbf{e_y} - \mathbf{a})\cdot\nabla\tilde{f}. \end{aligned}$$

Last, we write the first linearized equation:

$$u\gamma_r(\dot{\tilde{f}} + i\Phi|\psi_{k,p}|) = 2\Re(\tilde{f})[\alpha_r + (k\mathbf{e_x} + p\mathbf{e_y} - \mathbf{a})^2] + \nabla^2\tilde{f} + 2i(k\mathbf{e_x} + p\mathbf{e_y} - \mathbf{a})\cdot\nabla\tilde{f}, \tag{C.30}$$

with $\Re(z)$ and $\Im(z)$ denoting the real and imaginary part of a complex number z. After neglecting the terms of order higher than two in f, the second TDGL equation (3.4) reads

$$\kappa(\mathbf{j} - \mathbf{j}_{k,p}) = \frac{i}{2}(\psi_{k,p}^*\nabla f + f^*\nabla\psi_{k,p} - \psi_{k,p}\nabla f^* - f\nabla\psi_{k,p}^*) - \mathbf{a}(\psi_{k,p}^* f + \psi_{k,p} f^*) - \sigma_r(\dot{\mathbf{a}} - \nabla\Phi),$$

knowing that the stationary supercurrent is

$$\mathbf{j}_{k,p} = -\frac{i}{2}(\psi^*_{k,p}\nabla\psi_{k,p} - \psi_{k,p}\nabla\psi^*_{k,p}) - \mathbf{a}|\psi_{k,p}|^2. \tag{C.31}$$

We use the substitution described in Eq. (C.29)

$$\kappa(\mathbf{j} - \mathbf{j}_{k,p}) = 2\Re(\tilde{f})|\psi_{k,p}|(k\mathbf{e_x} + p\mathbf{e_y} - \mathbf{a}) + \Im(\nabla\tilde{f})|\psi_{k,p}| - \sigma_r(\dot{\mathbf{a}} - \nabla\Phi) \tag{C.32}$$

and obtain the linearized TDGL equations for the 2D case when $|\psi_{k,p}| = \sqrt{\frac{-\alpha_r-(k\mathbf{e_x}+p\mathbf{e_y}-\mathbf{a})^2}{\beta_r}}$:

$$u\gamma_r(\dot{\tilde{f}} + i\Phi|\psi_{k,p}|) = 2\Re(\tilde{f})[\alpha_r + (k\mathbf{e_x} + p\mathbf{e_y} - \mathbf{a})^2] + \nabla^2\tilde{f} + 2i(k\mathbf{e_x} + p\mathbf{e_y} - \mathbf{a})\cdot\nabla\tilde{f} \tag{C.33}$$

$$\kappa(\mathbf{j} - \mathbf{j}_{k,p}) = 2\Re(\tilde{f})|\psi_{k,p}|(k\mathbf{e_x} + p\mathbf{e_y} - \mathbf{a}) + \Im(\nabla\tilde{f})|\psi_{k,p} - \sigma_r(\dot{\mathbf{a}} - \nabla\Phi)|. \tag{C.34}$$

For the more general solution

$$\psi_{\nabla\theta} = \sqrt{\frac{-\alpha_r - (\nabla\theta - \mathbf{a})^2}{\beta_r}}e^{i\theta},$$

we have:

$$u\gamma_r(\dot{\tilde{f}} + i\Phi|\psi_{\nabla\theta}|) = 2\Re(\tilde{f})[\alpha_r + (\nabla\theta - \mathbf{a})^2] + \nabla^2\tilde{f} + 2i(\nabla\theta - \mathbf{a})\cdot\nabla\tilde{f} \tag{C.35}$$

$$\kappa(\mathbf{j} - \mathbf{j}_{\nabla\theta}) = 2\Re(\tilde{f})|\psi_{\nabla\theta}|(\nabla\theta - \mathbf{a}) + \Im(\nabla\tilde{f})|\psi_{\nabla\theta} - \sigma_r(\dot{\mathbf{a}} - \nabla\Phi)|. \tag{C.36}$$

C.4 Result of the stability analysis

The stability analysis done in sections 3.3.2.1 and 3.3.2.2 can be extended by using the coefficient α_r (in this case considered constant) in the equations and in the stationary solution $|\psi_{k,p}|^2 = \frac{-\alpha_r-(k\mathbf{e_x}+p\mathbf{e_y}-\mathbf{a})^2}{\beta_r}$. The stability condition in 2D for the stationary solutions for $a_y = 0$ yields

$$\begin{cases} 3(a_x - k)^2 + p^2 & < & -\alpha_r \\ \quad \text{or} & & \\ \quad |q| & > & \sqrt{2}\sqrt{3(a_x - k)^2 + p^2 + \alpha_r}, \end{cases} \tag{C.37}$$

with q being the wavenumber of the perturbation. This stability condition can easily be transferred to the 1D case.

Bibliography

[1] V. V. Schimdt, *The physics of Superconductors*, vol. 121 (Springer, 1997), ISBN 978-3-642-08251-1.

[2] P. G. Gennes, *Superconductivity of metals and alloys* (Addison-Wesley, Redwood City, 1989), ISBN 978-0738201016.

[3] M. Tinkham, *Introduction to Superconductivity* (McGraw-Hill, New York, 1996), ISBN 978-0070648784.

[4] L. D. Landau and E. M. Lifshitz, *Statistical Physics Part 2, Vol. 5*, Landau and Lifshitz Course of Theoretical Physics (Butterworth-Heinemann, 1980), ISBN 978-0-750-63372-7.

[5] E. M. Lifshitz and L. P. Pitaevskii, *Statistical Physics Part 2, Vol. 9*, Landau and Lifshitz Course of Theoretical Physics (Butterworth-Heinemann, 1980), ISBN 978-0-750-62636-1.

[6] L. D. Landau and E. M. Lifshitz, *Fluid Mechanics, Vol. 6 (2nd ed.)*, Landau and Lifshitz Course of Theoretical Physics (Butterworth-Heinemann, 1987), ISBN 978-0-080-33933-7.

[7] A. B. Pippard, Proceedings of the Royal Society of London. Series A. Mathematical and Physical Sciences **216**, 547 (1953).

[8] L. N. Cooper, Phys. Rev. **104**, 1189 (1956).

[9] J. Bardeen, L. N. Cooper, and J. R. Schrieffer, Phys. Rev. **106**, 162 (1957).

[10] J. Bardeen, L. N. Cooper, and J. R. Schrieffer, Phys. Rev. **108**, 1175 (1957).

[11] V. L. Ginzburg and L. D. Landau, Zh. Eksp. Teor. Fiz. **20**, 1064 (1950).

[12] L. P. Gor'kov, Zh. Eksp. Teor. Fiz. **36**, 1918 (1959).

[13] L. P. Gor'kov, Sov. Phys. JETP **9**, 1364 (1959).

[14] A. A. Abrikosov, Doklady Akademii Nauk SSSR **86**, 489 (1952).

[15] A. A. Abrikosov, Zh. Eksp. Teor. Fiz. **32**, 1442 (1957).

[16] A. A. Abrikosov, Sov. Phys. JETP **5**, 1174 (1957).

[17] L. V. Shubnikov, V. Khotkevich, Y. Shepelev, and Y. Ryabinin, Zh. Eksp. Teor. Fiz. **7**, 221 (1937).

[18] J. Pearl, Applied Physics Letters **5**, 65 (1964).

[19] U. Essmann and H. Träuble, Physics Letters A **24**, 526 (1967).

[20] H. F. Hess, R. B. Robinson, R. C. Dynes, J. M. Valles, and J. V. Waszczak, Phys. Rev. Lett. **62**, 214 (1989).

[21] J. Bardeen and M. J. Stephen, Phys. Rev. **140**, A1197 (1965).

[22] L. P. Gor'kov and N. B. Kopnin, Soviet Physics Uspekhi **18**, 496 (1975).

[23] N. B. Kopnin, Reports on Progress in Physics **65**, 1633 (2002).

[24] B. D. Josephson, Physics Letters **1**, 251 (1962).

[25] K. K. Likharev, Rev. Mod. Phys. **51**, 101 (1979).

[26] L. G. Aslamazov and A. I. Larkin, Pis'ma Zh. Eksp. Teor. Fiz. **9**, 150 (1968).

[27] L. G. Aslamazov and A. I. Larkin, JETP letters **9**, 87 (1969).

[28] R. Tidecks, *Current-Induced Nonequilibrium Phenomena in Quasi-One-Dimensional Superconductors*, vol. 121 of *Springer Tracts in Modern Physics* (Springer Berlin / Heidelberg, 1990).

[29] A. Schmid, Zeitschrift für Physik B Condensed Matter (Phys. Kondens. Mater.) **5**, 302 (1966).

[30] E. Abrahams and T. Tsuneto, Phys. Rev. **152**, 416 (1966).

[31] B. I. Ivlev and N. B. Kopnin, Usp. Fiz. Nauk **142**, 435 (1984).

[32] B. I. Ivlev and N. B. Kopnin, Soviet Physics Uspekhi **27**, 206 (1984).

[33] B. I. Ivlev and N. B. Kopnin, Advances in Physics **33**, 47 (1984).

[34] N. B. Kopnin, Journal of Low Temperature Physics **129**, 219 (2002).

[35] L. P. Gor'kov and G. M. Eliashberg, Zh. Eksp. Teor. Fiz. **54**, 612 (1968).

[36] L. P. Gor'kov and G. M. Eliashberg, Sov. Phys. JETP **27**, 328 (1968).

[37] L. Kramer and R. J. Watts-Tobin, Phys. Rev. Lett. **40**, 1041 (1978).

[38] I. S. Aranson and L. Kramer, Rev. Mod. Phys. **74**, 99 (2002).

[39] L. Kramer and W. Zimmermann, Physica D: Nonlinear Phenomena **16**, 221 (1985).

[40] M. Lu-Dac and V. V. Kabanov, Journal of Physics: Conference Series **129**, 012050 (2008).

[41] M. Lu-Dac and V. V. Kabanov, Phys. Rev. B **79**, 184521 (2009).

[42] W. A. Little, Phys. Rev. **156**, 396 (1967).

[43] R. A. Ferrell, Phys. Rev. Lett. **13**, 330 (1964).

[44] T. M. Rice, Phys. Rev. **140**, A1889 (1965).

[45] J. S. Langer and V. Ambegaokar, Phys. Rev. **164**, 498 (1967).

[46] R. D. Parks and R. P. Groff, Phys. Rev. Lett. **18**, 342 (1967).

[47] T. K. Hunt and J. E. Mercereau, Phys. Rev. Lett. **18**, 551 (1967).

[48] D. E. McCumber and B. I. Halperin, Phys. Rev. B **1**, 1054 (1970).

[49] W. W. Webb and R. J. Warburton, Phys. Rev. Lett. **20**, 461 (1968).

[50] T. J. Rieger, D. J. Scalapino, and J. E. Mercereau, Phys. Rev. B **6**, 1734 (1972).

[51] W. J. Skocpol, M. R. Beasley, and M. Tinkham, Journal of Low Temperature Physics **16**, 145 (1974).

[52] I. M. Dmitrenko, Low Temperature Physics (Fiz. Nizk. Temp.) **22**, 648 (1996).

[53] F. von Oppen and E. K. Riedel, Phys. Rev. B **46**, 3203 (1992).

[54] X. Zhang and J. C. Price, Phys. Rev. B **55**, 3128 (1997).

[55] N. C. Koshnick, H. Bluhm, M. E. Huber, and K. A. Moler, Science **318**, 1440 (2007).

[56] N. Giordano, Phys. Rev. Lett. **61**, 2137 (1988).

[57] N. Giordano, Phys. Rev. B **41**, 6350 (1990).

[58] A. D. Zaikin, D. S. Golubev, A. van Otterlo, and G. T. Zimányi, Phys. Rev. Lett. **78**, 1552 (1997).

[59] J. E. Mooij and C. J. P. M. Harmans, New Journal of Physics **7**, 219 (2005).

[60] J. E. Mooij, T. P. Orlando, L. Levitov, L. Tian, C. H. van der Wal, and S. Lloyd, **285**, 1036 (1999).

[61] J. E. Mooij and Y. V. Nazarov, Nature Physics **2**, 169 (2006).

[62] K. Arutyunov, D. Golubev, and A. Zaikin, Physics Reports **464**, 1 (2008).

[63] M. B. Tarlie and K. R. Elder, Phys. Rev. Lett. **81**, 18 (1998).

[64] D. Y. Vodolazov and F. M. Peeters, Phys. Rev. B **66**, 054537 (2002).

[65] D. Y. Vodolazov, F. M. Peeters, S. V. Dubonos, and A. K. Geim, Phys. Rev. B **67**, 054506 (2003).

[66] S. Michotte, S. Mátéfi-Tempfli, L. Piraux, D. Y. Vodolazov, and F. M. Peeters, Phys. Rev. B **69**, 094512 (2004).

[67] L. Kramer and R. Rangel, Journal of Low Temperature Physics **57**, 391 (1984).

[68] M. Lu-Dac and V. V. Kabanov, Physica C: Superconductivity **470**, 942 (2010).

[69] M. Lu-Dac and V. V. Kabanov, Phys. Rev. Lett. **105**, 157005 (2010).

[70] U. Parts, V. M. H. Ruutu, J. H. Koivuniemi, Y. M. Bunkov, V. V. Dmitriev, M. Fogelström, M. Huebner, Y. Kondo, N. B. Kopnin, J. S. Korhonen, et al., EPL (Europhysics Letters) **31**, 449 (1995).

[71] S. V. Iordanskii, Zh. Eksp. Teor. Fiz. **48**, 708 (1965).

[72] S. V. Iordanskii, Sov. Phys. JETP **21**, 467 (1965).

[73] A. Weber and L. Kramer, Journal of Low Temperature Physics **84**, 289 (1991).

[74] G. R. Berdiyorov, M. V. Milošević, and F. M. Peeters, Phys. Rev. B **79**, 184506 (2009).

[75] A. Andronov, I. Gordion, V. Kurin, I. Nefedov, and I. Shereshevsky, Physica C: Superconductivity **213**, 193 (1993).

[76] A. I. Larkin and Y. N. Ovchinnikov, Zh. Eksp. Teor. Fiz. **68**, 1915 (1975).

[77] A. I. Larkin and Y. N. Ovchinnikov, Sov. Phys. JETP **41**, 960 (1976).

[78] W. Klein, R. P. Huebener, S. Gauss, and J. Parisi, Journal of Low Temperature Physics **61**, 413 (1985).

[79] D. Vodolazov, B. J. Baelus, and F. M. Peeters, Physica C: Superconductivity **404**, 400 (2004), proceedings of the Third European Conference on Vortex Matter in Superconductors at Extreme Scales and Conditions.

[80] D. Y. Vodolazov and F. M. Peeters, Phys. Rev. B **76**, 014521 (2007).

[81] A. V. Silhanek, M. V. Milošević, R. B. G. Kramer, G. R. Berdiyorov, J. Van de Vondel, R. F. Luccas, T. Puig, F. M. Peeters, and V. V. Moshchalkov, Phys. Rev. Lett. **104**, 017001 (2010).

[82] E. Goldobin, A. Sterck, T. Gaber, D. Koelle, and R. Kleiner, Phys. Rev. Lett. **92**, 057005 (2004).

[83] E. Goldobin, N. Stefanakis, D. Koelle, and R. Kleiner, Phys. Rev. B **70**, 094520 (2004).

[84] L. Kelvin (Sir W. Thomson), *Mathematical and Physical Papers, Vol. 4: Hydrodynamics and General Dynamics* (Cambridge University Press, 1910), ISBN 9781108029018.

[85] H. L. F. von Helmholtz, *Monatsberichte der königl* (Akademie Wissenschaften, Berlin, 1868).

[86] L. Rayleigh (J. W. Strutt), *Scientific papers, Vol. 1* (Cambridge University Press, 1899).

[87] R. Blaauwgeers, V. B. Eltsov, G. Eska, A. P. Finne, R. P. Haley, M. Krusius, J. J. Ruohio, L. Skrbek, and G. E. Volovik, Phys. Rev. Lett. **89**, 155301 (2002).

[88] G. Volovik, JETP Letters (Pis'ma v ZhETF) **75**, 418 (2002).

[89] S. Korshunov, JETP Letters (Pis'ma v ZhETF) **75**, 423 (2002).

[90] A. P. Finne, V. B. Eltsov, R. Hnninen, N. B. Kopnin, J. Kopu, M. Krusius, M. Tsubota, and G. E. Volovik, Reports on Progress in Physics **69**, 3157 (2006).

[91] T. W. B. Kibble, Journal of Physics A: Mathematical and General **9**, 1387 (1976).

[92] W. H. Zurek, Nature **317**, 505 (1985).

[93] W. H. Zurek, Physics Reports **276**, 177 (1996).

[94] I. Chuang, R. Durrer, N. Turok, and B. Yurke, Science **251**, 1336 (1991).

[95] M. J. Bowick, L. Chandar, E. A. Schiff, and A. M. Srivastava, Science **263**, 943 (1994).

[96] P. C. Hendry, N. S. Lawson, R. A. M. Lee, P. V. E. McClintock, and C. D. H. Williams, Nature **368**, 315 (1994).

[97] V. M. H. Ruutu, V. B. Eltsov, A. J. Gill, T. W. B. Kibble, M. Krusius, Y. G. Makhlin, B. Placais, G. E. Volovik, and W. Xu, Nature **382**, 334 (1996).

[98] V. M. Ruutu, V. B. Eltsov, M. Krusius, Y. G. Makhlin, B. Plaçais, and G. E. Volovik, Phys. Rev. Lett. **80**, 1465 (1998).

[99] V. Eltsov, M. Krusius, and G. Volovik (Elsevier, 2005), vol. 15 of *Progress in Low Temperature Physics*, pp. 1 – 137.

[100] A. Maniv, E. Polturak, and G. Koren, Phys. Rev. Lett. **91**, 197001 (2003).

[101] R. Carmi and E. Polturak, Phys. Rev. B **60**, 7595 (1999).

[102] M. Hindmarsh and A. Rajantie, Phys. Rev. Lett. **85**, 4660 (2000).

[103] J. R. Kirtley, C. C. Tsuei, and F. Tafuri, Phys. Rev. Lett. **90**, 257001 (2003).

[104] A. Maniv, E. Polturak, G. Koren, Y. Bliokh, B. Biehler, B.-U. Runge, P. Leiderer, B. Shapiro, and I. Shapiro, Phys. Rev. Lett. **94**, 247005 (2005).

[105] R. Monaco, J. Mygind, R. J. Rivers, and V. P. Koshelets, Phys. Rev. B **80**, 180501 (2009).

[106] M. Ghinovker, B. Y. Shapiro, and I. Shapiro, EPL (Europhysics Letters) **53**, 240 (2001).

[107] P. Laguna and W. H. Zurek, Phys. Rev. Lett. **78**, 2519 (1997).

[108] P. Laguna and W. H. Zurek, Phys. Rev. D **58**, 085021 (1998).

[109] T. Kibble and G. Volovik, JETP Letters (Pis'ma v ZhETF) **65**, 102 (1997).

[110] N. B. Kopnin and E. V. Thuneberg, Phys. Rev. Lett. **83**, 116 (1999).

[111] I. S. Aranson, N. B. Kopnin, and V. M. Vinokur, Phys. Rev. Lett. **83**, 2600 (1999).

[112] G. E. Volovik, Physica B: Condensed Matter **280**, 122 (2000).

[113] I. Aranson, B. Y. Shapiro, and V. Vinokur, Phys. Rev. Lett. **76**, 142 (1996).

[114] R. Yusupov, T. Mertelj, V. V. Kabanov, S. Brazovskii, P. Kusar, J.-H. Chu, I. R. Fisher, and D. Mihailovic, Nature Physics **(advance online publication)** (2010).

[115] J. Demsar, B. Podobnik, V. V. Kabanov, T. Wolf, and D. Mihailovic, Phys. Rev. Lett. **82**, 4918 (1999).

[116] J. Demsar, R. D. Averitt, A. J. Taylor, V. V. Kabanov, W. N. Kang, H. J. Kim, E. M. Choi, and S. I. Lee, Phys. Rev. Lett. **91**, 267002 (2003).

[117] V. V. Kabanov, J. Demsar, and D. Mihailovic, Phys. Rev. Lett. **95**, 147002 (2005).

[118] P. Kusar, V. V. Kabanov, J. Demsar, T. Mertelj, S. Sugai, and D. Mihailovic, Phys. Rev. Lett. **101**, 227001 (2008).

[119] J. H. Bechtel, Journal of Applied Physics **46**, 1585 (1975).

[120] D. C. Mattis and J. Bardeen, Phys. Rev. **111**, 412 (1958).